Computational Study of Materials Under Pressure

By

Deepa Kasinathan
B.Sc. (Mumbai University, India) 1999
M.Sc. (IIT Mumbai, India) 2001

DISSERTATION

Submitted in partial satisfaction of the requirements for the degree of

Doctor of Philosophy

in

Physics

in the

OFFICE OF GRADUATE STUDIES

of the

UNIVERSITY OF CALIFORNIA
DAVIS

Approved:

_____

_____

_____

Committee in Charge

2006

Acknowledgements

Contents

List of Tables

List of Figures

Chapter 1

Introduction

Pressure possesses perhaps the greatest range of all the physical variables. The physical properties of materials depend strongly on structure and interatomic distances. Since pressure can vary these distances considerably more than, say, temperature, it provides an extremely powerful means of examining the relationship between structure and properties - both towards a better fundamental understanding of the underlying phenomena and also for the improved design of applied materials. Additionally, pressure is a 'clean' variable in that it can bring about large changes in structure and properties without altering the chemical composition or thermal energy of a system. This makes high-pressure systems particularly amenable to computational study.

The studies of the pressure behavior of the physical properties of materials may provide additional valuable information about these properties. Applying pressure changes the lattice parameters and hence produces shifts of the electronic states in the crystal. Therefore, pressure provides a convenient technique for shifting the relative positions of some energy levels by a controlled amount. It is also evident that by applying pressure one can change the band extrema from one point of the Brillouin zone to another, thereby altering the underlying property of the system as a functional of pressure.

First principles electronic structure calculations have contributed significantly to high pressure studies, especially of solids. Main merit of these first principles calculations is their predictive power, as they demand little *a priori* experimental data. A few well established achievements of their independent predictive power are: (1) prediction of phase transition, even under physical conditions, which are not yet easily attainable in the laboratories; (2) interpretation of mechanism of physical processes, especially in the case of observed anomalies by providing finer details of the calculations; (3) resolving the controversies, often with hints about the associated reasoning for the inappropriate interpretation.

For example, though superconductivity in MgB_2 itself was not predicted *a priori*, the *ab initio* calculations have shown [1] as to why its T_c falls as a function of pressure. It is concluded that the increasing phonon frequency and decreasing electronic density of states at the Fermi level leads to the observed decrease in the critical temperature under pressure.

In the following chapters, I will present the results of first principles analysis under pressure for CoN, MnO and Li.

CoN, a paramagnet at ambient pressure, undergoes a change in structure coupled with a ferromagnetic transition with increasing pressure.

MnO, a classic prototype for a Mott insulator exibits rich physics as a function of pressure, including phase transition, volume collapse, insulator - metal transition, etc. This system has been a long standing challenge to density functional methods.

Li, the simplest metal becomes a superconductor under pressure, with the highest T_c observed in any elemental metal. Increasingly strong electron-phonon coupling concentrated along intersections of Kohn anomaly surfaces with the evolving Fermi surface, drives this simple metal to become a superconductor under pressure.

Chapter 2

Density Functional Theory and Techniques

2.1 Outline of the problem

We wish to address the question, what are the energies and the wave functions of electrons in a solid under the influnce of the nuclei as well as other electrons. The fundamental problem in this regard is the solution of Schrödingers equation for many electron systems with interaction among the electrons and the nuclei. One of the approaches to the solution of this problem, which is the basis of the modern quantitative theory for electronic structure calculations is to rigourously map the problem of many electrons onto the problem of an independent electron moving in the mean field of the other electrons and ions.

2.2 Origin of the solution

The solution to the above problem started off with the ***Born-Oppenheimer*** approximation. This approximation amounts to saying that we can seperate the electronic and nuclear degrees of freedom. Because the electronic mass is so much smaller than that of the nuclei the electrons respond almost instantaneously to the changes in the positions of the nuclei. It is a good approximation to say that the electrons are always in their ground state as the atoms of the solid vibrate thermally. This means that the positions of the nuclei are parameters that appear in the potential of the schrödinger equation defining the wave functions of the electrons.

2.3 Density Functional Theory

The next advent for the independent electron approximation came with the development of *density functional theory* (DFT) by Hohenberg-Kohn-Sham[2, 3]. The basic idea of DFT originated from the query 'can we arrive at a potential V(r) uniquely, given the charge density ρ(r) of the system?'. The density functional theory yields two results, one important conceptually and the other a framework for practical calculations:

- The solution of the many-body ground state problem is reduced exactly to the solution for the ground-state density distribution $\rho(r)$ given by *one-particle* schrödinger equation. The effective potential in the schrödinger equation includes, in principle all the interaction effects: the Hartree potential (the coulomb potential due to the charge distribution when the electrons are treated as fixed), the exchange potential (due to the interaction described by the Pauli exclusion principle), and the

correlation potential (due to the effect of the given electron on the overall charge distribution).

- An approximation for effective potential is given by regarding a small neighbourhood of the electron system. This result forms the so-called 'local-density-functional' approximation.

Thus the charge density becomes the central quantity that must be found, in the place of many electron wave functions. More formally Hohenberg and Kohn showed that the ground state energy is a *unique functional* of $\rho(r)$. Unfortunately the functional is not known! But whatever the functional is, it acquires a minimum value when the charge density is the correct ground state charge density. Mathematically this means that we have to use a *variational principle* for finding the charge density.

Then, Kohn and Sham derived a system of one-particle equations for the description of the electronic ground state. The interacting N-electron problem was thus mapped exactly onto N single particle equations. This means each electron is moving independently of the other electrons, but it experiences an effective potential which emulates all the interactions with the other electrons. This gives the rigorous justification for the independent electron approximation which we will be using all along. It was also showed that the effective potential is a unique functional of the charge density. The one-particle equations are known as the Kohn-Sham equations.

2.3.1 Hartree Approximation and Self Consistency

First of all we shall discuss the simplest Hartree approximation[46]. This introduces the idea of *self-consistency* between the charge density and the effective potential.

In the Hartree approximation each electron moves independently in the mean electrostatic field of the other electrons and the nuclear electrostatic potentials. The electrostatic potential V_H due to the electronic charge density $\rho(r)$ is given by Poisson's equation,

$$\nabla^2 V_H(r) = -(\frac{\rho(r)}{\varepsilon_0}) \tag{2.1}$$

or

$$V_H(r) = \int \frac{\rho(r')dr'}{4\pi\varepsilon_0|r-r'|} \tag{2.2}$$

where $V_H(r)$ is called the Hartree potential. The effective potential felt by each independent electron is then,

$$V_{eff}(r) = V_H(r) + V_N(r) \tag{2.3}$$

where $V_N(r)$ is the electrostatic potential due to the nuclei

$$V_N(r) = \sum_i \frac{Z_i e}{4\pi\varepsilon_0|r-R_i|} \tag{2.4}$$

and Z_ie is the charge on the i th nucleus and R_i is its position. The Schrödinger equation for the wave function of the j th independent electron is

$$-\frac{\hbar^2}{2m}\nabla^2\Psi_j(r) + V_{eff}(r)\psi_j(r) = \varepsilon_j\Psi_j(r) \tag{2.5}$$

Once this equation is solved the eigen states are populated with electrons. A new charge density is then calculated from the occupied states as follows

$$\rho(r) = \sum_{j occupied} \Psi_j(r)\Psi_j^*(r) \tag{2.6}$$

Now the wave functions $\Psi_j(r)$ are being defined by an effective potential in eqn (2.5) which is a functional of the charge density, through eqn (2.2), which in turn is defined by the wavefunctions in eqn (2.6)! This is called a self-consistent field problem. When it is solved till convergence the output charge density is the same as the input charge density.

The Hartree problem that we just discussed can also be set up starting with the total

energy of the system as a functional of the charge density and then to minimise the energy with respect to the charge density. This is the variational problem. In this way of doing things the ground state total energy is expressed as follows

$$E_G[\rho(r)] = T[\rho(r)] + \int \rho(r)V_N(r)dr + \frac{1}{2}\int \rho(r)V_H(r)dr \tag{2.7}$$

where $T[\rho(r)]$ is the kinetic energy of the electrons. Minimization of this energy, subject to the constraint that the total number of electrons is conserved,

$$\int \rho(r)dr = N, \tag{2.8}$$

is equivalent to solving eqns (2.3), (2.5), (2.6).

2.4 One-particle Kohn-Sham equation

Now let us see how the Kohn-Sham equation is derived: The exact ground state energy functional for a system containing interacting electrons in the presence of nuclei can be written in terms of charge density as

$$E_G[\rho(r), R] = E_{el}[\rho(r), R] + E_{ion}[R, R^{'}] \tag{2.9}$$

$$E_{el}[\rho(r), R] = T_s[\rho] + E_{ES}[\rho] + E_{XC}[\rho, R] \tag{2.10}$$

where,

R, R$^{'}$: denote nuclear coordinates.

T$_s[\rho]$: Kinetic energy of the non-interacting electron gas of the same density as that of the actual interacting system.

E$_{XC}[\rho]$: exchange-correlation energy.

E$_{ES}[\rho]$: total electrostatic energy.

Now,

$$E_{ES}[\rho] = E_H[\rho] + E_{ext}[\rho, R] + E_{mad}(R, R^{'}) \tag{2.11}$$

$$E_{ES}[\rho] = \int\int \frac{\rho(r)\rho(r^{'})}{|r-r^{'}|}drdr^{'} + \int V_{ext}(r)\rho(r)dr + \sum_{R,R^{'}} \frac{Z_R Z_R^{'}}{|R-R^{'}|} \tag{2.12}$$

where,

$\mathrm{E}_H[\rho]$: energy due to Hartree potential.

$\mathrm{E}_{ext}[\rho,\mathrm{R}]$: energy due to external potential.

$\mathrm{E}_{mad}(\mathrm{R},\mathrm{R}^{'})$: energy due to ion-ion madelung potential.

Therefore,

$$E[\rho(r), R] = T_S[\rho] + E_{XC}[\rho] + E_H[\rho] + E_{ext}[\rho, R] + E_{mad}(R, R^{'}) \tag{2.13}$$

Now, minimising this energy, subject to the constraint of charge conservation,

$$\int \rho(r)dr = N \tag{2.14}$$

leads to the **Kohn − Sham** equation,

$$[-\nabla^2 + V_{eff}]\psi_i(r) = \varepsilon_i^{KS}\psi_i(r) \tag{2.15}$$

where,

$$\begin{aligned} V_{eff} &= effectivepotential. \\ &= V_H(r) + V_N(r) + V_{xc}(r) \\ &= 2\int \frac{dr^{'}\rho(r^{'})}{|r-r^{'}|} + 2\sum \frac{Z_R}{|r-R|} + \frac{\delta E_{xc}[\rho]}{\delta\rho(r)} \end{aligned}$$

Thus solving the Kohn-Sham equation, the new charge density is calculated for the occupied states using eqn (2.6). The only difficulty is that the exchange-correlation energy functional E_{XC} is not known for a spatially varying charge density. To solve this, we apply the *Local Density Approximation* [46]. In this approximation we pick a volume element in the solid and measure the charge density there and find that it is some value, which we call ρ_0. The exchange-correlation energy we assign to this volume element is then approximated as the exchange-correlation energy of a volume element in a uniform electron gas

of the same density as ρ_0. This is an approximation because it ignores the fact that the charge density in the solid is varying from one volume to another.

Also the kinetic energy is expressed as,

$$T_s = -\sum_{i}^{occ} n_i < \psi_i|\nabla^2|\psi_i >= \int^{E_F} \varepsilon N(\varepsilon)d\varepsilon - \int V_{eff}(r)\rho(r)d(r) \tag{2.16}$$

Therefore eqn (2.13) can be recasted as,

$$E^{KS}[\rho] = \int^{E_F} \varepsilon N(\varepsilon)d\varepsilon - \int [\frac{1}{2}\Phi + \mu_{xc}]\rho(r)d(r) + E_{XC}^{LDA} + E_{mad} \tag{2.17}$$

where,

Φ : Hartree potential

μ_{XC} : Exchange-Correlation potential

Now eqns (2.6), (2.15), (2.17) are solved self consistently. Automatically the loop comes to an end when the output charge density is equal to the input charge density.

2.5 Basis Set

The next step in solving the Kohn-Sham equation to obtain the ground state eigenfunctions, involves in a suitable choice of a basis set. Most of the electronic structure calculations presented in my dissertation were performed using a Full-Potential-Local-Orbital (FPLO)[5, 6] scheme. In this section, I will provide a brief overview of this scheme.

2.5.1 Local-Orbital Minimum-Basis Scheme

Let us start from the well known ansatz for the Bloch states $\Psi_{\mathbf{k}n}(\mathbf{r})$,

$$\Psi_{\mathbf{k}n}(\mathbf{r}) = \sum_{\mathbf{R}\mathbf{s}L} \phi_{\mathbf{s}L}(\mathbf{r} - \mathbf{R} - \mathbf{s}) C_{L\mathbf{s},\mathbf{k}n} e^{i\mathbf{k}\cdot(\mathbf{R}+\mathbf{s})}, \tag{2.18}$$

where, the basis states $\phi_{\mathbf{s}L}$ are used to approximate the Kohn-Sham wave function of the crystal and are local orbitals centered at sites $\mathbf{s}$ in the elementary cell defined by the lattice

vector **R**. They are solution of an atom-like Schrödinger equation and are denoted by a complete set of atomic quantum numbers L = {ρ,l,m}.

Due to the choice of nonorthogonal basis sets, one needs to solve the secular equation,

$$HC = SC\varepsilon, \tag{2.19}$$

where the Hamiltonian H and overlap S matrices are defined by

$$H^{LL'}_{\mathbf{ss'}} = \sum_{\mathbf{R}} < \mathbf{O}\mathbf{s}'L'|\widehat{H}|\mathbf{R}\mathbf{s}L > e^{ik\cdot(\mathbf{R}+\mathbf{s}-\mathbf{s}')}, \tag{2.20}$$

$$S^{LL'}_{\mathbf{ss'}} = \sum_{\mathbf{R}} < \mathbf{O}\mathbf{s}'L'|\mathbf{R}\mathbf{s}L > e^{ik\cdot(\mathbf{R}+\mathbf{s}-\mathbf{s}')}. \tag{2.21}$$

In order to avoid unnecessarily large matrix problems, the local basis states are divided into core states $\phi_{\mathbf{s}L_c}$ and valence states $\phi_{\mathbf{s}L_v}$. The core states are then defined by

$$\langle \mathbf{R}'\mathbf{s}'L_c^{'}|\mathbf{R}\mathbf{s}L_c\rangle = \delta_{cc'}\delta_{\mathbf{RR}'}\delta_{\mathbf{ss}'} \tag{2.22}$$

If this condition is fulfilled, the core states can be removed from the basis by an exact transformation. Next, the overlap matrix can be decomposed into,

$$S = \begin{pmatrix} 1 & S_{cv} \\ S_{vc} & S_{vv} \end{pmatrix} = \begin{pmatrix} 1 & 0 \\ S_{vc} & S^L_{vv} \end{pmatrix} \begin{pmatrix} 1 & S_{cv} \\ 0 & S^R_{vv} \end{pmatrix} = S^L S^R \tag{2.23}$$

where the left and right triangular matrices S^L_{vv} and S^R_{vv} obey the relation

$$S^L_{vv} S^R_{vv} = S_{vv} - S_{vc}S_{cv} \tag{2.24}$$

Further, by definition of the core states,

$$H = \begin{pmatrix} \varepsilon_c 1 & \varepsilon_c S_{cv} \\ S_{vc}\varepsilon_c & H_{vv} \end{pmatrix}, \quad \varepsilon_c = diag(..., \varepsilon_s L_c, ...) \tag{2.25}$$

So, we can now re-write the secular equation as,

$$(S^L)^{-1} H (S^R)^{-1} (S^R C) = (S^R C)\varepsilon \tag{2.26}$$

which leads us finally to the reduced problem

$$\tilde{H}_{vv}\tilde{C}_{vv} = \tilde{C}_{vv}\varepsilon_v \tag{2.27}$$

with the definition

$$\tilde{H}_{vv} = (S^L_{vv})^{-1}(H_{vv} - S_{vc}H_{cc}S_{cv})(S^R_{vv})^{-1} \tag{2.28}$$

and

$$C = \begin{pmatrix} 1 & -S_{cv}(S^R_{vv})^{-1}\tilde{C}_{vv} \\ 0 & (S^R_{vv})^{-1}\tilde{C}_{vv} \end{pmatrix}. \tag{2.29}$$

The orthogonality condition for the core states is controlled during the successive interations.

2.5.2 Basis Optimization

One of the crucial features of the FPLO method is that, the basis states are readjusted at every iteration and is optimized in the course of the iteration. The core states obey the equation,

$$(\hat{t} + v^{at}_{\mathbf{s}})\phi_{\mathbf{s}}L_c = \phi_{\mathbf{s}}L_c\varepsilon_{\mathbf{s}}L_c \tag{2.30}$$

with $v^{at}_{\mathbf{s}}$ being the crystal potential spherically averaged around the site center $\mathbf{s}$. This assures that a Bloch sum of the core orbitals and the related core eigenvalues $\varepsilon_{\mathbf{s}}L_c$ are very good approximations to the solution of the true crystal Hamiltonian.

On the contrary, inorder to compress the long range tails, the valence orbitals are defined as:

$$\left(\hat{t} + v^{at}_{\mathbf{s}} + \left(\frac{r}{r_{\mathbf{s}}L_v}\right)^4\right)\phi_{\mathbf{s}}L_v\varepsilon_{\mathbf{s}}L_v \tag{2.31}$$

with $r_{\mathbf{s}}L_v = (r_{NN}(\mathbf{s})x_0L_v/2)^{\frac{3}{2}}$, where r_{NN} is the nearest neighbor distance and x_0L_v are dimensionless compression parameters. The seemingly strange scaling of the $r_{\mathbf{s}}L_v$ is the

correct one for an empty lattice. The power law potential has minor influence on the orbital in the core region, while in the region far away from the nucleus the orbitals undergo a drastic change, compared to solutions without the confining potential. To be precise, the valence orbitals are usually unbound states in the potential $v_{\mathbf{s}}^{at}$ alone. A second, even more important effect of the valence orbital confinement is that the orbital resonance energies are pushed up to come close to the band centers, providing the optimum curvature of the orbitals.

2.6 LDA+U

The density functional theory within the local spin density approximation (LSDA) has been highly successful for electronic structure calculations and zero temperature magnetic properties of non-correlated or weakly correlated systems. But the understanding and evaluation of electronic structure of strongly correlated systems is a long standing problem, and the transition metal oxides (which, in contrast with the observed insulating behavior, are incorrectly predicted to be metals or small gap semiconductors by LSDA) have represented for long time the most notable failure of DFT. One of the most popular approcahes to correct this deficiency is LDA+U, a method first suggested by Anisimov [7], for which a variety of different functionals were introduced and developed. The main idea of this approach is to correct the standard LDA energy functionals with a mean field Hubbard-like term which is meant to improved the description of the electron correlations. The formal expression of this additional energy functional is taken from the model hamiltonians (the Hubbard model is just one example) that represent the 'natural' theoretical framework to deal with strongly correlated materials. These models are however strongly dependent on the choice of the interaction parameters which sometimes have been evaluated using ab-initio (constrained) calculations.

Strongly correlated materials (usually systems with partially filled d or f valence shells belong to this family) are such that their electrons (or some of them) are supposed to spend their time in regions (around the ions) where the presence of other particles would make them feel strong Coulomb repulsion, thus making their motion 'correlated'. This is quite different from the scenario of a simple metal where electron-electron scattering is weak and particles spend vanishing amount of time in the regions around the ions. So, we have two extreme scenarios. When the kinetic energy is the dominant contribution, the electrons can overcome the on-site Coulomb cost and delocalize in extended states giving metallic behavior. On the other hand, when the bands in which they move are quite narrow, correlation wins and electrons actually localize in some regions, making the system acquire insulating character.

One way to introduce such a correction is essentially based on an Hartree-Fock (HF) like expression for the effective (screened) electronic interactions which is introduced as a mean field Hubbard-like correction to the standard exchange-correlation functionals. The starting point of the method is the description of the system within LDA which is supposed to contain (screened) correlations in some averaged way. This 'wrong' contribution is then subtracted from the energy functional and a correct term in which the correlations are supposed to be treated properly is added. The first expression of the LDA+U approach was formulated by Anisimov *etal*. [7, 8, 9]. Another important contribution was given by Pickett [10] and coworkers who, while slightly refining the functionals, introduced a linear response technique for calculating the Hubbard parameters. Despite some different details occuring among these approaches, the main physical idea behing them can be captured in

a very elementary formulation of the total energy functional:

$$E = E_{LDA} + \sum_I \left[\frac{U}{2} \sum_{m,\sigma \neq m',\sigma'} n_m^{I\sigma} n_{m'}^{I\sigma'} - \frac{U}{2} n^I (n^I - 1) \right] \tag{2.32}$$

where $n^I_{m\sigma} = n^I_{mm\sigma}$, $n^I = \sum_{m,\sigma} n^I_{m\sigma}$, U is the parameter (the Hubbard U) describing on-site correlations, the second term is the 'correct' on-site correlation functional (E_{hub}) and the third term is Mean Field (MF) approximation of the second term (E_{dc}), which modelling the LDA contribution to the on-site electronic interactions, has to be subtracted in order to avoid double counting. If we derive this equation with respect to the orbital occupation to obtain the corresponding orbital energy, we have:

$$\epsilon^I_{m\sigma} = \frac{\partial E}{\partial n^{I\sigma}_m} = \epsilon^{0I}_{m\sigma} + U \left(\frac{1}{2} - n^{I\sigma}_m \right) \tag{2.33}$$

(ϵ^0 is the corresponding LDA quantity) from which it is evident that a gap of width $\approx$ U opens between occupied ($n^I_i \approx 1$) and unoccupied ones ($n^I_i \approx 0$) orbitals. If we define the atomic orbital occupation as the projection of the occupied valence manifold over the corresponding atomic state ($n^I_{m\sigma} = \sum_{k,v} \langle \Psi^\sigma_{k,v} | P^I_m | \Psi^\sigma_{k,v} \rangle$) we can easily extract the potential entering the Kohn-Sham equation,

$$V|\Psi^\sigma_{k,v}\rangle = V_{LDA}|\Psi^\sigma_{k,v}\rangle + \sum_{I,m} U(\frac{1}{2} - n^I_{m\sigma}) P^I_m |\Psi^\sigma_{k,v}\rangle \tag{2.34}$$

From this expression we can see that if the occupation of a particular atomic orbital is initially larger than 1/2 then the Hubbard contribution to the potential is attractive and encourages the electrons to localize on that particular atomic state, whereas the opposite happens when the initial occupation is smaller than 1/2. In practical calculations, the final result does not actually depend very strongly on the initial conditions as occupations greatly evolve during the self consistent iterations with possible changes in the sign of the Hubbard potential. In the final self consistent configuration completely empty or completely filled atomic orbitals are not necessarily obtained because the LDA contribution to

the energy functional contains the competing factor (the tendency to minimize kinetic energy through delocalization) which sometimes could result stronger than the effect due to the Hubbard U term. Fractional occupation numbers for atomic orbitals around the fermi level is indeed the situation we would expect when applying this functional to a normal metal. Furthermore, even for localized electrons we could observe fractional $n_m^{I\sigma}$ because localization may occur on hybridized orbital built by d levels with states of the other atoms.

2.6.1 Rotationally Invariant Form

Despite the fact that this simple scheme already contains the main physical mechanism that could lead to gap openig in strongly correlated materials, it actually neglects the exchange coupling and the possible non spherical character of the effective interactions (the dependence of U on the magnetic quantum number m) entering the model. It's most serious inconsistency is that, the energy experssion is not invariant under rotation of the atomic orbital basis set used to define the occupancies $n_{i\sigma}^I$. To solve these problems, Anisimov and coworkers [11, 12] introduced a basis set independent formulation of LDA+U in which the E_{Hub} and E_{dc} are given a more general expression:

$$\begin{aligned} E_{Hub}[\{n^I_{mm'}\}] &= \frac{1}{2}\sum_{\{m\},\sigma,I}\{\langle m,m''|V_{ee}|m',m''\rangle n^{I\sigma}_{mm'}n^{I-\sigma}_{m''m'''} \\ &+ (\langle m,m''|V_{ee}|m',m'''\rangle - \langle m,m''|V_{ee}|m''',m'\rangle)n^{I\sigma}_{mm'}n^{I\sigma}_{m''m'''}\} \quad (2.35) \\ E_{dc}[\{n^I\}] &= \sum_I\left(\frac{U}{2}n^I(n^I-1) - \frac{J}{2}[n^{I\uparrow}(n^{I\uparrow}-1)+n^{I\downarrow}(n^{I\downarrow}-1)]\right) \quad (2.36) \end{aligned}$$

where U and I are screened Coulomb and exchange parameters. The V_{ee} integrals in eq. (2.35) describe the Coulomb interaction among (d) electrons sitting on the same site. Their expression is borrowed from the expansion of the $e^2/|r-r'|$ Coulomb potential in

terms of spherical harmonics,

$$\langle m, m''|V_{ee}|m', m'''\rangle = \sum_k a_k(m, m', m'', m''')F^k \tag{2.37}$$

where $0 \leq k \leq 2l$ (l is the angular moment of the Hubbard electrons) and

$$a_k(m, m', m'', m''') = \frac{4\pi}{2k+1} \sum_{q=-k}^{k} \langle lm|Y_{kq}|lm'\rangle\langle lm''|Y^*_{kq}|lm'''\rangle \tag{2.38}$$

The F^k coefficients, that in HF theory are the radial Slater integrals describing the electron-electron (bare) interaction, in the present formulation represent parameters to be related to the U and J of the LDA+U approach. For d electrons we just need F^0, F^2, and F^4 which can be related to the on sire and exchange interaction parameters as follows:

$$U = \frac{1}{(2l+1)^2} \sum_{m}, m'\langle m, m'|V_{ee}|m, m'\rangle = F^0 \tag{2.39}$$

$$J = \frac{1}{2l(2l+1)} \sum_{m\neq m', m'} \langle m, m'|V_{ee}|m', m\rangle = \frac{F^2 + F^4}{14} \tag{2.40}$$

where m and m' describe the electronic orbitals with the same l. In these formulae the V_{ee} integrals have the same angular dependence of HF electronic interactions, but they are evaluated using an indirect procedure which allows to account for the screening [13].

2.6.2 Double Counting

One of the main difficulties in LDA+U scheme is correcting for the double counting that arises from the fact that similar interactions are included in LDA. Presently, there are two schemes that are available and widely used. The first one is called 'Around Mean Field' (AMF) functional [14] and is zero if the orbitals of an atomic shell are equally occupied, hence it depends on the orbital polarization. It is given by:

$$e^{U,AMF} = \frac{1}{2} \sum_{R\sigma} \{U(N - \tilde{n}_\sigma) - J(N_\sigma - \tilde{n}_\sigma)\}N_\sigma \tag{2.41}$$

$$N_\sigma = \sum_\mu \tilde{n}_{\mu\sigma} = (2l+1)\tilde{n}_\sigma$$

N is the number of electrons occupying a whole correlated l - shell, N_σ is that for one spin sort, $\tilde{n}$ is the occupation matrix. As mentioned above, one weak point of this version is that it yields no contribution at all in the case of orbital-independent occupation numbers $\tilde{n}_{\mu'\sigma} = \tilde{n}_\sigma$. This is, for instance, the case of a half-filled completely spin polarized shell (e.g. $4f$-shell of Gd).

In order to provide a better description for systems like Gd, Czyżyk and Sawatzky [14] introduced another functional called 'Atomic Limit' (AL).

$$e^{U,AL} = e^{U,AMF} + \frac{1}{2}\sum_{R\sigma}(U-J)(1-\tilde{n}_\sigma)N_\sigma \tag{2.42}$$

The main characteristic of this functional is that, in case of an isolated shell, it moves the occupied states downward by (U - J)/2 and the unoccupied states upward by (U - J)/2 independent of the shell occupation. By way of contrast, the center of the AMF spin subshell potential split moves up with increasing subshell occupation (so that the shift of the occupied levels is zero in the case of a filled spin subshell and likewise the shift of the unoccupied levels of an empty spin subshell).

Chapter 3

Pressure Driven Nonmagnetic to Ferromagnetic Transition in CoN

3.1 Introduction

Transition metal oxides comprise perhaps the most thoroughly studied class of solids. Transition metal nitrides, which might be expected to retain several chemical and physical similarities to the oxides, have been studied far less. Although the mononitrides do show substantial structural similarities to the monoxides (rocksalt structure being common in both), their physical properties differ considerably. The main sources of these differences are the electronegativity, which is less for nitrogen than for oxygen, and the fact that nitrogen requires three extra electrons to form a closed shell whereas oxygen requires only two. Thus while insulating behavior, magnetic and metal-insulator transitions under doping, temperature, and pressure, and strongly correlated behavior are the norm in the monoxides, the mononitrides typically are standard metals.

Transition metal pnictides are attracting increased attention recently partially due to the discovery that CrAs can be synthesized in thin film form in the zincblende

(B3) structure, and that it is half metallic[15] and therefore a desirable candidate for spintronics applications. Several studies have appeared of transition metal pnictides including nitrides.[16] Although CoN has been known for almost 50 years, originally being reported in the NaCl (B1) phase (but off stoichiometry)[17] and confirmed to be cubic soon after[18], it has attracted little study until recently. The B1 structure was expected since *T*N, *T*= Sc, Ti, V, Cr, share that structure. Much more recently, however, Suzuki, Kaneko *et al.*[19] determined their materials to have the B3 structure, and later Suzuki, Shinohara *et al.*[20] demonstrated that they were Pauli paramagnetic metals. There has been conflicting information for other transition metal nitrides. FeN was reported by Suzuki, Morita *et al.*[21] to have a B3 structure, with evidence of a mictomagnetic state after field cooling. It was later reported by Suzuki, Yamaguchi *et al.*[22] that B3 FeN had no magnetic order down to 2.2 K. The B1 structure, with magnetic order, has also been reported for FeN, as discussed below.

Some time ago thin films of CoN_x were reported by Matsuoka, Ono, and Inukai.[23] Unlike the bulk materials of Suzuki *et al.*, their films were ferromagnetic and they reported hysteresis curves and coercive fields. Being film samples, it was not possible to determine the N concentration precisely or to obtain specific structural details. Very interestingly, the magnetic moment showed a strong perpendicular anisotropy, a property that has long been of great interest to the magnetic recording industry. The source of the magnetism, whether intrinsic, induced by strain, or induced by N vacancies, was not determined.

Theoretical studies of the electronic and magnetic properties of bulk CoN are few and rather cursory. Shimizu *et al.* presented a study[24] of the electronic, structural, and magnetic structure of several of the 3*d* transition metal oxides, but the electronic structure of CoN was only addressed briefly with a rigid band extrapolation from FeN. Eck *et al.* have presented[25] a related theoretical study of 3*d* metal nitrides, again focusing on iron

nitrides. Our study of these questions about CoN will extend earlier work on CrN and FeN. CrN transforms to a non-obvious antiferromagnetic phase at 280 K, accompanied by a shear distortion to an orthorhombic structure.[29] This phase is favored only slightly[30] over simple ferromagnetism, with the distortion playing a crucial role. Stoichiometric B1 FeN, on the other hand, was calculated to have a stable ferromagnetic phase,[31] in agreement some experimental data.[32] The difference between CrN and FeN was traced to the smaller ionicity and smaller moment of FeN. Experimentally, both structural choice and the magnetic order may be sensitive to deviations from stoichiometry.

The combination of the structural ambiguity of CoN, of the report of ferromagnetism, and the connection to B3 structure transition metal pnictides that suggest spintronics applications, has led us to make a detailed first principles study of the energetics and magnetism of CoN. We find that B3 CoN is strongly favored over the rocksalt at zero pressure, and we report the bulk modulus B and its pressure derivative for both phases. At 43 GPa pressure we predict a pressure driven nonmagetic-to-ferromagnetic first order transition to the rocksalt structure, which is unusual in the aspect of being a nonmagnetic-to-magnetic pressure-driven transition. The volume dependence of the moment in the rocksalt structure is illuminated by using fixed spin moment calculations.

3.2 Structure and Methods

The lattice structures of the B1 and the B3 type CoN are contrasted in Fig 3.1. The cobalt atoms in both these structures form an fcc lattice, but differ in the coordinations with the nitrogen atoms. The nearest neighbor N atoms in the B1 structure form an octahedron (sixfold coordinated) about the cobalt atom, while in the B3 structure, N atoms occupy the tetrahedral site (fourfold coordinated). Both the structures are a bipartite "AB" type fcc lattice, with different sublattice positions. The two structures are

related by a shift of the N (or Co) sublattice along a (111) direction. The distinct packing types lead to different equal-pressure volumes of around 20%.

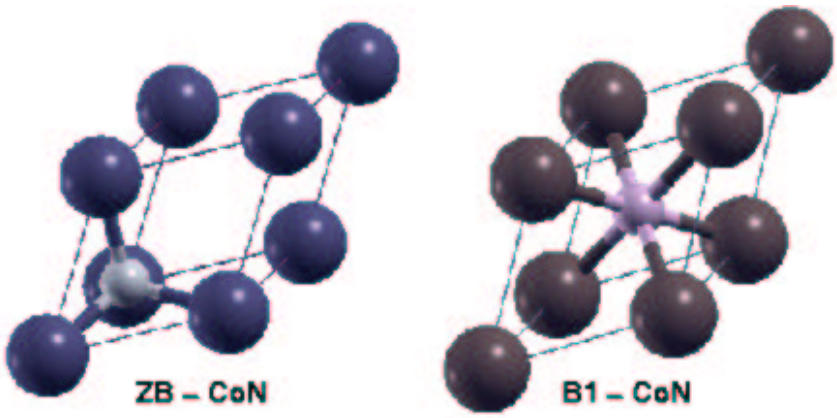

Figure 3.1. Structure, illustrating the coordination, of zincblende B3 CoN with tetrahedral coordination (left) and rocksalt B1 CoN with octahedral coordination (right). The big spheres are the Co atoms and the small spheres are the N atoms (although this viewpoint is interchangeable between the atoms). In each case the rhombus shaped primitive cell is pictured.

All calculations reported here have been performed using the full-potential linearized augmented plane wave code Wien2K[26], using both local density functional (LDA) and generalized gradient approximation (GGA), incorporated in the code for the exchange correlation potential. The muffin tin radii for Co and N have been set to 1.8 and 1.4 a.u. respectively for the ground state and all the high pressure calculations for both B1 and B3 structures. The basis set corresponding to RKmax = 7.0 was used for all calculations. The total energy and density of states (DOS) calculations were done with more than 1000 k-points in the irreducible ($\frac{1}{48}$) wedge of the Brillouin zone to attain good energy and charge convergence. The DOS has been calculated using the tetrahedral integration method. The energies were iterated to within 10^{-6} Rydberg convergence and the magnetic moments to within $0.01\mu_B$.

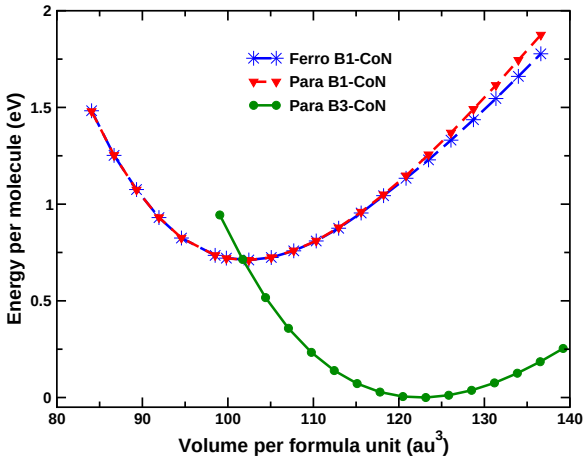

Figure 3.2. Calculated equations of state of CoN for the non-magnetic zincblende structure and both nonmagnetic and ferromagnetic B1 structure. The zincblende phase is the stable one at ambient pressure by almost 0.75 eV per cell.

3.3 Equation of State

3.3.1 Equation of State in LDA

To obtain the structural and magnetic properties of CoN, we performed total energy calculations using the LDA functional of Perdew and Wang[27] by varying the volumes for the non-magnetic B3 structure and both nonmagnetic and ferromagnetic B1 structure. The volumes were varied from $0.74V_\circ$ to $1.04V_\circ$ for the B3 case and from $0.64V_\circ$ to $1.04V_\circ$ for the B1 case. $V_\circ$ is the experimental equilibrium volume[19] of $a_\circ^3/4 = 134.3$ a.u.^{3} ($a_\circ$=4.297 Å). Results using the GGA functional will be presented in a following subsection.

The equations of state E(V) for the three cases are plotted in Fig 3.2. Contrary to the claim by Shimizu *et al.*[24] but in agreement with the conclusion of Eck *et al.*[25], the total energy of B3 CoN is lower than that of B1 CoN, thereby making the tetrahedrally coordinated structure stable at ambient temperature and pressure. The calculated equilibrium B1 lattice constant is 4.17 *Å*, 3% smaller than the experimental value[19]

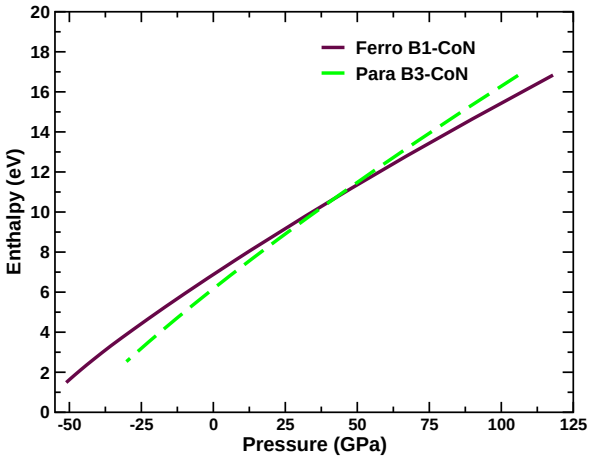

Figure 3.3. Plot of the enthalpy E+PV versus pressure for both phases of CoN, illustrating its continuity at the critical pressure P_c for the first order structural transition. Finding where the enthalpies are equal avoids having to perform the common-tangent construction to obtain P_c.

a_o= 4.297 $\AA$. For the B1 structure, the energy of the ferromagnetic state is lower than the nonmagnetic state for all volumes. Therefore, if B1-CoN is prepared, it will favor a magnetically ordered ground state. The equilibrium B1 lattice constant and magnetic moment are 3.92 $\AA$ and 0.22 μ_B respectively. The equilibrium volume for the B1 structure is 17% smaller than the B3 structure, reflecting the openness of the B3 structure. The possibility of magnetic order in the B3 structure was also investigated. Fixed spin moment calculations on this system showed no tendency to magnetism.

3.3.2 Transition Pressure

The equation of state E(V) curves shown in Fig 3.2 indicate a phase transition from the non-magnetic B3 phase to the ferromagnetic B1 phase under pressure. To facilitate the calculation of the transition pressure, the total energies were fitted to an equation of state. We have used Taylor series, Birch,[33] and Murnaghan[34] equations of state to compare the consistency of the values obtained. Here, we report the results of just the

Birch fitting

$$E(V) = E_c + \frac{9}{16} B V_\circ \left[v^{-2} \left(B' - 4 \right) + \left(3B' - 16 \right) v^{-\frac{2}{3}} + \left(14 - 3B' \right) v^{-\frac{4}{3}} \right]$$

$V_\circ$ represents the equilibrium volume of the unit cell, B is the bulk modulus and B' is its pressure derivative, both calculated at $V_\circ$. E_c is a constant and $v \equiv V/V_\circ$. The pressure is obtained by taking the volume derivative of the above equation. The next step is to calculate the enthalpy $E + PV$ of the two systems and the transition pressure (P_c) is the one at which the enthalpies are equal. The enthalpy-pressure relationship is presented in Fig 3.3 for both paramagnetic B3-CoN and ferromagnetic B1-CoN. The curves cross at P_c = 41 GPa. There is a 15% volume collapse at this pressure, where the structure changes from B3 to the denser (and magnetic) B1 phase.

3.3.3 Corresponding Results using GGA

It is generally found that the GGA functional for the exchange-correlation energy gives a more accurate equilibrium volume and equation of state than does LDA. For this reason all the total energy calculations were repeated using the GGA functional of Perdew, Burke, and Ernzerhof.[28] The calculated equilibrium lattice constants are (quoting GGA versus LDA): 4.25 Å versus 4.17 Å for the B3 phase, a 1.9% increase; 4.02 Å versus 3.92 Å for the rocksalt phase, a 2.5% increase. Thus GGA brings the calculated lattice constant to within 1% of the experimental value.

Applying the same procedures as described above to get enthalpy-pressure relationships, the transition pressure was increased from 41 GPa (LDA) to 43 GPa (GGA). This small change reflects that the volume increase given by GGA is similar for the two

Table 3.1. Bulk modulus B (GPa) and its pressure derivative B′, contrasting LDA and GGA results. GGA gives a larger volume and a corresponding softer lattice as usual.

	LDA		GGA	
	B	B'	B	B'
B1 CoN	347	5.4	275	4.8
B3 CoN	305	4.5	260	4.2

crystal structures, leaving a common tangent (whose slope is -P_c) with little change. The equilibrium moment of the ferromagnetic B1-CoN is 0.12 μ_B in GGA, roughly half of the LDA value in spite of the larger volume. This decrease was unexpected, since simple increase of the volume usually decreases the bandwidth and increases the tendency toward magnetism as reflected in the enhanced magnetic moment.

3.4 Moment Collapse in the Rocksalt Phase

Applying pressure to any structure with magnetic order increases the bandwidth and almost always decreases the moment of the system. Figure 3.4 shows the moment vs. volume M(V) curve of the ferromagnetic B1 CoN phase. A striking feature of M(V) is the collapse of the moment around 0.98 V_o, which results from a first order magnetic transition where the moment jumps from 0.9 μ_B to 0.4 μ_B. To better understand the mechanism of collapse of the moment, we carried out fixed spin moment calculations[35] for the 0.97 V_o case. The resultant energy vs. moment is plotted in Fig. 3.4. We observe two energy minima for the system with very small energy difference. As the volume changes, the energies if these two local minima vary, and where they become equal a first order magnetic transition occurs. In this case it is a moment collapse, 0.9 $\rightarrow$ 0.4 μ_B.

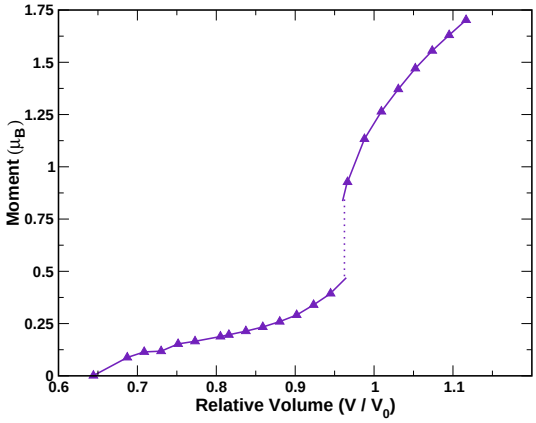

Figure 3.4. Moment versus volume relationship for ferromagnetically ordered B1 CoN. Around the critical volume of 0.98V_o the moment collapses from 0.9 to 0.4 μ_B. The corresponding energy curve E(M) from the fixed spin moment method is shown in Fig. 3.5. The equilibrium volume $V_\circ$ is given in the text.

Note that this volume range is where the B3 structure is stable, hence this collapse is not accessible to experiment.

From the plot of the density of states in the high moment phase at 0.96$V_\circ$ in Fig. 3.6, one can see a peak very close to and above the Fermi energy for the minority spin. The contribution to that peak arises from Co t_{2g} states. Applying pressure to reduce the volume (which decreases the magnetization) moves the peak to lower energy, thereby bringing the peak of the Co t_{2g} states right on top of the Fermi energy. This high density of states at the Fermi energy is energetically unfavorable enough that the system undergoes a first order transition to move the peak below the Fermi energy, rather than to move the Fermi level precisely onto the peak. This jump in the filling of states changes the moment discontinuously, thus revealing the driving force for the moment collapse. The energy barrier is quite small, ∼0.1-0.2 meV/cell, accounting for our failure to observe hysteresis.

It is worthwhile to clarify an unexpected feature in the DOS of Fig. 3.6, the lack of N $2p$ character in the energy region -3 eV to -1 eV in the majority bands, and the

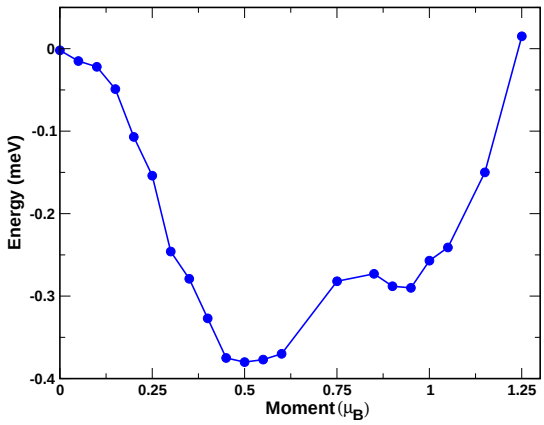

Figure 3.5. The energy versus fixed (imposed) spin moment for rocksalt CoN at $0.97V_o$. The double minimum structure reveals the cause of the moment collapse in Fig. 3.4: as the volume changes, the positions of the minima remain fixed but the energies at the minima change, and the volume at which the minima are degenerate marks the critical volume. Note the very small energy scale, which accounts for the calculated values not lying on a completely smooth curve.

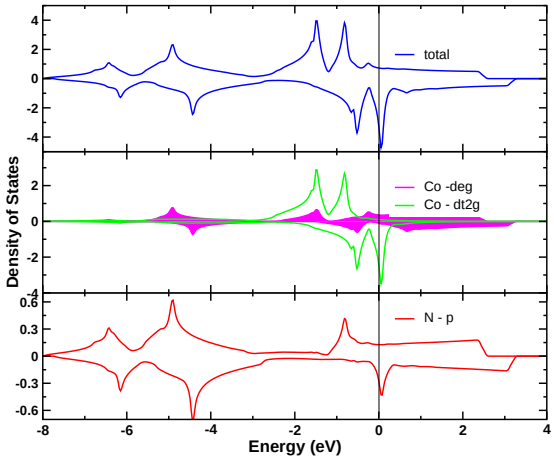

Figure 3.6. Total and partial density of states (DOS) of ferromagnetic rocksalt structure CoN for V = 0.96 $V_\circ$. *Top panel*: total DOS; the peak in the minority (plotted downward) states is responsible for the moment collapse (see text). Middle panel: Co e_g and t_{2g} DOS, illustrating that the peak is due to the t_{2g} states. *Bottom panel*: the N $2p$ DOS, illustrating strong hybridization with both e_g and t_{2g} states of Co.

corresponding region about 1 eV higher in the minority DOS – this is the lower of the two t_{2g} DOS peaks. This void is unexpected because the N $2p$ states clearly do mix with the Co t_{2g} states as is clear from the corresponding peaks in the respective DOS in Fig. 3.6 (near -1 eV in the majority, and the important peak at E_F in the minority that was discussed above). To illustrate the origin of the effect, the majority bands are presented in Fig. 3.7 with N $2p$ character emphasized. At the zone center Γ, the $3d$ and $2p$ states are close in energy with the $3d$ states lying below the $2p$ states. The $2p - e_g$ hybridization is large, and it results in the 10.5 eV total bandwidth. The t_{2g} bandwidth itself is narrow, less than 2 eV as shown in Fig. 3.6, and the coupling tends primarily to repel the N $2p$ character away, and $2p - t_{2g}$ hybridization survives only in the upper of the two t_{2g} peaks.

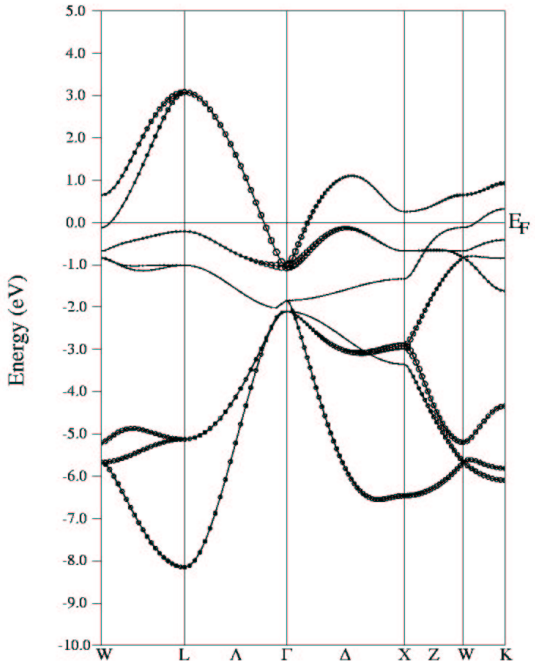

Figure 3.7. Majority band structure of ferromagnetic B1 CoN along high symmetry directions. The symbol size if proportional to the N $2p$ character. As discussed in the text, N $2p$ character is excluded from the region -2.5 eV to -1.3 eV by $t_{2g} - 2p$ mixing and resulting repulsion.

3.5 Conclusions

This study has cleared up several features in the experimental data for CoN. From total energy calculations, it has been established that CoN takes a paramagnetic zincblende structure at ambient pressure, rather than rocksalt as sometimes suggested. Around 43 GPa we predict a first order phase transition to the denser rocksalt phase, which at this volume has a small but clearly nonvanishing ferromagnetic moment of 0.1 μ_B per Co. Thus pressure drives the system into a weak ferromagnetic phase that is relatively close to a quantum critical point (QCP). Our calculations predict this QCP, where the Curie temperature finally goes to zero, to be $P_{qcp} = 176$ GPa. Fluctuations should renormalize P_{qcp} to a lower value.

Our work has not explained the observation of ferromagnetic films by Matsuoka *et al.*[23] Strain, nonstoichiometry, or even the altered chemistry of the open-shell transition metal atom and the N atom at the surface, may be factors. Strain can change the in-plane lattice constant, however the tendency to conserve volume will cause the perpendicular lattice constant to compensate and there may be much less reduction in volume than the in-plane lattice alone would suggest. Nonstoichiometry is an obvious concern; since Co itself is ferromagnetic, regions with decreased N content, or N-free Co clusters, will tend to be ferromagnetic. Finally, even at perfect stoichiometry, the presence of the surface can alter the chemistry considerably. At the Mn-terminated (001) surface of $CaMnO_3$, for example, the coupling between subsurface and surface Mn ions was found to become ferromagnetic,[36] rather than the antiferromagnetic coupling of the bulk. It is likely to require further study both experimentally and theoretically to resolve the origin of the magnetism of CoN films.

Chapter 4

Mott Transition of MnO under Pressure

4.1 Introduction

For fifty years the metal-insulator transition has been one of the central themes[37] of condensed matter physics. The type we address here does not involve spatial disorder nor change of the number of charge carriers per cell; the competing tendencies arise solely from the kinetic and potential energies in the Hamiltonian, favoring itineracy and localization respectively, and the many real-material complexities that arise. The classic categorization is that of the Mott transition, treated in its most basic form with the single-band Hubbard model. In the past half-century much has been learned about this model, but there are very few physical systems that are modeled faithfully by such a model. Real materials involve multiorbital atoms and thus extra internal degrees of freedom, and an environment that is often very active and may even react to the configuration of active sites.

MnO is a transition metal monoxide (TMO) with open $3d$ shell that qualifies as

one of the simpler realizations of a prototypical, but real, Mott insulator. It is, certainly, a multiorbital system with the accompanying complexities, but the half-filled $3d$ bands lead to a spherical, spin-only moment at ambient pressure. Applying pressure to such a system leads to a number of possibilities, including insulator-metal transition, moment reduction, volume collapse if a first-order transition (electronic phase change) occurs, and any of these may be accompanied by a structural phase transition, that is, a change in crystal symmetry. The $3d$ band width W of such a Mott insulator is very susceptible to applied pressure, and is one of the main determining factors of the strength of correlation effects.

While "closed subshell" MnO may seem to be one of the simpler $3d$ monoxides, it is actually not at all simple, moreover it is not typical of a $3d$ monoxide. The half-filled shell aspect is what makes it atypical, as shown for example by Saito *et al.*, who compiled[38] effective parameters for this system from spectroscopic information. An effective intra-atomic Coulomb repulsion energy as defined by them, for example, is roughly twice as large as for the other $3d$ monoxides.

The complexity that should be expected can be considered in terms of the energy scales that are involved in the electronic structure and magnetism of these oxides. These include the $3d$ bandwidth W, an intra-atomic Coulomb repulsion strength U, an intra-atomic $d-d$ exchange energy (Hund's rule J, or exchange splitting Δ_{ex}), the crystal field splitting $\Delta_{cf} = \varepsilon_{e_g} - \varepsilon_{t_{2g}}$, and the charge transfer energy $\Delta_{ct} \equiv \varepsilon_d - \varepsilon_p$ (the difference in mean Mn $3d$ and O $2p$ site energies). In the magnetically ordered antiferromagnetic (AFM) state, there is further symmetry lowering and ligand field subsplittings involving $3d-2p$ hybridization. All of these scales change as the volume changes, making the pressure-driven Mott transition a challenging phenomenon to describe.

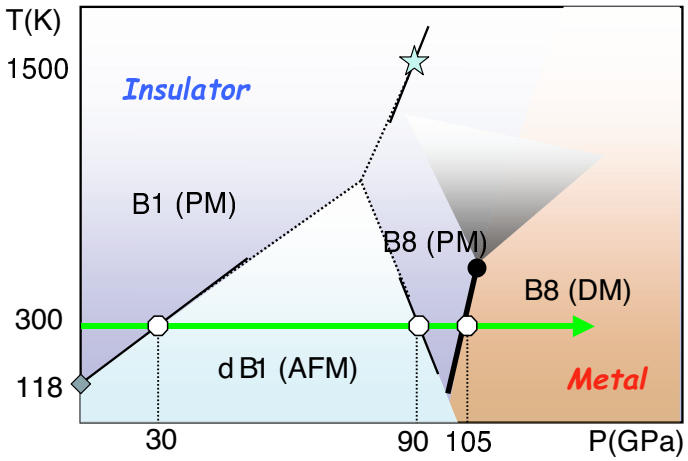

Figure 4.1. The conceptual phase diagram of MnO based on recent high pressure work at Lawrence Livermore National Laboratory.[39, 40] The thick phase line signifies the first-order Mott transition which simultaneously accompanies the loss of Mn magnetic moment, a large volume collapse, and metalization. This transition should end at a critical point (solid circle). The gray fan above the critical point signifies a region of crossover to metallic behavior at high temperature. Only the distorted B1 (dB1) phase is magnetically ordered.

It is useful first to recount what is known about the Mott transition at this time. The current experimental information, mostly at room temperature, on the behavior of MnO under pressure is summarized in Fig. 4.1. Resistance measurements[39] provided the first evidence of the Mott transition in MnO near 100 GPa. Recent x-ray diffraction and emission spectroscopy measurements of the crystal structure and magnetic moment by Yoo *et al.*[40] have clarified the behavior. Around 90 GPa there is a structural transformation from the distorted B1 (rocksalt) phase to the B8 (NiAs) structure. This structure change is followed at 105 GPa by the Mott transition, consisting of a simultaneous volume collapse and moment collapse signifying a qualitative change in the electronic structure of the compound. A related phase diagram is seen in the lanthanide and actinide volume collapse transitions, with "metalization" defined in terms of the f spectral weight.

On the theoretical side, little is known about how the Mott transition occurs in a real multiband TMO in spite of the extensive studies of the Mott transition in the single-band Hubbard model, which has a simple spin-half moment at strong coupling and half-filling. The numerous energy scales listed above, and the S=$\frac{5}{2}$ moment on Mn arising from the five $3d$ electrons, allow for many possibilities for how the moment might disintegrate as the effective repulsion decreases. The high pressure limit is clear: a nonmagnetic $3d-2p$ band metal in which kinetic energy considerations overwhelm potential energy. This is the competition that is studied in the (simplified) Hubbard model. The multiband nature has attracted little attention until recently, when for example the question of possible orbital-selective Mott transitions[41, 42] have aroused interest. One can imagine one scenario of a cascade of moment reductions S = $\frac{5}{2} \rightarrow \frac{3}{2} \rightarrow \frac{1}{2}$ before complete destruction of magnetism, as electrons use their freedom to flip spins (as some competing energy overcomes Hund's rule, for example). In such a scenario there is the question of which orbital flips its spin at each spinflip, which involves a question of orbital selection and ordering. At each flip the system loses exchange (potential) energy while gaining kinetic energy (or correlation energy through 'singlet' formation). The manner in which kinetic energy changes is difficult to estimate because subband involvement means that there is no longer a single bandwidth W that is involved. The increasing hybridization with O $2p$ states under pressure strongly affects the kinetic energy, directly and through superexchange (a kinetic energy effect).

It has been known for decades that the conventional band theory (local density approximation [LDA]) that does so well for so many materials gives poor results for $3d$ monoxides in many respects, and some predictions are qualitatively incorrect (*viz.* no band gap when there should be a large gap of several eV). Thus even at the density functional level (ground state energy, density, and magnetization) some correlated approach is

required. In the past fifteen years several approaches, which we refer to as correlated band theories, have been put forward, and each has had its successes in providing an improved description of some aspects of correlated TMOs. Although commonly called mean-field approaches with which they share many similarities, they are not mean-field treatments of any many-body Hamiltonian. Rather, they are energy functionals based on the complete many-body Hamiltonian, which must then be approximated due to limited knowledge of the exchange-correlation functional.

4.2 Structure and Symmetry

Density functional theory, like Hartree-Fock theory, deals in its most straightforward form with ground state properties, *i.e.* zero temperature. The ground state is known to be the AFMII phase in which $< 111 >$ layers have spins aligned, and successive layers are antiparallel. The resulting symmetry is rhombohedral, with Mn$\uparrow$ and Mn$\downarrow$ being distinct sites (although related through a translation + spin-flip operation). Thus, while most of the lore about transition metal monoxides is based upon cubic symmetry of the Mn (and O) ion, in the ordered state the electronic symmetry is reduced. It is obvious that individual wavefunctions will be impacted by this symmetry, *viz.* fourfold symmetry around the cubic axes is lost. It has been emphasized by Massidda *et al.*[43] that zone-integrated, and even spin-integrated, quantities show the effects of this symmetry lowering; for example, Born effective charges lose their cubic symmetry. Since this issue arises in the interpretation of our results, we provide some background here.

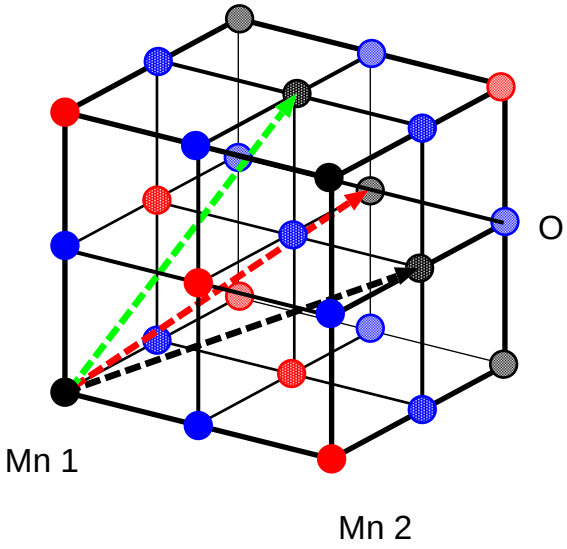

Figure 4.2. The AFMII phase of MnO. Here, the black spheres correspond to Mn atoms of one spin arrangement (let's say, *spin up*), while the red spheres are Mn atoms with the opposite spin arrangement (let's say, *spin down*) and the blue spheres are the oxygens

In cubic symmetry the Mn $3d$ states split into the irreducible representations denoted by t_{2g} and e_g. Rhombohedral site symmetry results in the three irreducible representations a_g, $e_{g,1}$, and $e_{g,2}$, the latter two being two fold degenerate. The coordinate rotation from cubic to rhombohedral (superscript c and r respectively) is, with a specific choice for the orientation of the x and y axes in the rhombohedral system,

$$\begin{pmatrix} x^r \\ y^r \\ z^r \end{pmatrix} = \begin{pmatrix} \frac{1}{\sqrt{6}} & \frac{1}{\sqrt{6}} & -\frac{\sqrt{2}}{\sqrt{3}} \\ -\frac{1}{\sqrt{2}} & \frac{1}{\sqrt{2}} & 0 \\ \frac{1}{\sqrt{3}} & \frac{1}{\sqrt{3}} & \frac{1}{\sqrt{3}} \end{pmatrix} \begin{pmatrix} x^c \\ y^c \\ z^c \end{pmatrix}$$

Applying this rotation of coordinates gives the $3d$ orbitals in the rhombohedral frame in

terms of those in the cubic frame ($d_{z^2} \equiv d_{3z^2-r^2}$):

$$d^r_{xy} = \frac{1}{\sqrt{3}}\left(d^c_{xz} - d^c_{yz} - d^c_{x^2-y^2}\right) \quad (4.1)$$

$$d^r_{yz} = \frac{1}{\sqrt{6}}(d^c_{yz} - d^c_{xz}) - \sqrt{\frac{2}{3}}d^c_{x^2-y^2} \quad (4.2)$$

$$d^r_{xz} = \frac{\sqrt{2}}{3}d^c_{xy} - \frac{1}{3\sqrt{2}}(d^c_{xz} + d^c_{yz}) - \frac{\sqrt{2}}{\sqrt{3}}d^c_{z^2} \quad (4.3)$$

$$d^r_{x^2-y^2} = -\frac{1}{3}(d^c_{xz} + d^c_{yz} + \frac{2}{3}d^c_{xy}) - \frac{1}{\sqrt{3}}d^c_{z^2} \quad (4.4)$$

$$d^r_{z^2} = \frac{1}{\sqrt{3}}(d^c_{xy} + d^c_{yz} + d^c_{xz}). \quad (4.5)$$

In rhombohedral coordinates it is useful to categorize the $3d$ orbitals in terms of their orbital angular momentum projections along the rhombohedral axis: $d^r_{z^2} \leftrightarrow m_\ell = 0$; $d^r_{xz}, d^r_{yz} \leftrightarrow m_\ell = \pm 1$; $d^r_{xy}, d^r_{x^2-y^2} \leftrightarrow m_\ell = \pm 2$. It is easy to see that $|m_\ell|$ specifies groups of states that only transform into combinations of themselves under trigonal point group operations.

Note that the unique a_g symmetry state in rhombohedral coordinates is the fully symmetric combination of the cubic t_{2g} states. The other two irreps are both e_g doublets. While $|m_\ell| = 1$ and $|m_\ell| = 2$ form representations of these irreps, if there are components of the crystal field that are not diagonal in the L=(2,m_ℓ) basis, these states will mix. Then each of the resulting (orthonormal) irreps $e_{g,1}$, and $e_{g,2}$ will contain both $|m_\ell| = 1$ and $|m_\ell| = 2$ components. Such mixing does occur in MnO and complicates the symmetry characterization of the $3d$ states.

4.3 Previous Electronic Structure Studies

The origin, and the proper description, of the moments and the band gaps in transition metal monoxides have been of interest for fifty years. The earliest question centered on the connection between the antiferromagnetic (AFM) order and the insulating behavior. Slater's band picture[46] could account in a one-electron manner for a gap arising

from AFM order, whereas Mott's picture of correlation-induced insulating behavior[47] was a many-body viewpoint with insulating behavior not connected to the magnetic order. The proper general picture in these monoxides arose from studies of transport above the Néel temperature and with introduction of defects, giving them the designation as Mott insulators.

Much progress on the understanding of MnO and the other monoxides came from early studies using LDA. While understanding that LDA does not address the strong correlation aspect of the electronic structure, Mattheiss[48] and Terakura *et al.*[49] quantified the degree and effects of $3d-2p$ interactions, and pointed out the strong effect of magnetic ordering on the band structure. More recently, Pask and collaborators[50] have studied the structural properties, and the rhombohedral distortion, with LDA and GGA approximations. The symmetry lowering and resulting structure is described well, and in addition they found that AFM ordering results in significant charge anisotropy. Effects of AFM order were further probed by Posternak *et al.* by calculating and analyzing maximally localized Wannier functions for the occupied states.[51]

The application of correlation corrections in MnO already has a colorful history. The first work, by Svane and Gunnarsson[53] and by Szotek *et al.*,[52] was in the application of the SIC-LSD method. The former pair correctly obtained that MnO, FeO, CoO, NiO, and CuO are AFM insulators, while VO is a metal. They calculated a gap of 4 eV for MnO. Szotek *et al.* used a fairly different implementation of the SIC-LSD approach but find a similar gap (3.6 eV). Their $3d$ states lay about 6 eV below the center of the $2p$ bands, although hybridization was still clearly present. In this same time frame, Anisimov, Zaanen, and Andersen introduced[7] the LDA+U method with application to the transition metal monoxides. They obtained a band gap of 3.5 eV but few other results on MnO were reported.

Kotani implemented[54, 55, 56] the "DFT exact-exchange" method of Talman and Shadwick[57] to crystal calculations. This method consists of taking the Fock expression for the exchange energy in the DFT functional, then performing a Kohn-Sham solution (minimization), giving a local exchange potential ("optimized effective potential"). In Kotani's results for MnO, the Mn e_g and t_{2g} bands form very narrow (almost atomic-like) bands between the occupied O $2p$ bands and the conduction bands. Takahashi and Igarashi[58] proposed starting from the Hartree-Fock exchange and adding correlation from a local, three-body scattering viewpoint. Their corrections were built on a parametrized tight-binding representation, and they obtained small self-energy corrections for MnO, much smaller than they obtained for the other transition metal monoxides.

The effective potential approach used by Kotani was extended by Solovyev and Terakura[59] in an unconventional way. They obtained an effective potential using the criterion that it had to reproduce the spin-wave spectrum, *i.e.* that it had to describe the magnetic interactions correctly. They found clear differences when comparing to the LDA+U and the optimized effective potential results, and discussed limitations of the one-electron band method itself.

More recently, Savrasov and Kotliar applied a dynamical extension[60] of the LDA+U method (dynamical mean field theory) to MnO and NiO. Being a self-energy method, this is not really a correlated band theory. For the properties they calculated (band gap, effective charges, dielectric constant, optic phonon frequencies) the dynamical results are similar to the LDA+U results and differ considerably from LDA values.

Even though hybrid-exchange DFT applications to solids are still in their infancy, there have been two previous studies of MnO. The first, by Bredow and Gerson,[61] utilized the B3LYP hybrid functional. Unlike the LDA and GGA, they found B3LYP provided an excellent band gap for MnO. More recently, Franchini *et al.* have examined MnO in more

detail using the PBE0 approximation.[62] They also found a gap, lattice constant and density of states in quite good agreement with experiment. In particular, the distorted dB1 rhombohedral structure was determined to be the minimum energy geometry, in agreement with experiment. Neither the B3LYP nor the PBE0 approximation can be applied to the metallic side of the transition of interest here. For that, we must turn to the screened hybrid-exchange of HSE.

Therefore, while there has been thorough LDA studies of MnO and a variety of approaches to treatment of the correlation problem, nearly all of these have considered only ambient pressure or small variations of the volume near zweo pressure. The work described in the following sections focuses on using the LDA+U correlated band method from ambient conditions to high pressures, through the volume collapse regime, to see whether some base foundation can be laid for the understanding and theoretical description of pressure-driven Mott transitions in real materials.

The results are organized as follows: First, I will present the LDA results at ambient conditions, in the AFMII rocksalt phase to help us orient ourselves, and follow it up in the next section with LDA+U results as a function of pressure, still limiting the analysis to the AFMII rocksalt (NaCl) phase, since it undergoes a first-order transition in both moment and volume. Later, i will add the LDA+U results of the high pressure NiAs phase, to compare and contrast with the experiemental findings. By definition of the Hubbard 'U' in the LDA+U functional, the choice of 'U' regulates the possible states that are obtained from a self-consistent calculation. Bearing that in mind, i will also provide the effects of U on these transitions.

4.4 LDA Calculations

For LDA band structure plot (Fig. 4.3) we used version 5.20 of the full-potential local orbital band structure method (FPLO[5, 44]). Relativistic effects were incorporated on a scalar-relativistic level. We used a single numerical basis set for the core states (Mn $1s2s2p$ and O $1s$) and a double numerical basis set for the valence sector including two $4s$ and $3d$ radial functions, and one $4p$ radial function, for Mn, and two $2s$ and $2p$ radial functions, and one $3d$ radial function, for O. The semi core states (Mn $3s3p$) are treated as valence states with a single numerical radial function per nl-shell.

4.4.1 Baseline: LDA Bands

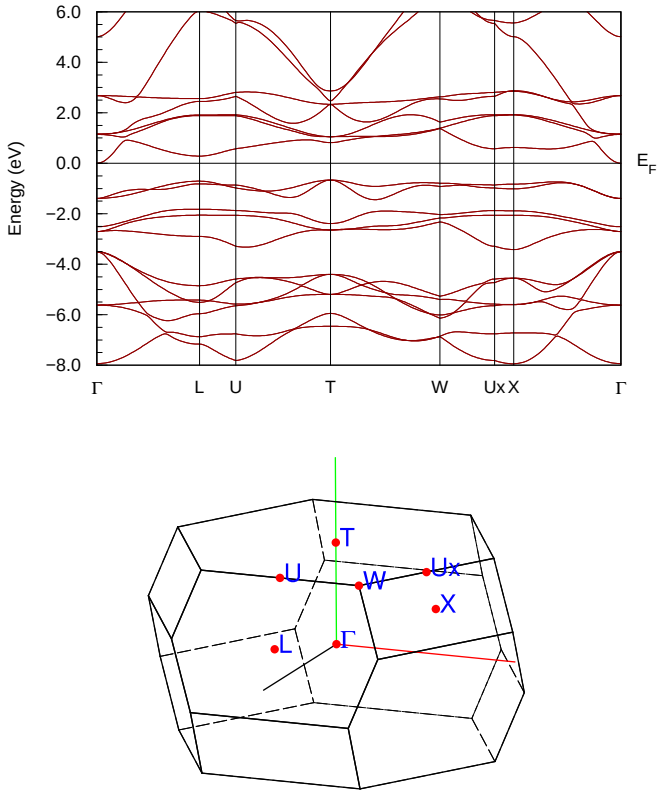

Figure 4.3. *Top*: LDA band structure of AFM MnO along rhombohedral symmetry lines, calculated with the FPLO method[5, 44], with horizontal line ("Fermi level") placed at the top of the gap. The Γ-T lies along the rhombohedral axis, while Γ-L lies in the basal plane. The O 2*p* bands lie in the -8 eV to -3.5 eV range, with the majority Mn 3*d* bands just above (-3 eV to -1 eV). The five minority 3*d* bands are just above the gap. Note the small mass, free-electron-like band that lies below the unoccupied 3*d* bands at the Γ point. *Bottom*: The high symmetry points in the rhombohedral brillouin zone, depicted here for better understanding the band structure

The LDA (uncorrelated) band structure of AFM MnO is shown in Fig. 4.3 as the reference point for the following calculations. There is a band gap of $\sim$ 0.7 eV.

The five bands immediately below the gap are the majority Mn $3d$ bands, those lying below are the O $2p$ bands. The charge transfer energy mentioned in the Introduction is $\Delta_{ct} = \varepsilon_d - \varepsilon_p = 6$ eV, and the exchange splitting is $\approx$3.5 eV. It is tempting to interpret the 3+2 separation of occupied $3d$ states as $t_{2g} + e_g$, but the rhombohedral symmetry renders such a characterization approximate. The five bands above the gap are primarily the minority Mn $3d$ bands. However, a free-electron-like band at Γ lies lower in energy than the $3d$ bands, but disperses upward rapidly, so over most of the zone the lowest conduction band is Mn $3d$ and the gap is 1 eV. The presence of the non-$3d$ band does complicate the interpretation of the band gap.

4.4.2 Energetics under pressure

The LDA energetics, band gap and Mn moments as a function of pressure are displayed in Fig.4.4. With pressure the moment on the Mn sites decrease continously, though around $0.7\mathrm{V}_0$, the rate is a bit steeper, indicative of a possible transition. The total energy curves also show a change of curvature close to $0.68\mathrm{V}_0$, consistent with the moment picture. With pressure, the LDA band gap closes within less than 20% of the volume reduction.

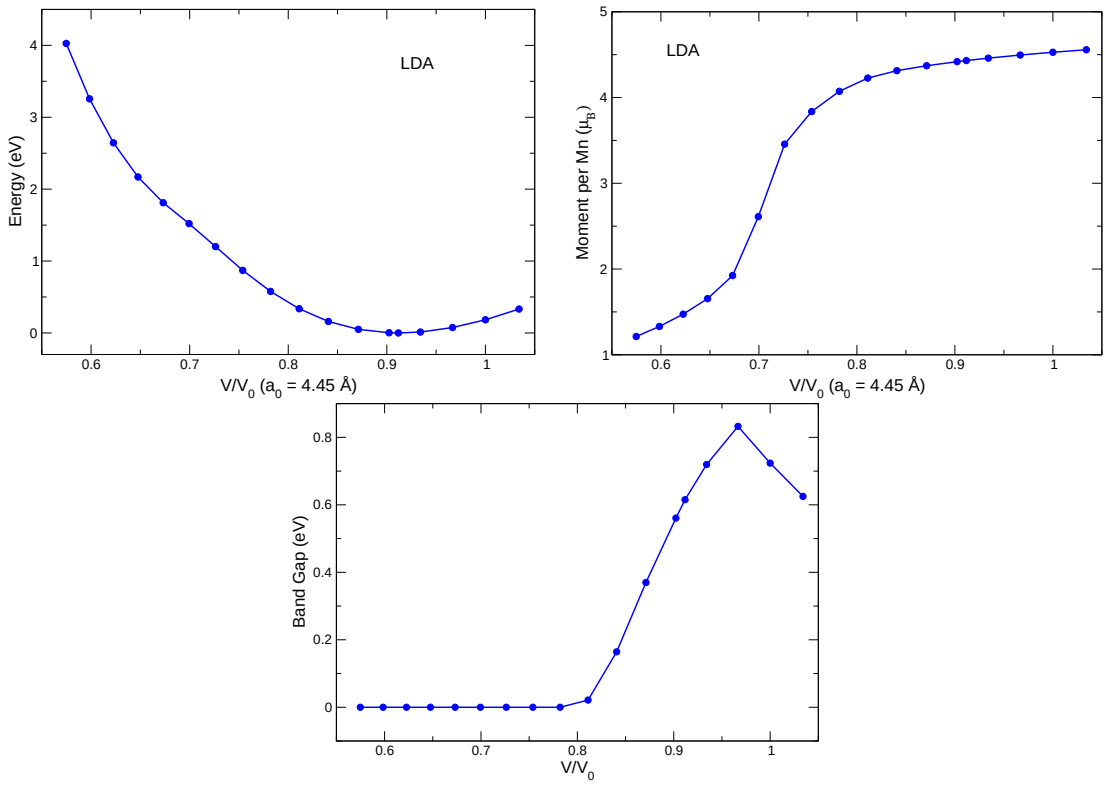

Figure 4.4. *Top Left*: The calculated LDA total energy versus volume for rocksalt MnO. *Top Left*: Change in moment on the Mn site as a function of pressure. *Bottom*: LDA band gap for MnO versus volume

The behavior of MnO under compression within GGA has been given earlier by Cohen, Mazin, and Isaak.[64] They obtained an equilibrium volume 2% higher, and bulk modulus 13% smaller, than measured. Pressure studies including extensive structural relaxation have also been provided by Fang *et al.*[65] Their structural relaxations make their study more relevant (within the restrictions of GGA) but also make comparison with our (structurally restricted) results impossible.

4.5 LDA+U Method

The LDA+U approach of including correlation effects is to (1) identify the correlated orbital, $3d$ in this case, (2) augment the LDA energy functional with a Hubbard-like term (Coulomb repulsion U) and Hund's (exchange J) energy between like spins, (3) subtract off a spin-dependent average of this interaction energy to keep from double-counting repulsions (once in LDA fashion, once in this U term), and (4) include the correlated orbital occupation numbers in the self-consistency procedure, which leads to an orbital-dependent Hartree-Fock-like potential acting on the correlated orbitals. The addition to the energy functional has the schematic form

$$E_U = \frac{1}{2}{\sum}'(U - J\delta_{\sigma\sigma'})[n_{m\sigma}n_{m'\sigma'} - \bar{n}_\sigma\bar{n}_{\sigma'}]. \tag{4.6}$$

where the primed-sum is over all indices $m\sigma \neq m'\sigma'$.

We actually use the coordinate-system independent form of LSDA+U [45, 12, 14] implemented in FPLO,[5] which leads to four m indices on U and J which for simplicity have not been displayed (nor has the full off-diagonal form of the occupation matrices $n_{mm'\sigma}$). This treatment of the on-site interactions U and J incorporates on-site correlation effects in the Mn 3d-shell. We have used the so called 'atomic-limit' (strong local moment) form of the double-counting correction, the last term in Eq. 4.6. This form is appropriate for the high-spin state, but it is less obviously so for the low-spin state that is found at reduced volumes. The Slater parameters were chosen according to $U = F_0 = 5.5$ eV, $J = \frac{1}{14}(F_2 + F_4) = 1$ eV and $F_2/F_4 = 8/5$. (The choice of the value of U and possible ways to evaluating them will be addressed later)

The shape of the basis orbitals has been optimized yielding a sufficient accuracy of the total energy over the range of geometries considered in this work. The **k**-integrals are performed via the tetrahedron method with an irreducible mesh corresponding to 1728

(12^3) points in the full Brillouin zone.

4.5.1 Rocksalt (NaCl) AFMII MnO:

Energetics and Equation of State

The equation of state (EOS) energy vs. volume curve obtained from the LDA+U calculations are shown in Fig. 4.5. We obtain a large volume, high-spin (S = $5\mu_B$) state and a small volume, low-spin (S = $1\mu_B$) state. The analysis to obtain the first-order volume collapse transition was done as follows. For the high volume and low volume phase separately, an EOS function $E_{h,l}(V)$ was determined (h, l=high, low) by a fit to the Murnaghan equation. Both fits give minima, with the most relevant one being for the high spin phase and being the predicted equilibrium volume V_0^{th}. The pressure is obtained from the volume derivative of the EOS, then is inverted to give $V(P)$. Then equating the enthalpies $E[V(P)] + PV(P)$ of the two phases gives the critical pressure P_c. The volumes at this pressure then give the volume collapse $\Delta V = V_h(P_c) - V_l(P_c)$. The various quantities from our computational scheme are given in Table 4.1, along with the uncorrelated results of Cohen *et al.*[64] The equilibrium volume from the LDA+U method is smaller than the experimental volume and hence over binding. We obtain a volume collapse of nearly 5.4% within the rocksalt phase (Yoo and coworkers [40] observed a 6.6% isostructural volume collapse around 110 GPa, though within the NiAs (B8) phase). The critical pressure P_c = 123 GPa, and is fairly comparable to that of the GGA work of Cohen *et al.*[64]

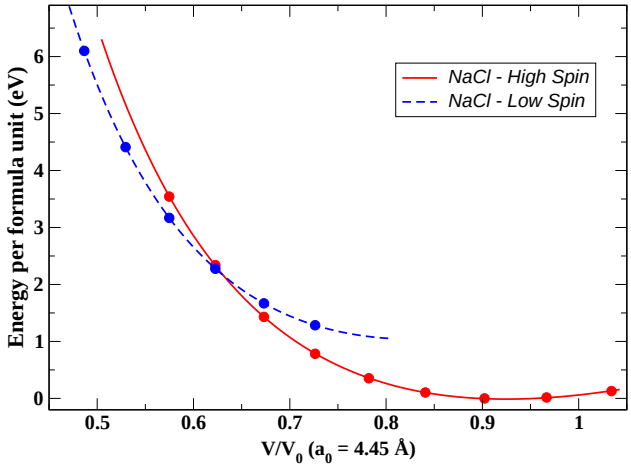

Figure 4.5. The calculated total energy/MnO versus volumes for the AFMII rocksalt phase, referred to zero at their equilibrium volume. The filled symbols denote the energies of the large volume, high spin configuration and the open symbols denote the energies of the small volume, low spin configuration. The continuous and dashed lines are the least square fitted curves to the Murnaghan equation of state for high and low spin configurations respectively.

	v_0	v_h	v_l	Δv	B_h	B_l	B'_h	B'_l	P_c
GGA	1.02	0.70	0.62	0.08	196	-	3.9	-	149
LDA+U	0.93	0.66	0.61	0.05	192	195	3.2	3.6	123

Table 4.1. Quantities obtained from fits to the Murnaghan equation of state for the LDA+U functional and compared to the GGA column, which are taken from Ref. [64]. v_0 is the experimental equilibrium volume, B and B' are the bulk modulus (in GPa) and its pressure derivative. v_h, v_l are the calculated volumes of the high and low pressure phases, respectively, at the critical pressure P_c (in GPa). Δv is the amount of volume collapse that occurs at the transition pressure P_c. All volumes are referred to the experimental equilibrium volume. The experimental values are B=142-160 GPa, $B' \approx 4$; see Zhang[63] and references therein.

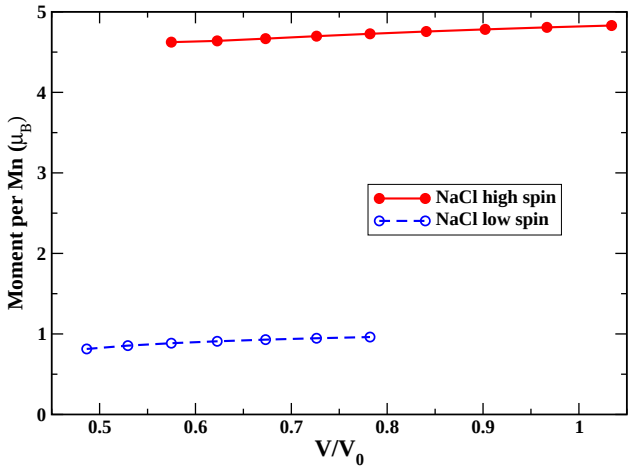

Figure 4.6. Calculated moment on each Mn site as a function of volume. We observe a distinct collapse (first order) of magnetic moment with decrease in volume. At large volumes, the high spin state with S = 5/2 (single occupancy of the d-orbitals) is realized whilst the low spin state with S = 1/2 is favored for smaller volumes.

Magnetic Moment

The moment collapse behavior as a function of pressure is collected in Fig. 4.6. We predict a distinct collapse (first order) of the magnetic moment with decrease in volume. For comparison, the GGA result presented by Cohen *et al.*[64] was a moment collapse from $3.4\mu_B$ to $1.3\mu_B$ at the volume given in Table 4.1. At low pressure, we get the high-spin S=$\frac{5}{2}$ configuration of the Mn^{2+} ion, with the local moment being reduced slightly from $5\mu_B$ by $3d-2p$ mixing. This electronic phase persists over a substantial volume reduction, becoming unstable around $v = 0.60$ and rearranging to a low-spin state S=$\frac{1}{2}$, *not* the nonmagnetic $S = 0$ result that might naively be anticipated.

Fundamental Band Gap

In Fig. 4.7 the calculated band gap of both high-spin and low-spin states are shown. At ambient pressure the LDA+U method gives a gap of less than 2 eV. Experi-

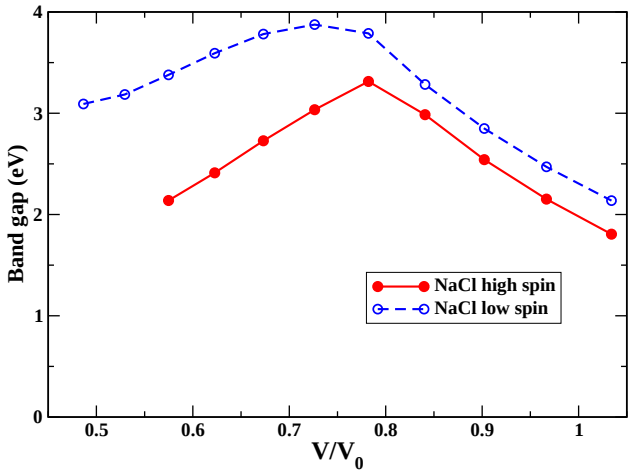

Figure 4.7. Calculated band gap as a function of volume. For LDA+U, the band gap increases with decrease in volume for the high spin state, but decreases with volume in the low spin state. At very low volumes, were the low spin configuration is preferred LDA+U gives a substantial gap and is still an insulator

mental values lie in the 3.8-4.2 eV range. Referring to Fig.4.3 , it can be observed that the large volume gap depends on the position of the majority $3d$ states with respect to the free-electron-like band, *i.e.* it is not the $3d-3d$ Mott gap. The LDA+U gaps, smaller initially, show a much stronger increase with pressure, and also incur the band crossover that leads to decrease of the gap (within the high-spin state). This gives the transition a distinctive character: the low-spin state has a larger gap than the high-spin state, and there does not seem to be a metallic state nearby.

Analysis of the Transition

In this section we analyze the character of the states just above and just below the Mott transition. The projected DOSs (PDOSs) in Fig. 4.8 refer to projections onto Mn $3d$ orbitals, with the z-axis being the rhombohedral axis, the a_g $3z^2-r^2$ ($|m|$=0) state; the e_g' pair $\{xz, yz\}$ ($|m|$=1); and the e_g pair $\{x^2-y^2, xy\}$ ($|m|$=2). Because the

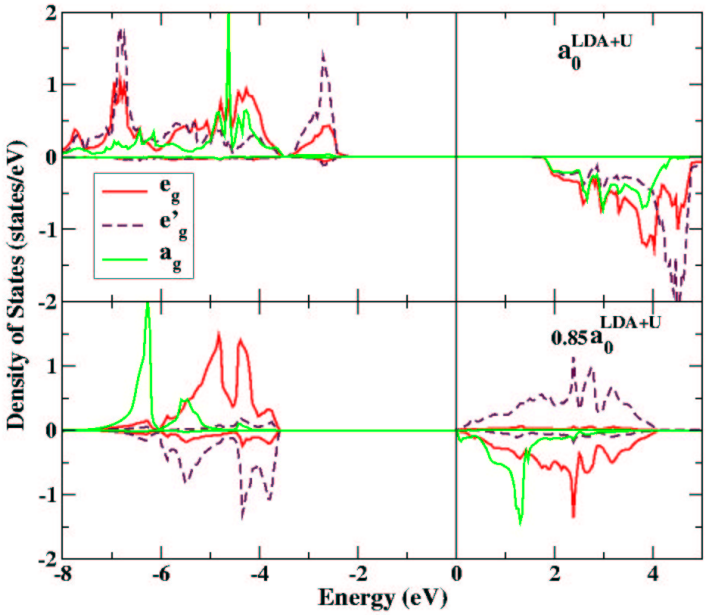

Figure 4.8. Projected DOS onto symmetrized Mn $3d$ orbitals in the rhombohedral AFMII rocksalt phase using the LDA+U method. Top panel: High spin solution at the LDA+U equilibrium volume. Bottom panel: Low spin solution at 60% of the LDA+U equilibrium volume. The a_g orbital is the $3z^2 - r^2$ oriented along the rhombohedral axis, other symmetries are described in the text. The overriding feature is the spin-reversal of the $m = \pm 1$ e'_g orbitals between the two volumes.

two e_g representations have the same symmetry, they can mix and the actual combinations $e_{g,1}, e_{g,2}$ are orthogonal linear combinations of e_g, e'_g which depend on interactions. For the LDA+U results, however, there is little mixing of the e_g, e'_g pairs. The character of the transition is simple to describe: the e'_g pair ($|m|$=1 with respect to the rhombohedral axis) simply flips its spin.

This S=$\frac{1}{2}$ state is unexpected and quite unusual. First, each $3d$ orbital is still singly occupied, verified by plotting the charge density on the Mn ion and finding it just as spherical as for the high-spin state. Second, each $3d$ orbital is essentially fully spin-polarized, with the configuration being $a_g \uparrow e_g \uparrow e'_g \downarrow$. A plot of the spin density (Fig. 4.9)

reveals the unanticipated strong anisotropy with nodal character, characteristic of spin-up $m = 0$ and $|m|$=2 orbitals, and spin-down $|m|$=1 orbitals (in the rhombohedral frame). Third, it makes this transition with essentially zero change in the gap, which is 3.5 eV. The band structure changes completely, however, so the close similarity of the gaps on either side is accidental.

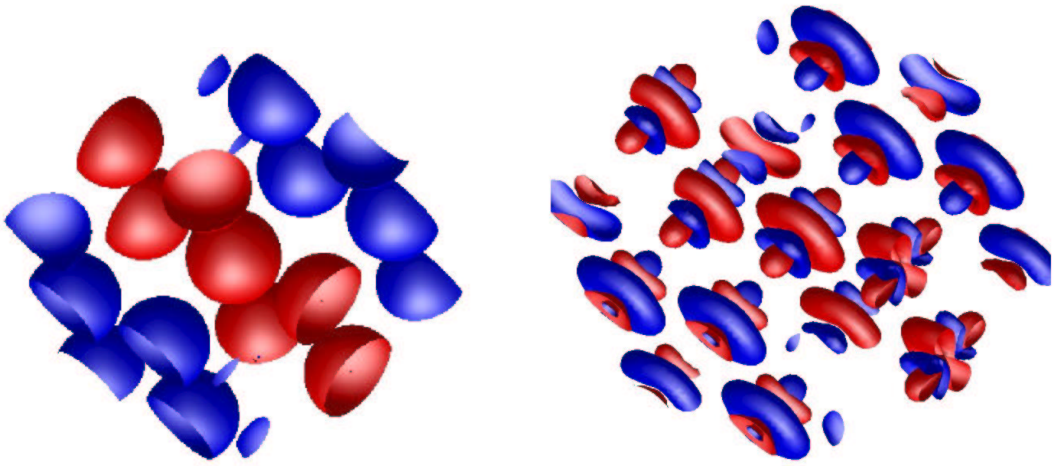

Figure 4.9. Spin density plot of the AFMII MnO in the LDA+U method. (red = majority spin channel, blue = minority spin channel) *Left*: High spin solution, wherein all the 5 spins are parallel to each other in each layer and antiparallel along the [111] axis. So, we see a layer of up-spins (all red) surrounded by a layer of down-spins (all blue) above and below. *Right*: Visible difference in the spin arrangement due to the un-anticipated strong anisotropy. The a_g orbital is still fully polarized (red - axial) and pointing along the [111] axis of the rhombohedron. The two doublets, e_g (red - inplane) and e_g' (blue) are also fully polarized with equal and opposite spins as seen in the plot

Now, I will move on to the high pressure NiAs (B8) phase witnessed in experiments.

4.5.2 NiAs (B8) MnO:

Fig.4.10 shows the arrangement of Mn and O atoms in the NiAs (B8) phase. The B8 structure can be generated from a *hcp* arrangemet of oxygens and then filling the octahedral holes with Mn ions. In contrast the rocksalt (B1) structure has a fcc close packing of ions with all of the octahedral holes filled. In the B1 structure, both Mn and O sites are octahedrally coordinated while in the B8 structure, the Mn atoms are octahedrally coordinated by the 6 surrounding O sites, but the O sites are surrounded by a trigonal prism of 6 Mn ions. The local environment around the Mn ions is still octahedral like in the B8 structure.

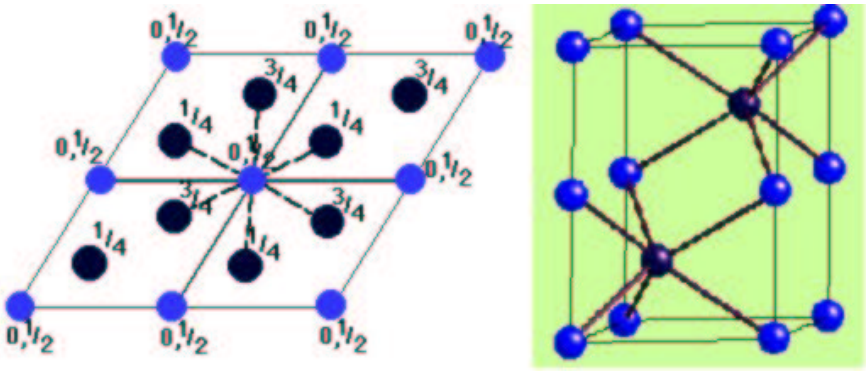

Figure 4.10. The NiAs phase of MnO. The blue spheres are the Mn ions, and the purple spheres represent the O ions. The left panel shows the top view of 4 formula unit cells, wherein the octahedral coordination of the Mn ions with the 6 neighboring O sites is depicted. On the right panel, a frontal view of one formula unit cell is shown, elucidating the trigonal prismatic coordination of the oxygens.

All the experiments have only ascertained the structural arrangement of the high pressure phase (NiAs), but have not obtained information about the possible magnetic ordering of the Mn ions in the NiAs phase. There are two possibile arrangements of the Mn spins in the NiAs phase, ferromagnetic or antiferromagnetic. We have done total

energy calculations for both the orderings for a wide range of pressures and the findings are displayed in Fig.4.11. Our LDA+U calculations show the antiferromagnetic (AFM) phase to be energetically favorable than the ferromagnetic (FM) phase, by 0.2 eV for a wide range of pressures. Fang and coworkers [65] have previously reported GGA and LDA+U calculations for the NiAs phase of MnO and concluded that the FM ordering is favourable, which is contrary to our findings. This could be due to the fact that, they did not do a c/a optimization for the B8 phase. We have optimized the c/a ratio for a wide range of volumes and found it to undergo substantial changes.

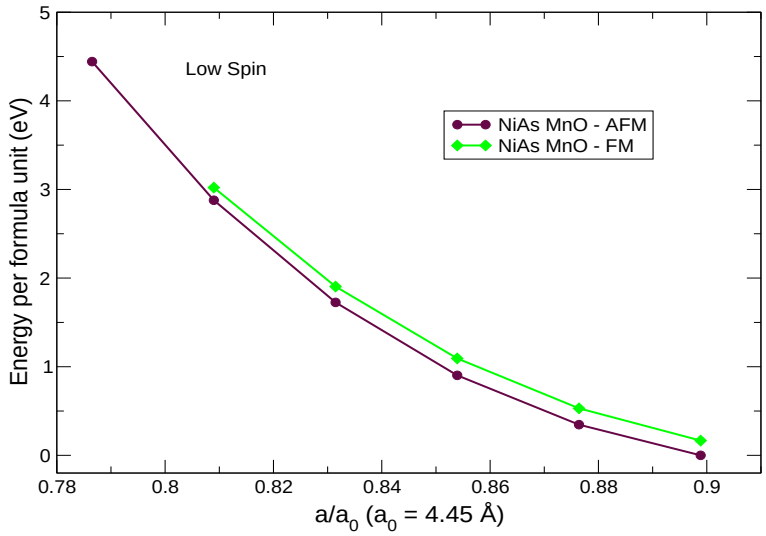

Figure 4.11. Calculated total energy versus volume for both FM and AFM ordering of the Mn ions in the high pressure NiAs structure. All the energies were obtained after a c/a optimization within their respective magnetic ordering. Throughout the phase-space considered here, the AFM is lower than the FM by about 0.2 eV. Thus, we only do further analysis of the AFM NiAs-MnO structure.

Displayed in Fig.4.12 and 4.13 are the results of our c/a optimization for the AFM ordering in the B8 phase. Since LDA+U gives two solutions, a high spin (S = $5\mu_B$) and a low spin (S = $1\mu_B$), we performed calculations for both such solutions. We notice,

the c/a values show a substantial increase with pressure and the trend is the same for both possible spin solutions. These ratios do change for different magnetic orderings. Keeping that in mind, we also did optimizations for the FM ordering and noticed the same trend. All these calculations were done within the LDA+U methodology with U = 5.5 eV and J = 1 eV, to retain consistency with the rocksalt phase results. Using our findings as a benchmark, I will now concentrate on AFM NiAs MnO as the high pressure phase and analyse the electronic structure.

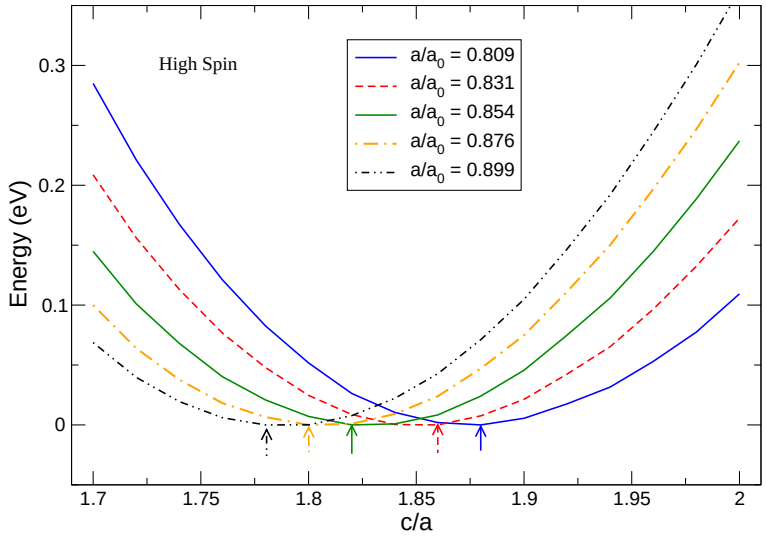

Figure 4.12. Calculated total energies versus c/a for different volumes of NiAs MnO in the high spin state. The arrows indicate the optimized c/a value for the corresponding lattice constant. With pressure, the c/a ratio increases.

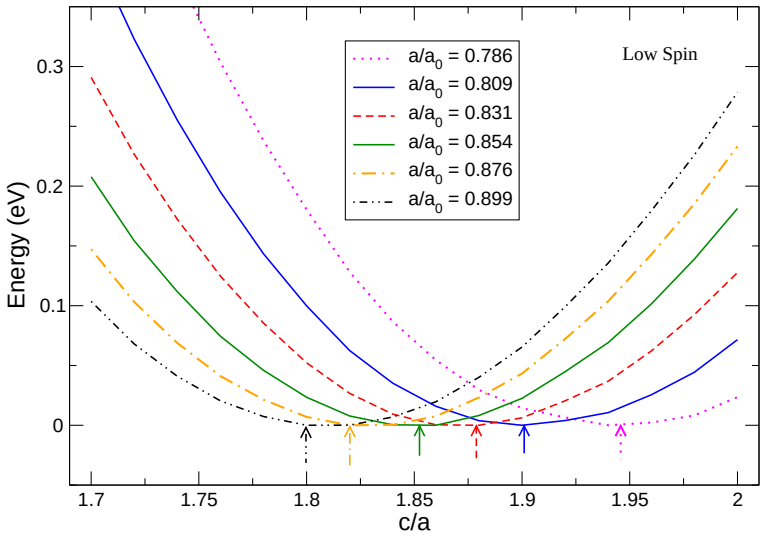

Figure 4.13. Calculates total energies versus c/a for different volumes of NiAs MnO in the low spin state. The arrows indicate the optimized c/a value for the corresponding lattice constant. With pressure, the c/a ratio increases.

The equation of state (EOS) energy vs. volume curves for both the AFMII NaCl and AFM NiAs-MnO structure are collected in Fig.4.14. There are two electronic phases within each structure, a high-spin (S = 5/2) and a low-spin (S = 1/2) phase. From the enthalpies of all the four curves, we notice that the previously mentioned first order magnetic transition and volume collapse within the NaCl phase still prevails at 123 GPa but is quickly followed by a transition to a low spin NiAs phase at 130 GPa, without much change in the volume. (Note: The LDA+U results are very much dependent on the choice of U and J. The numbers reported here are only true for U = 5.5 eV and J = 1 eV. One can get different transitions and pressures for other choices)

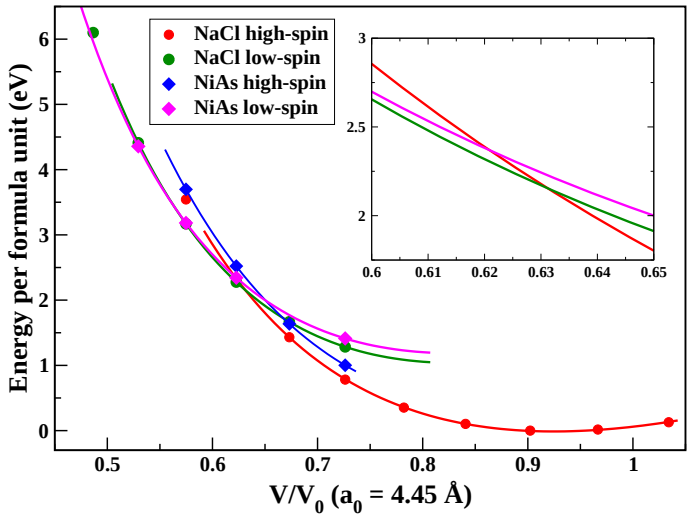

Figure 4.14. The calculated total energy/MnO versus volumes for the low pressure and high pressure structures of MnO. The filled symbols denote the calculated energies and the continous lines are the least square fitted curves to the Murnaghan equation of state for high and low spin configurations respectively.

Changes in the Mn-moment and band gap for both the structures as a function of pressure are collected in Fig.4.15 and 4.16. As shown previously for the rocksalt phase, LDA+U gives two distinct spin states for the NiAs phase also. At low pressure we obtain the S = $\frac{5}{2}$ high-spin configuration while at high pressures the S = $\frac{1}{2}$ is realized. An interesting fact to notice here is that, even the high pressure AFM NiAs phase also stabilizes in the S = $\frac{1}{2}$ spin configuration and not in the nonmagnetic S = 0 state. Discussions in the previous sections have indicated that the NaCl low spin phase continues to be an insulator upto very high pressures, with a substantial gap. The results of the NiAs low spin phase also follows the same trend, with the S = $\frac{1}{2}$ state having a larger gap than the S = $\frac{5}{2}$ state. So, LDA+U predicts a NaCl-MnO (insulator, high-spin) $\longrightarrow$ NaCl-MnO (insulator, low-spin) transition at 123 GPa $\longrightarrow$ AFM NiAs-MnO (insulator, low-spin) transition at 130 GPa.

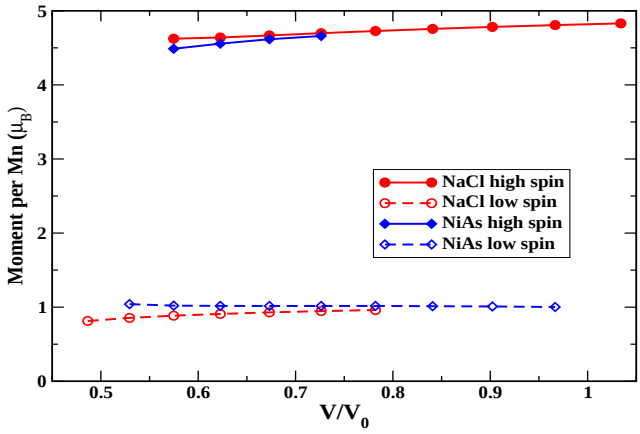

Figure 4.15. Changes in moment on the Mn site as a function of pressure for both NaCl and NiAs structures of MnO.

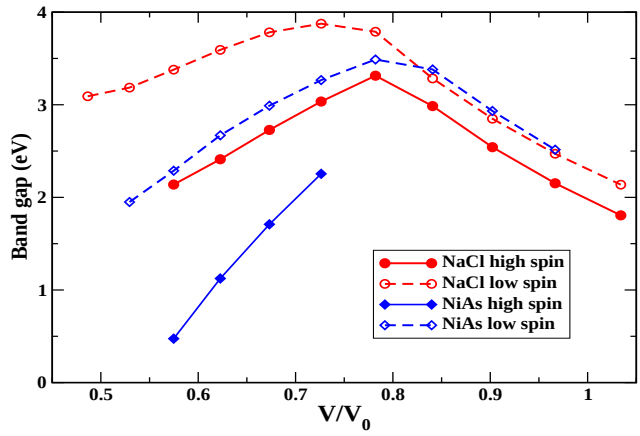

Figure 4.16. Band gap versus volume for NaCl and NiAs-MnO. LDA+U predicts an insulator for a wide range of pressures.

Analysis of the transition

Our findings of an insulator → insulator transition is contrary to the recent experiments which witness a Mott transition in the NiAs structure. The AFM ordering of the Mn moments in the NiAs structure along with the LDA+U methodology used for

the total energy calculations seems to aide in the persistence of an insulating gap upto very high pressures. Now, I will analyze the character of the Mn d states in the NiAs structure and compare it with the previously analyzed NaCl structure. The projected DOSs for both high-spin and low-spin states and for both structures are displayed in Fig.4.17. The physics of the $S = \frac{5}{2} \rightarrow S = \frac{1}{2}$ transition for the NiAs structure is strikingly similar to that of the NaCl structure. The so called 'spin-flip' solution is also realized in the NiAs structure. Going from NaCl to NiAs, the structure changes from rhombohedral to hexagonal, but the underlying local symmetries do not change much and the d orbitals are still seperated into two doubly degenerate doublets and a singlet. The singlet a_g is pointing along the hexagonal axis. So, the low-spin state is obtained by just 'flipping' the e'_g pair with respect to the hexagonal axis. This novel spin transition produced by LDA+U prevails for both the structures.

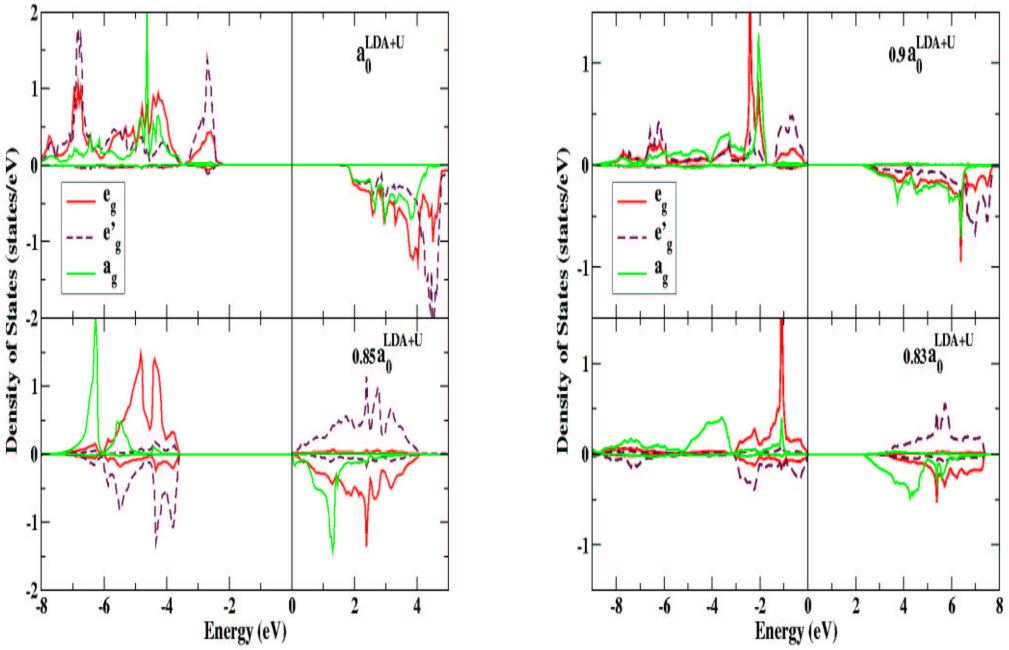

Figure 4.17. *Left*: Projected DOS onto symmetrized Mn 3*d* orbitals in the NaCl AFMII phase using the LDA+U method. Top panel shows the solution at the LDA+U equilibrium volume, while the bottom panel shows the low-spin solution at 60% of the LDA+U equilibrium volume. The a_g orbital is oriented along the rhombohedral axis. *Right*: Projected DOS onto symmetrized Mn 3*d* orbitals in the NiAs AFM phase using the LDA+U method. Top panel shows the high spin solution, while the bottom panel shows the low-spin solution at 54% of the equilibrium volume. The overriding feature is the spin-reversal of the $m = \pm 1 e'_g$ orbitals between the two volumes for both the structures.

4.6 Trends due to U and J

In this section, I will present a systematic look at the energetics for various choices of the 'Hubbard U' and the 'Exchange constant J'. I will concentrate only on the rocksalt phase of MnO, since the trends are quite similar for the NiAs phase.

In Figs.4.18 and 4.19, I have collected the total energies versus normalized lattice

constant for two choices of U = 4.5 eV and 5.5 eV, with J going from 0.0 eV to 1 eV. First, let us look at a fixed value of J (say 1 eV) and observe what happens when we change U from 4.5 eV to 5.5 eV. The energy difference between the minima's of the high and low spin insulating states increases. This results in an increase in slope of the common tangent that connects both the curves, thereby leading to an increase in the calculated transition pressure, with increase in U. Now, let us keep U constant (say 5.5 eV) and change J from 1 eV to 0 eV. From Fig.4.19 we observe that, the low spin energy curve is again shifted upwards with respect to the high spin energy curve, leading to an increase in transition pressure. Though, the trends look similar for changes in U and J, the curvature of the trends are not the same. *i.e.* critical pressure P_c increases with increase in U, while decreases with increase in the value of J, with the possibility of no transition for $J \rightarrow 0$.

Along with the two insulating solutions, we were also able to obtain a metallic low spin state, but that was always energetically unfavorable for all choices of parameters. For the sake of completeness, their energetics are also presented in Figs.4.18 and 4.19.

The various transition pressures due to our choices of U and J are collected in Fig.4.20.

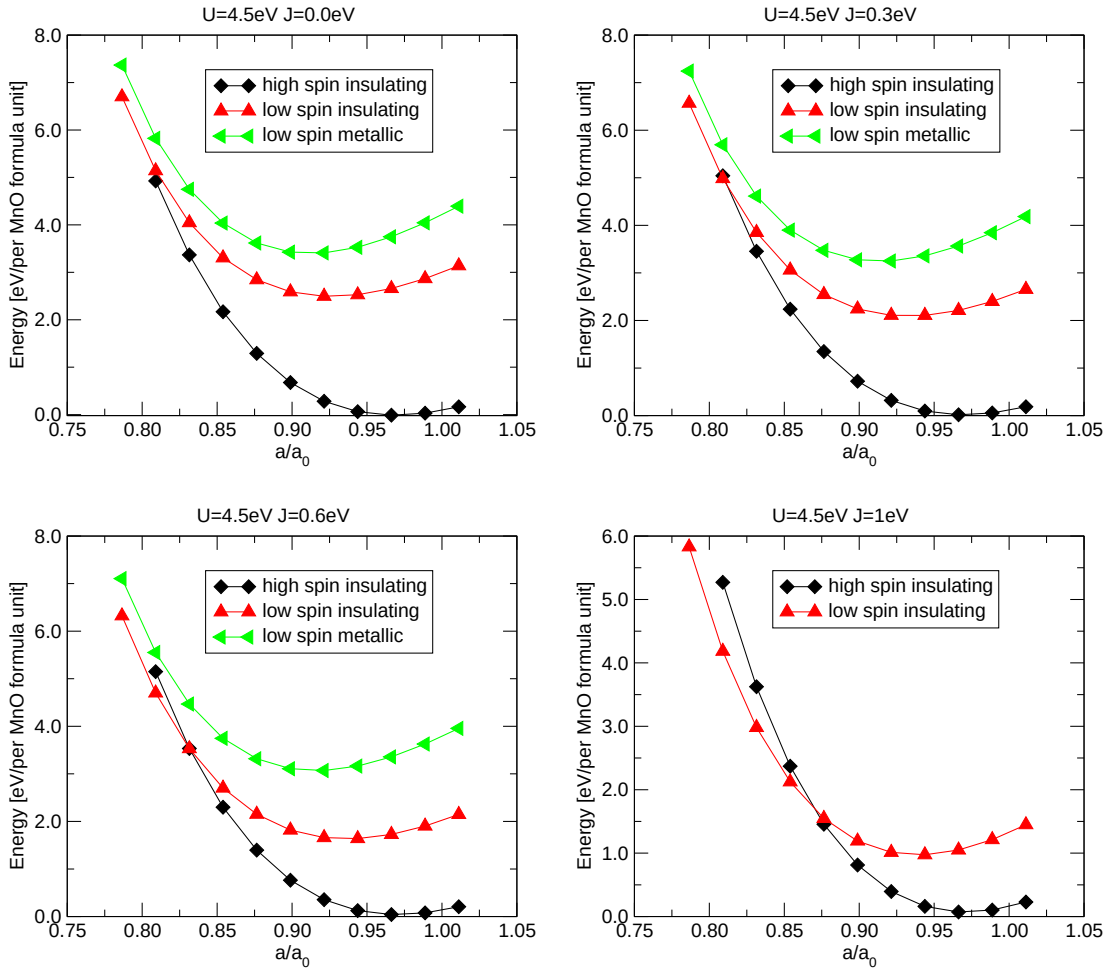

Figure 4.18. Calculated LDA+U total energies versus normalized lattice parameter for rocksalt phase of MnO with U = 4.5 eV and J = 0, 0.3, 0.6 and 1 eV. The filled symbols denote the actual energies, while the continous lines are there as a guide to the eye.

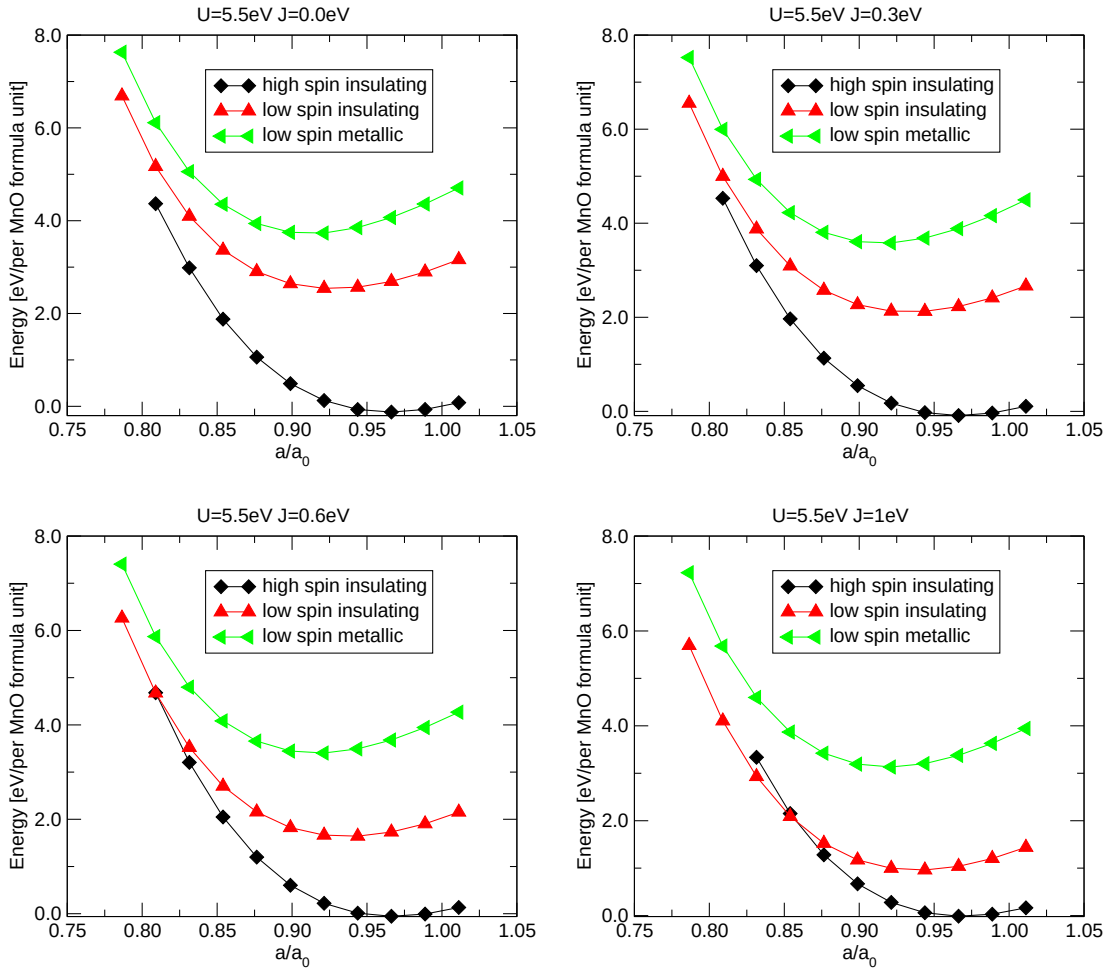

Figure 4.19. Calculated LDA+U total energies versus normalized lattice parameter for rocksalt phase of MnO with U = 5.5 eV and J = 0, 0.3, 0.6 and 1 eV. Notice the change in the energy axis of this plot as compared to the previous plot with U = 4.5 eV.

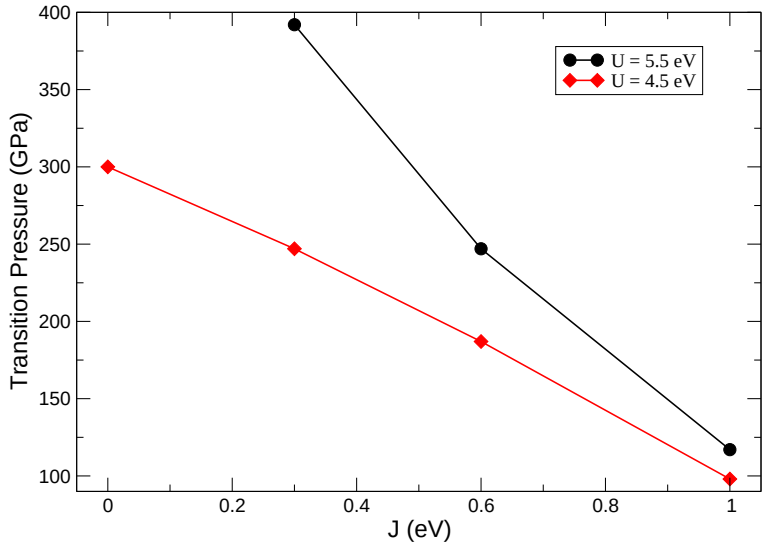

Figure 4.20. Calculated transition pressure P_c, from high-spin insulating rocksalt MnO to the low-spin insulating rocksalt MnO, for the various choices of U and J. These numbers were obtained from doing a least square fit to the Murnaghan equation of state and equating the resultant enthalpies for the various solutions.

4.7 Effect of the exchange constant J

Depending on the value of the exchange constant J, we are able to calculate multiple magnetic solutions within the LSDA+U method. As discussed in the previous section, when using J = 1 eV, we obtain the possibility of a phase trasition from a S = 5/2 B1 phase to S = 1/2 B1 phase around 123 GPa, followed by a transition to S = 1/2 B8 phase at 130 GPa. On the contrary if we choose J = 0 eV, we do not obtain the possibility of any phase transition. In order to understand the unique effect of J, we will start from the simple cubic (rocksalt) structure in the LDA approximation. We will focus on the low spin state, since the major effects of J are witnessed in that regime.

4.7.1 Cubic Ferromagnet - LSDA

The cubic (fcc) MnO cell contains one Mn site. The LDA total and the orbital projected DOS of the ferromagnetic (FM) solution at the compressed volume $V/V_0 \approx 0.64$ is shown in Figure 4.21. The cubic symmetry splits the Mn d orbitals into a triplet t_{2g} and a doublet e_g. From the Mn d orbital projected DOS we see that the e_g bands are more involved in the covalent bonding with the O p orbitals producing a covalency split of 10 eV. The t_{2g} and e_g states are split due to the crystal field effect.

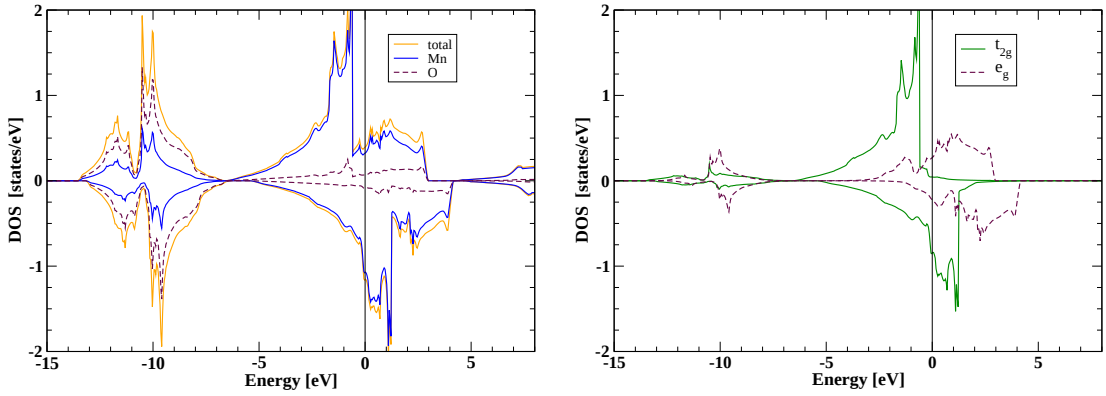

Figure 4.21. *Left*: Total DOS of fcc MnO (spin polarized) in the LDA approximation at 64% of the equilibrium volume ($a_0 = 4.45$ $\mathring{A}$. *Right*: Orbitally resolved DOS of the Mn d orbital. Cubic symmetry splits the d orbitals into a triplet t_{2g} (green/continous) and a doublet e_g (brown/dashed)

The Mn atoms along the cubic axis can interact via the Oxygens. These involve mainly the e_g orbitals with the O p orbitals. This covalency pins the position of the e_g bands relative to the Oxygen bands. And there is no direct Mn-Mn next nearest neighbor (NNN) coupling due to symmetry constraints. This leads to the fact that the t_{2g} bands are more flexible and hence more active when the symmetry is changed and/or LSDA+U is applied. Presently, the e_g bands are basically unoccupied and the 5 d electrons are

distributed in the t_{2g} orbitals thereby leading to a metallic solution.

Now, let us apply a U to this system. Here we fix U = 5.5 eV and J = 0 eV.

4.7.2 Cubic Ferromagnet - LSDA+U

Figure 4.22 shows the result of applying LSDA+U on the Mn d states. The main effect of U is to shift the occupied bands down and the unoccupied bands up. The e_g bands are basically unoccupied, which results in an up-shift of both e_g spin sub bands. This additional up-shift removes the e_g bands completely from the discussion of the occupation effects and energetics. But the covalent split of about 10 eV is still maintained by the e_g states. The t_{2g} spin sub bands are shifted according to the expected U-effect. There is no possibility for a gap in the spin down band since the cubic symmetry does not allow a gap opening with in the t_{2g} band and the electron count requires the minority band to contain two electrons, resulting in a spin $\frac{1}{2}$ half-metal.

However, one can release the cubic symmetry by creating a rhombohedral cell, still maintaining the ferromagnetic alignment of the spins, (*i.e.* fcc unit cell with lower number of symmetry operations). This rhombohedral symmetry then splits the 5 d orbitals into two doublets and a singlet which we shall refer to e_{g1}, e_{g2} and a_g respectively. Now applying U (J = 0 eV) to this lower symmetry structure will lead to a gap formation in the system, which we discuss below.

4.7.3 Rhombohedral Ferromagnet - LSDA+U

Figure 4.23 shows the orbital projected DOS for the rhombohedral (low symmetry fcc) MnO, within the LSDA+U approximation. The rhombohedral cell that we use

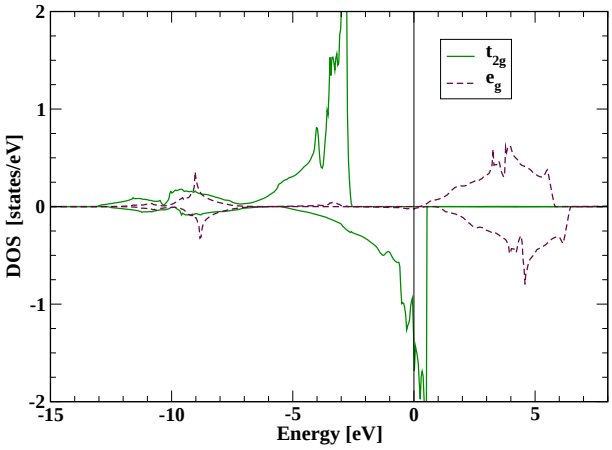

Figure 4.22. Mn d orbital projected DOS for the fcc MnO (spin polarized) in the LSDA + U (5.5 eV) approximation. The dashed (brown) curve is the e_g state, completely unoccupied and separated from the Oxygen states by a covalent split of about 10 eV. The $5d$ electrons are distributed among the t_{2g} levels producing a spin $\frac{1}{2}$ half-metal.

for this calculation is obtained by rotating the coordinate system and interpreting the primitive cell of the fcc lattice as a rhombohedral cell, with only D_{3d} symmetry. So, we still have only one formula unit of MnO in the unit cell. For clarity we show the DOS in both the rhombohedral and the cubic coordinate system. We observe the effect of the symmetry lowering, which has aided in the creation of a band gap.

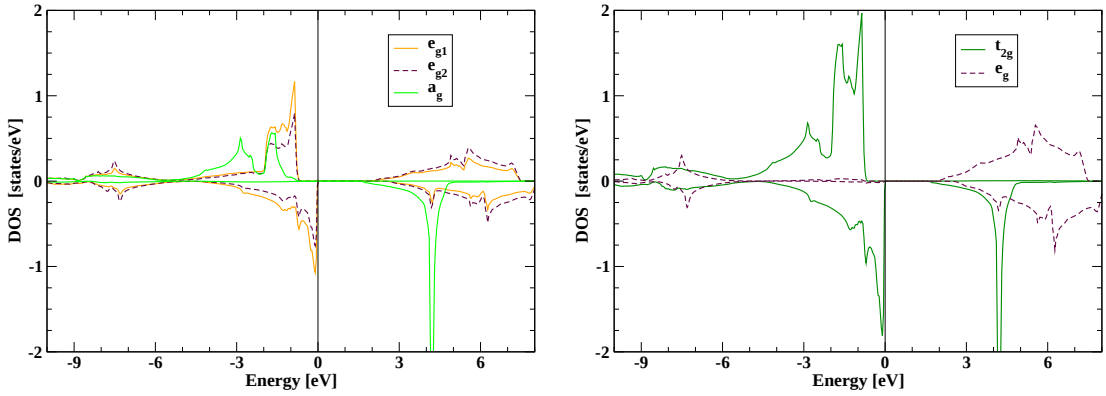

Figure 4.23. *Left*: Mn d orbital projected DOS for the low symmetry fcc (rhombohedral) cell for LSDA+U method. The orbitals are projected along the rhombohedral axes. The a_g orbital is the $3z^2 - r^2$ oriented along the body diagonal of a cube. *Right*: Cubic decomposition of the orbitals depicted in the top panel.

From the cubic decomposition we can clearly see the split happening in the minority t_{2g} band. The former e_g bands continue to remain unoccupied and do not mix in, since they do not have the relevant energies.

The fact that the singlet a_g is split by U makes the resulting solution insulating. Within the rhombohedral symmetry, the 2 two-dimensional irreducible representations (e_{g1}&e_{g2}) are equivalent and hence are allowed to mix. Out of the 5 electrons, one is in the singlet a_g. The remaining 4 electrons seem to be equally distributed between the spin up/down channels of e_{g1} and e_{g2} thereby cancelling out and producing a net S = 1/2 insulator.

There is another possibility, however. The splitting could occur in the doublets, e_{g1} and/or e_{g2}. This means that the a_g is fully filled, thereby bringing e_{g1} and e_{g2} to the fermi level producing a metal. This solution 'does' exist, but is energetically higher

than the insulating one described above. For simplicity we will maintain our focus on the insulating solutions.

Now, we move to the next step. We maintain the rhombohedral (low symmetry fcc) symmetry, but introduce the AFMII ordering in the system. In this phase, <111> layers have spins aligned, and successive layers are antiparallel. In order to account for the two types of Mn sites in the system, the rhombohedral cell that we consider for this calculation has two formula units of MnO per unit cell. Just to reiterate, we still are fixing U = 5.5 eV and J = 0 eV.

4.7.4 Rhombohedral Antiferromagnet (AFMII) - LSDA+U

Since the large exchange split is responsible for the ferromagnetic calculation itself to be insulating, the superposition of the AFMII ordering does not change the energetics much. Since we are already in the gapped regime, the AFMII order does not create a new gap, but slightly enhances the gap (2.5 eV) created by the ferromagnet. The striking feature is that, the projected DOS depicted in Figure 4.24 for the rhombohedral AFMII ordering looks exactly like the rhombohedral FM Figure 4.23. The minority t_{2g} is split and the e_g states are still fixed above the fermi level by the covalency.

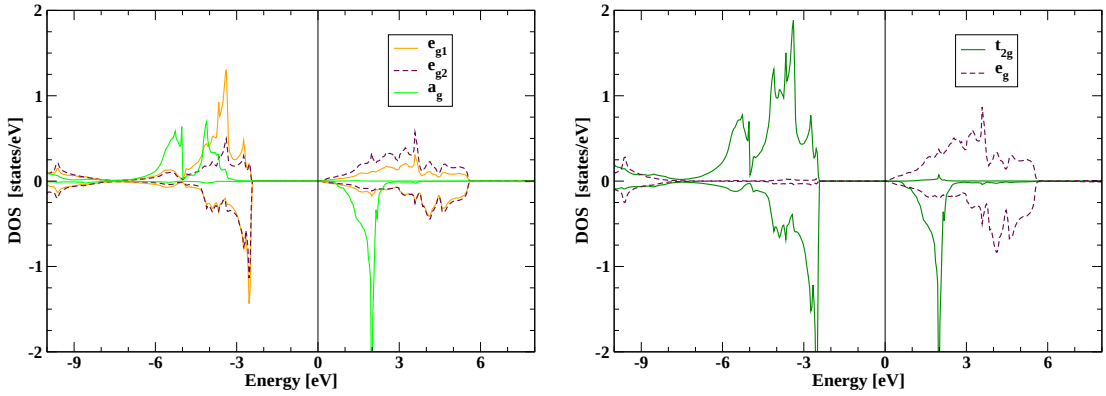

Figure 4.24. *Left*: Spin and symmetry projected DOS for the AFMII MnO using the LSDA+U method. The orbitals are projected along the rhombohedral axes. *Right*: Cubic decomposition of the Mn d orbitals from the top panel.

As mentioned in the previous section, it is possible to occupy the singlet a_g fully, thereby bringing the two doublets on to the fermi level creating a metallic solution which is again energetically unfavourable for the chosen parameters.

Next, we take the final step and turn on the J in our calculations. We now present the results of the rhombohedral AFMII cell with U = 5.5 eV and J = 1 eV.

4.7.5 Rhombohedral AFMII - LSDA+U & J = 1 eV

Figure 4.25 shows the DOS in both rhombohedral coordinate system and the corresponding cubic decomposition. Except for the inclusion of the exchange constant parameter J of 1 eV, all other parameters are indentical to the previous calculation. The first difference we observe between Figures 4.24 and 4.25 is the increase in the band gap by 1 eV and the occupied band width of the Mn d orbitals is smaller. The next striking feature is the nature of occupancy of the doublets e_{g1} and e_{g2}. The majority spin sub band of e_{g1} is fully filled and the minority spin sub band is completely empty and vice

versa for the other doublet e_{g2}. The net result still produces a S = 1/2 insulator. Each of the 3d orbital is still singly occupied, thereby still spin polarized with a configuration of $a_g \uparrow e_{g1} \uparrow e_{g2} \downarrow$. Comparing to the S = 5/2 solution where each of the 3d orbitals are also singly occupied with a configuration of $a_g \uparrow e_{g1} \uparrow e_{g2} \uparrow$, the S = 1/2 state is obtained when the e_{g2} orbital just simply flips its spin. This "spin flip" result due to J = 1 eV is quite unusual. One could have anticipated the possibility of the same S = 1/2 state in which either one of the two doublets are fully filled with 4 electrons and the other doublet is completely empty. Such a state was not obtainable.

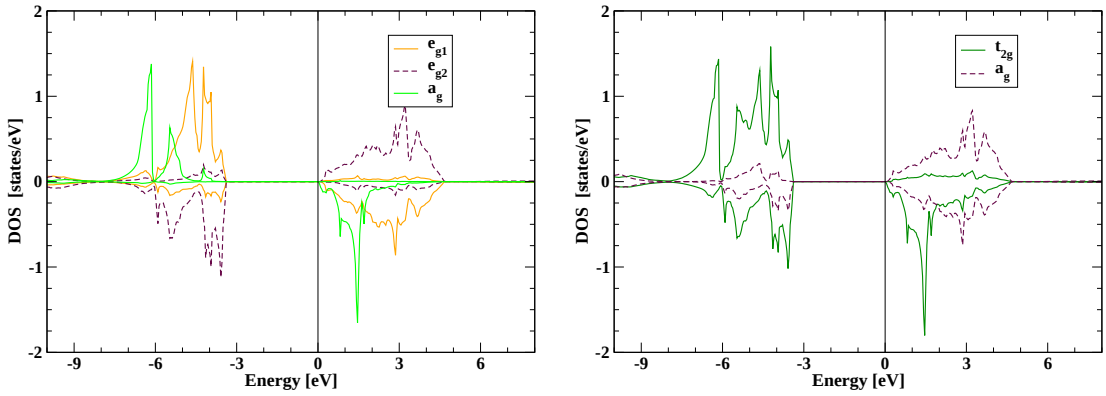

Figure 4.25. Spin and orbital projected DOS for the AFMII MnO in the LSDA+U method. Here we use J = 1 eV. *Left*: Orbitals projected along the rhombohedral axes. *Right*: Cubic decomposition

Comparing just the cubic decomposition of the DOS in Figure 4.24 and 4.25, we do not notice too many differences. But, one feature needs to be pointed out here. The e_g orbital is still fixed above the fermi level by a covalent split of 10 eV. But, when using J = 1 eV, we notice a small mixing of the e_g states with the t_{2g} in -6 to -3.5 eV region which is not seen in any of the previous DOS. The cubic decomposition is obtained by mere redistribution of the rhombohedral DOS along the cubic axis. Such a transformation neglects the off-diagonal contribution. If one includes the off-diagonal contribution also

into this picture, it is quite possible that the small e_g mixing that we notice here may not be as small anymore ! This could may be provide the insight into the effect of J in our calculations.

This unexpected difference between the solutions obtained from using J = 0 or 1 eV is also observed in the spin density plots (Figure 4.26), wherein we have plotted the spin density on a real space grid.

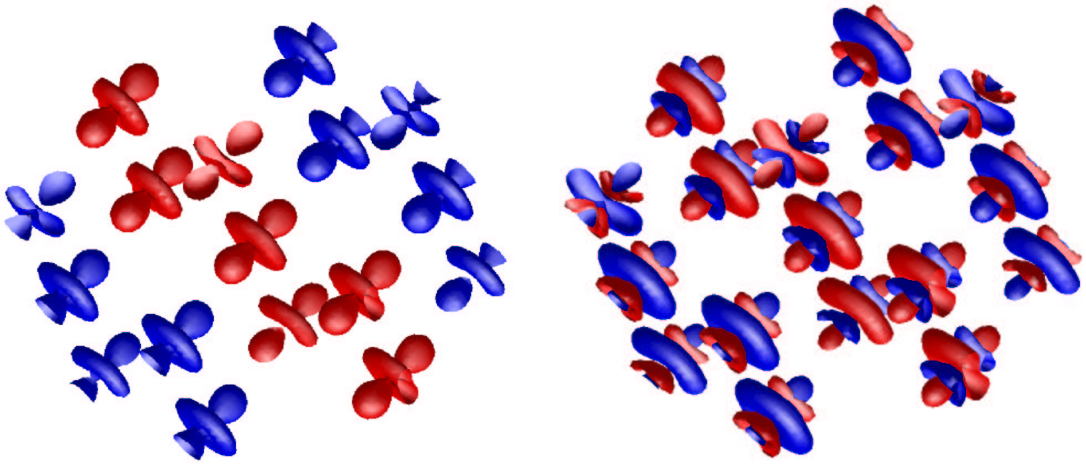

Figure 4.26. Spin density plot of the AFMII MnO in the LSDA+U method (red = majority spin channel, blue = minority spin channel). Both the plots depict the same S = 1/2 insulating solution. The left panel is from the calculation with J = 0 eV and the right panel is from the calculation with J = 1 eV. In the left panel, we can see the a_g orbital character only, corresponding to Figure 4.24, wherein they are completely spin polarized, while the other two doublets are not. All the red a_g orbitals (majority spins) depict the <111> layer with spins aligned and the adjacent layers are antialined with only minority spins (blue). In the bottom panel, we see a visible difference from the unanticipated strong anisotropy, corresponding to Figure 4.25. The a_g singlet is still fully polarized and looks identical to the top panel. But, the two doublets e_{g1} and e_{g2} are also fully polarized with equal but opposite spins as seen by the blue and red surfaces of the plot.

A compilation of the most relevant energetics for just the B1 phase from ambient pressure to high pressure are shown in Figure 4.27, for both choices of J = 0 and 1 eV. As mentioned earlier, we see no possible phase transition for the choice of J = 0 eV.

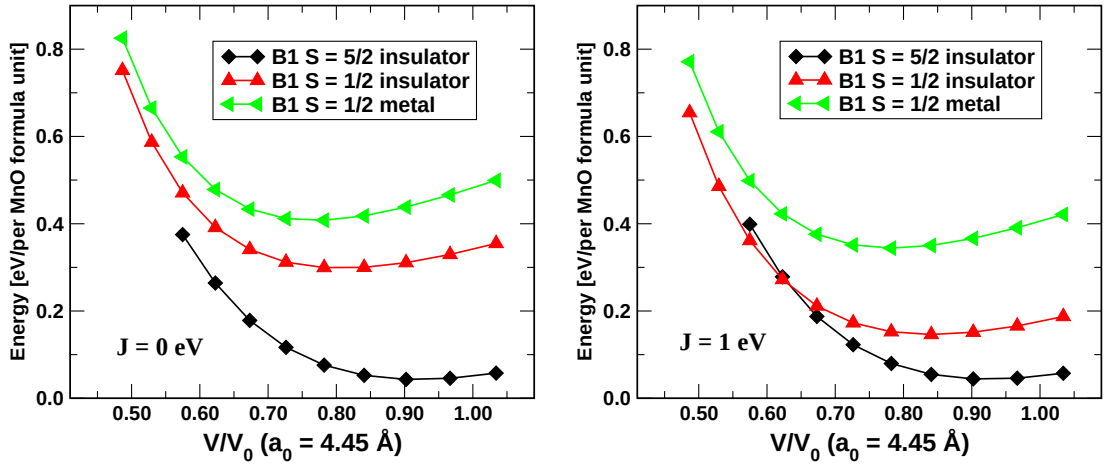

Figure 4.27. The calculated total energy/MnO versus volumes in the B1 phase for the LSDA+U method with different choices of J.

Having analyzed the B1 (NaCl) structure to understand the effects of J for a broad range of volumes, the next obvious question to ask is whether this behavior is witnessed in the B8 (NiAs) structure also. A detailed understanding of the crystal structure of the B8 phase would clearly reveal the fact that the underlying symmetries surrounding each Mn and O atoms are quite similar for both the B1 and B8 phases, which in turn leads to similar effects of J for both phases. Analysis of the DOS for a S = 1/2 insulating state of B8 MnO shows the "spin flip" solution similar to that of B1 phase when using U = 5.5 eV and J = 1 eV.

For the choice of J = 0 eV, we do not obtain either magnetic or structural phase transitions.

4.8 Conclusions

Our study provides some of the first detailed information on how magnetic moments in a real material may begin to disintegrate without vanishing identically, at or near a Mott transition, when correlation is taken into account. It is accepted that dynamic processes will be required for a truly realistic picture of the Mott (insulator-to-metal) transition. However, a moment collapse between two insulating phases may be described reasonably by a correlated band (static) approach.

Chapter 5

Lattice dynamics via Density-functional linear response

5.1 Framework

Response of electrons to a static external field is one of the important characteristics of a solid which can be uniquely determined within density functional theory. In recent years, the density-functional approach to the linear-response problem has proved to be powerful method for determining various solid-state properties. These include static dieletric properties in semiconductors and ionic crystals, screening response to electric fields and point charges, as well as lattice dynamical properties.

In this chapter, I will present a short overview of the algorithm of the perturbation theory, that takes into account the exchange effects and correlations in an inhomogeneous electron liquid by the density functional method. The results presented in the forthcoming chapters on lattice dynamics is solved using a code based on this formalism.

Within density-functional theory, the problem of calculating the lattice dynamics essentially amounts to finding the change in the electronic charge density in the presence of a phonon with wave vector $\mathbf{q}$. One of the most efficient technique developed for calculating this quantity is the solid-state analog[67, 68, 69] of the self-consistent Sternheimer[70] equation (which is the Schrodinger equation to linear order) for atomic polarizabilities. Its main features include, the study of the response via perturbation theory and the response to the total (bare+electronic) potential is obtained by iteration of the calculation up to self-consistency. The method is not restricted to perturbations written in terms of local potentials. This is of particular interest in lattice dynamics, where norm-conserving potentials are used to describe the electron-ion interaction. The calculations can be performed for perturbations of arbitrary wavelength, with use of only valence energy bands and wave functions of the unperturbed crystal.

The energy of a crystal is given by,

$$[-\nabla^2 + V(\mathbf{r})]\psi_i(\mathbf{r}) = E_i\psi_i \tag{5.1}$$

or

$$[-\nabla^2 + V_{bare}(\mathbf{r}) + e^2 \int \frac{\rho(\mathbf{r}')}{|\mathbf{r} - \mathbf{r}'|} dr' + V_{xc}(\rho(\mathbf{r}))]\psi_i(\mathbf{r}) = E_i\psi_i \tag{5.2}$$

where V is the sum of the external potential acting on the electons, plus an efffective electron-electron potential which depends on the density itself, plus the local-density approximation for the exchange and correlation. Now, when a perturbation $\Delta \mathrm{V}_{bare}$ is superimposed on the external potential, the whole self-consistent potential is modified accordingly: $\mathrm{V}_{SCF} \longrightarrow \mathrm{V}_{SCF} + \Delta \mathrm{V}_{SCF}$ (because, the perturbation also changes the wavefunction and the density).

Now let us consider the response of the atom when we apply an infinitesimal perturbing field $\delta \mathrm{V}_M(\mathbf{r})$. Each wave function $\psi_i(\mathbf{r})$ will be perturbed by this field. In the first order, the change is given by $\bar{\psi}_i(\mathbf{r})$ which is defined by

$$\psi_i(\mathbf{r}) \longrightarrow \psi_i(\mathbf{r}) + \bar{\psi}_i(\mathbf{r})\epsilon_M \tag{5.3}$$

Of course, this causes the density $\rho(\mathbf{r})$ to change, which in the first order is given by

$$\rho(\mathbf{r}) \longrightarrow \rho(\mathbf{r}) + \delta\rho(\mathbf{r})\epsilon_M \tag{5.4}$$

$$\delta\rho(\mathbf{r}) = 2Re(\sum_i \psi_i(\mathbf{r})^* \bar{\psi}_i(\mathbf{r})) \tag{5.5}$$

The change in the wavefunction and the density also changes the potential acting upon the electron. Along with the new external perturbation, the density changes cause a change in the potential $\mathrm{V}(\mathbf{r})$ in equation (5.1). So, the total self consistent potential is found by combining all these effects:

$$V^{new}(\mathbf{r}) = V_{bare}(\mathbf{r}) + e^2 \int \frac{\rho(\mathbf{r}')}{|\mathbf{r} - \mathbf{r}'|} dr' + V_{xc}(\rho(\mathbf{r}) + \delta V_{bare}(\mathbf{r}) + e^2 \int \frac{\delta\rho(\mathbf{r}')}{|\mathbf{r} - \mathbf{r}'|} dr' + \delta\rho(\mathbf{r})(\frac{\partial V_{xc}}{\partial \rho(\mathbf{r})}) \tag{5.6}$$

or

$$V^{new}(\mathbf{r}) = V(\mathbf{r}) + V_{SCF}(\mathbf{r})\epsilon_M \tag{5.7}$$

Using the first order perturbation theory on Schrödinger's equation, we can evaluate the change in the wave function, $\bar{\psi}_i(\mathbf{r})$. Since the energy changes will be of the order of ϵ_M^2 and negligible, we will have

$$[-\nabla^2 + V(\mathbf{r}) + V_{SCF}(\mathbf{r})\epsilon_M](\psi_i(\mathbf{r}) + \bar{\psi}_i(\mathbf{r})\epsilon_M) = E_i(\psi_i(\mathbf{r}) + \bar{\psi}_i(\mathbf{r})\epsilon_M) \tag{5.8}$$

$$\Downarrow$$

$$[-\nabla^2 + V(\mathbf{r}) - E_i]\bar{\psi}_i(\mathbf{r}) = -V_{SCF}(\mathbf{r})\psi_i(\mathbf{r}) \tag{5.9}$$

The above equation is the so called solid-state generalization of the Sternheimer equation. The original Sternheimer equation only used V_{bare} instead of V_{SCF}, the modified

self-consistent potential. First, one can do an atomic calculation to find the set of atomic wave functions $\psi_i(\mathbf{r})$, eigenvalues E_i and the potential $V(\mathbf{r})$. With these in hand, one can solve equations 5.3 to 5.9 self-consistently to find $\bar{\psi}_i(\mathbf{r})$ and $\delta\rho(\mathbf{r})$.

5.2 Choice of basis set

We have used an all-electron generalization of the linear-response approach, based on the above framework as implemented by Savrasov[71, 72, 73, 74]. In this approach, the first-order corrections are represented in terms of the muffin-tin (MT) basis sets which greatly facilitate the treatment of localized valence wave functions. The self-consistent solutions are obtained via the linear-muffin-tin-orbital (LMTO) method[76]. In this method, the space is partitioned into nonoverlapping (or slightly overlapping) muffin-tin spheres S_R surrounding every atom and the remaining interstitial region Ω_{int}. Within the spheres, the basis functions are represented in terms of numerical solutions of the radial Schrödinger equation for the spherical part of the potential multiplied by spherical harmonics as well as their energy derivatives taken at some set of energies ϵ_ν at the centers of interest. In the interstitial region, where the potential is essentially flat, the basis functions are spherical waves taken as the solutions of Helmholtz's equation: $(-\nabla^2 - \epsilon)f(r,\epsilon) = 0$, where the average kinetic energy $\epsilon = \kappa_\nu^2 = 0$ is chosen to fit the atomic-sphere approximation (ASA).

5.3 Calculation of the electron-phonon matrix element and the superconducting transition temperature

The electron-phonon interaction in metals plays an important role in a variety of experimentally accessible quantities, including the enhancement of the electron mass, the

phonon lifetime arising from electron-phonon scattering, electrical and thermal conductivities, and the superconducting transition temperature. The electron-phonon spectral function $\alpha^2F(\omega)$ measures the effectiveness of phonons with energy ω to scatter electrons from one part of the Fermi surface to another. Once it and the Coulomb pseudopotential μ^* are determined for a superconducting material, all of the thermodynamic properties of the superconductor, including the superconducting gap as a function of temperature, the transition temperature, and the discontinuity in the specific heat at T_c, can be computed [108]. In addition, transport properties of materials in the normal state can be calculated from the closely related spectral function $\alpha^2_{tr}F(\omega)$.

The superconducting transition temperature is evaluated via the Allen-Dynes[77] formula, the derivation of which is based on strong coupling theory. Here, I only highlight some of the important quatities that are needed to calculate T_c, the details of which can be obtained from reference [75]. The electron phonon matrix element describes the scattering of an electron at the Fermi surface from the state $|\mathbf{k}j\rangle$ to the state $|\mathbf{k}+\mathbf{q}j'\rangle$ via the phonon perturbation $\delta V^{\mathbf{q}\nu}_{eff}$:

$$g^{\mathbf{q}\nu}_{\mathbf{k}+\mathbf{q}j',\mathbf{k}j} = \langle \mathbf{k}+\mathbf{q}j'|\delta V^{\mathbf{q}\nu}_{eff}|\mathbf{k}j\rangle \tag{5.10}$$

where, $\mathbf{q}$ is the phonon wave vector, ν numerates the phonon branches, $\mathbf{k}$ lies in the first Brillouin zone and j is the band index. Band structure calculations done using the variational principle produces energy bands and wave functions that are not exact solutions of the one-electron Schrödinger equation. This leads to incomplete-basis -set (IBS) corrections in force calculations and this must be taken into account when calculating the electron-phonon matrix element. The above equation only holds good when $\psi_{\mathbf{k}j}$, $\psi_{\mathbf{k}+\mathbf{q}j}$ are exact solutions. The above expression is the linear-response analogy of evaluating the strength of the electron-phonon matrix element via the splitting of the bands in the frozen-phonon method.

The electron-phonon spectral distribution functions α^2F(ω) in terms of the phonon linewidths $\gamma_{\mathbf{q}\nu}$ is evaluated as:

$$\alpha^2 F(\omega) = \frac{1}{2\pi N(\epsilon_F)} \sum_{\mathbf{q}\nu} \frac{\gamma_{\mathbf{q}\nu}}{\omega_{\mathbf{q}\nu}} \delta(\omega - \omega_{\mathbf{q}\nu}) \tag{5.11}$$

where N(ϵ_F) is the electronic density of states per atom per spin at the Fermi level. When the energy bands at the Fermi level are linear in the range of phonon energies, the linewidth is given by Fermi "golden rule" and is written as follows:

$$\gamma_{\mathbf{q}\nu} = 2\pi\omega_{\mathbf{q}\nu} \sum_{\mathbf{k}jj'} |g^{\mathbf{q}\nu}_{\mathbf{k}+\mathbf{q}j',\mathbf{k}j}|^2 \delta(\epsilon_{\mathbf{k}j} - \epsilon_F)\delta(\epsilon_{\mathbf{k}+\mathbf{q}j'} - \epsilon_F) \tag{5.12}$$

The Allen-Dynes formula for the superconducting transition temperature T$_c$ is given as

$$T_c = \frac{\omega_{log}}{1.2} exp\left(-\frac{1.04(1+\lambda)}{\lambda - \mu^*(1+0.62\lambda)}\right) \tag{5.13}$$

where

$$\lambda = 2\int_0^\infty d\omega \frac{\alpha^2 F(\omega)}{\omega} \tag{5.14}$$

with

$$w_{log} = exp\langle ln\ \omega\rangle, \langle ln\ \omega\rangle = \frac{2}{\lambda}\int_0^\infty d\omega \frac{\alpha^2 F(\omega)}{\omega} ln\ \omega \tag{5.15}$$

where λ is the dimensionless electron-phonon coupling constant, ω_{log} is the logarithmic-averaged phonon frequency and μ^* is the effective screened Coulomb repulsion constant whose value is usually taken to be between 0.1 and 0.15. [78]

In the case of monatomic metals λ can also be expressed in the following form: [95]

$$\lambda = \frac{N(\epsilon_F)\langle I^2\rangle}{M\langle\omega^2\rangle} = \frac{\eta}{M\langle\omega^2\rangle} \tag{5.16}$$

where M is the mass of the atoms and $\langle\omega^2\rangle$ denotes the average of squared phonon frequencies (second moment of the frequency). The frequency moments are defined by

$$\langle\omega^n\rangle = \frac{2}{\lambda}\int d\omega \frac{\alpha^2 F(\omega)}{\omega}\omega^n \tag{5.17}$$

Further the quantity η which is called the Hopfield parameter is defined by $\eta = N(\epsilon_F)\langle I^2\rangle$ with $\langle I^2\rangle$ representing the Fermi surface average of the squared electron-phonon coupling interaction,

$$\langle I^2\rangle = \frac{\sum_{\mathbf{q}\nu}\sum_{\mathbf{k}jj'} \mid g^{\mathbf{q}\nu}_{\mathbf{k}+qj',\mathbf{k}j} \mid^2 \delta(\epsilon_{\mathbf{k}j}-\epsilon_F)\delta(\epsilon_{\mathbf{k}+qj'}-\epsilon_F)}{\sum_{\mathbf{q}\nu}\sum_{\mathbf{k}jj'}\delta(\epsilon_{\mathbf{k}j}-\epsilon_F)\delta(\epsilon_{\mathbf{k}+qj'}-\epsilon_F)} \tag{5.18}$$

Chapter 6

Superconductivity and Lattice Instability in Compressed Lithium

6.1 Introduction

Lithium is considered to be a 'simple' metal, because it is the lightest of the alkali metals and at ambient conditions, its properties are well described by a free electron model, since the motion of the conduction electrons is only weakly perturbed by interactions with the cubic lattice of atomic cores. Therefore metallic lithium has high conductivity, due to the delocalized valence electron (the two core electrons effectively shield the nucleus). Conventional BCS theory predicts the possibility of superconductivity in elements with low atomic numbers when compressed to a dense metallic phase [**?**]. In sharp contrast to the intutive expectation, that applying hyrostatic pressure normally favours high symmetric (high-coordination) crystal structures, Neaton and Ashcroft [88] using first principles band structure calculations predicted the possibility of Lithium preferring low-symmetry structures under pressure. Motivated by those predictions, Hanfland and coworkers [90] performed monochromatic synchroton X-ry powder diffraction studies of Li in a diamond

anvil cell (DAC) at pressures up to 50 GPa. They evidenced pronounced structural changes under pressure, with a fcc to $hR1$ phase around 39 GPa followed by a transition to $cI16$ (bcc unit cell with 16 atoms) phase at 42 GPa. The structural transitions are associated with a softening of the lattice caused by the pressure-induced electronic $s \longrightarrow p$ transition. This also suggests the possibility of superconducting properties of dense lithium near the phase transition regime.

The initial report of superconductivity in compressed Lithium was by Shimizu and coworkers [80], who observed a superconducting critical temperature (T_c) of 20 K at 48 GPa (onset at 30 GPa and above). This was quickly followed by magnetic susceptibility and electrical resistivity measurements by Struzhkin and coworkers [81], who observed T_c to range from 9 to 16 K at 23 to 80 GPa. The T_c of 16 K occured in the fcc phase around 37 GPa. Both these experiments had used non-hydrostatic pressure cells. Later, Deemyad and coworkers [79] used near-hydrostatic pressure conditions and witnessed a T_c of 14 K at 30 GPa (fcc phase).

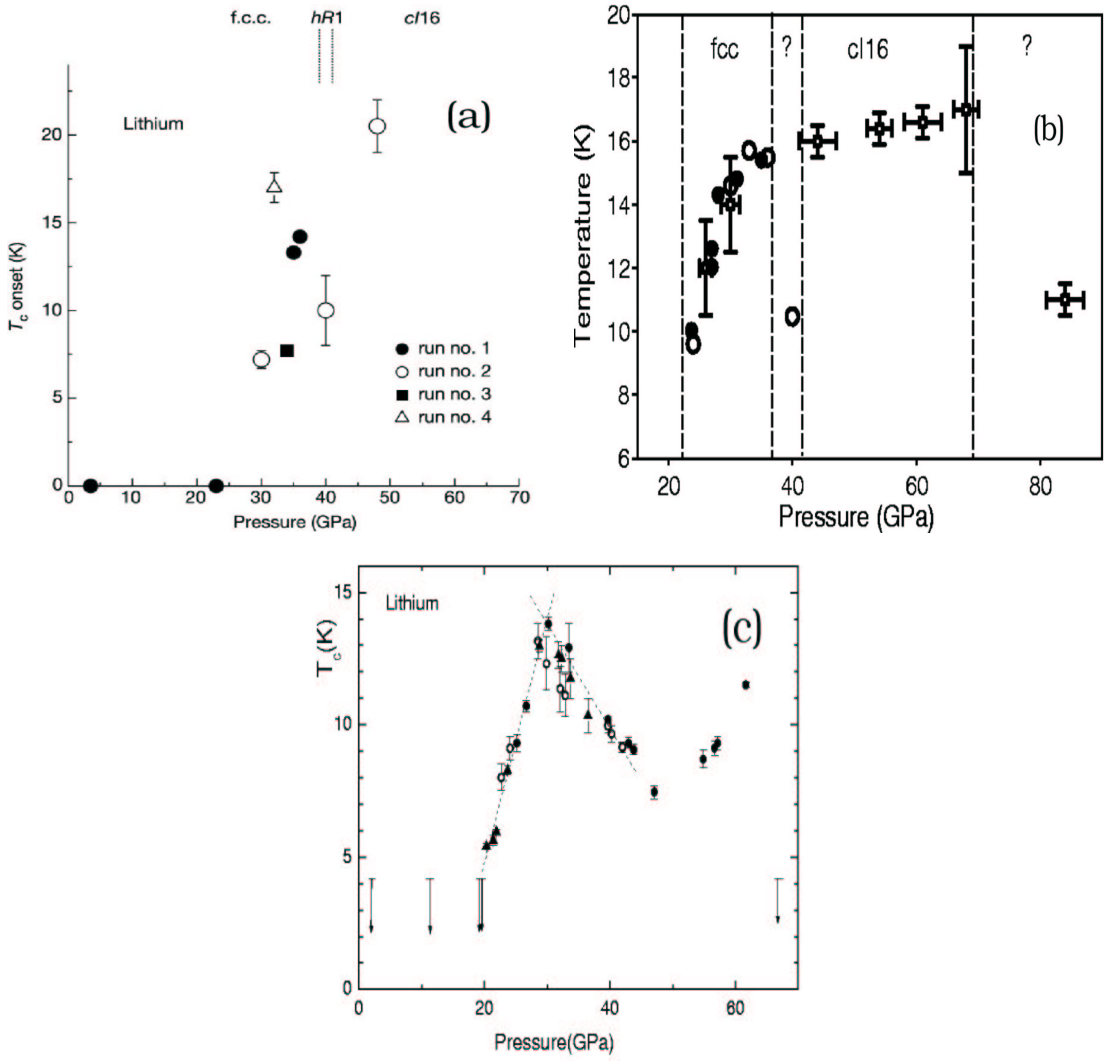

Figure 6.1. Superconducting critical temperature T_c versus Pressure from the three groups mentioned in the text. (a): Shimizu and coworkers [80] (b): Struzhkin and coworkers [81] (c): Deemyad and coworkers [79]

This provided almost as startling a development as the discovery[82] in 2001 of $T_c = 40$ K in MgB_2. Lithium at ambient conditions, after all, is a simple s-electron metal showing no superconductivity above 100 μK.[83] What can possibly transform it into the best elemental superconductor known, still in a simple, monatomic, cubic phase? There is no reason to suspect a magnetic (or other unconventional) pairing mechanism, but it seems equally unlikely that it transforms into a very strongly coupled electron-phonon

(EP) superconductor at readily accessible pressures.

The strength of EP coupling in Li has attracted attention for some time. Evaluations based on empirical pseudopotentials[84] early on suggested substantial coupling strength λ=0.56 and hence readily observable superconductivity ($T_c > 1$ K); more recent calculations relying on the rigid muffin-tin approximation (RMTA) reached a similar conclusion[85, 86] and led to prediction of remarkably high $T_c \sim 70$ K under pressure.[86] None of these studies actually calculated phonon frequencies, relying instead on estimates of a representative phonon frequency $\bar{\omega}$ based on the Debye temperature, which is only an extrapolation from the $q \to 0$ phonons. Linear response calculations of the phonons and EP coupling[87] in bcc Li confirmed that superconductivity would occur in bcc Li ($\lambda = 0.45$), but superconductivity is not observed due to the transformation into the 9R phase with 25% weaker coupling. Experimentally, superconductivity only appears above 20 GPa in the fcc phase.

In the work presented here, we focus on the monatomic fcc phase that is stable in the 20-38 GPa range. After providing additional characterization of the previously discussed[88, 89, 90, 91] evolution of the electronic structure under pressure, we analyze the implications of the Fermi surface (FS) topology for properties of Li. To study λ microscopically we focus on the decomposition[95] into mode coupling strengths $\lambda_{Q\nu}$, where $\lambda = (1/3N)\sum_{Q\nu}\lambda_{Q\nu} = <\lambda_{Q\nu}>$ is the Brillouin zone (BZ) and phonon branch (ν) average. We find that increase of pressure leads to *very strong* EP coupling to a *specific branch* in *very restricted regions* of momentum space determined by the FS topology; these features are directly analogous to the focusing of coupling strength[92, 93, 94] in MgB_2. Unlike in MgB_2, tuning with pressure leads to a vanishing harmonic frequency at ~25 GPa, beyond which the fcc phase is stabilized by anharmonic interactions.

6.2 Electronic Structure

First, let us look at the evolution of the band structure with pressure. Fig. 6.2 shows the s and p - orbital projected band structure at 0 and 35 GPa. Necks start to appear along the $\Gamma \rightarrow L, \langle 111 \rangle$ direction. The volume at 35 GPa is 51% of that at P=0, so the conduction electron density has doubled. We observe an increase in the p character of the band crossing the Fermi level as we go from 0 to 35 GPa. This shift in character from s to p is analogous to the $s \rightarrow d$ crossover in the heavier alkali metals.[96] The occupied bandwidth increases by only 14%, much less than the free electron value $2^{2/3}$-1 = 59%; this discrepancy is accounted for by the 55% increase in the k=0 band mass (m_b/m=1.34 at P=0 to m_b/m=2.08 at 35 GPa).

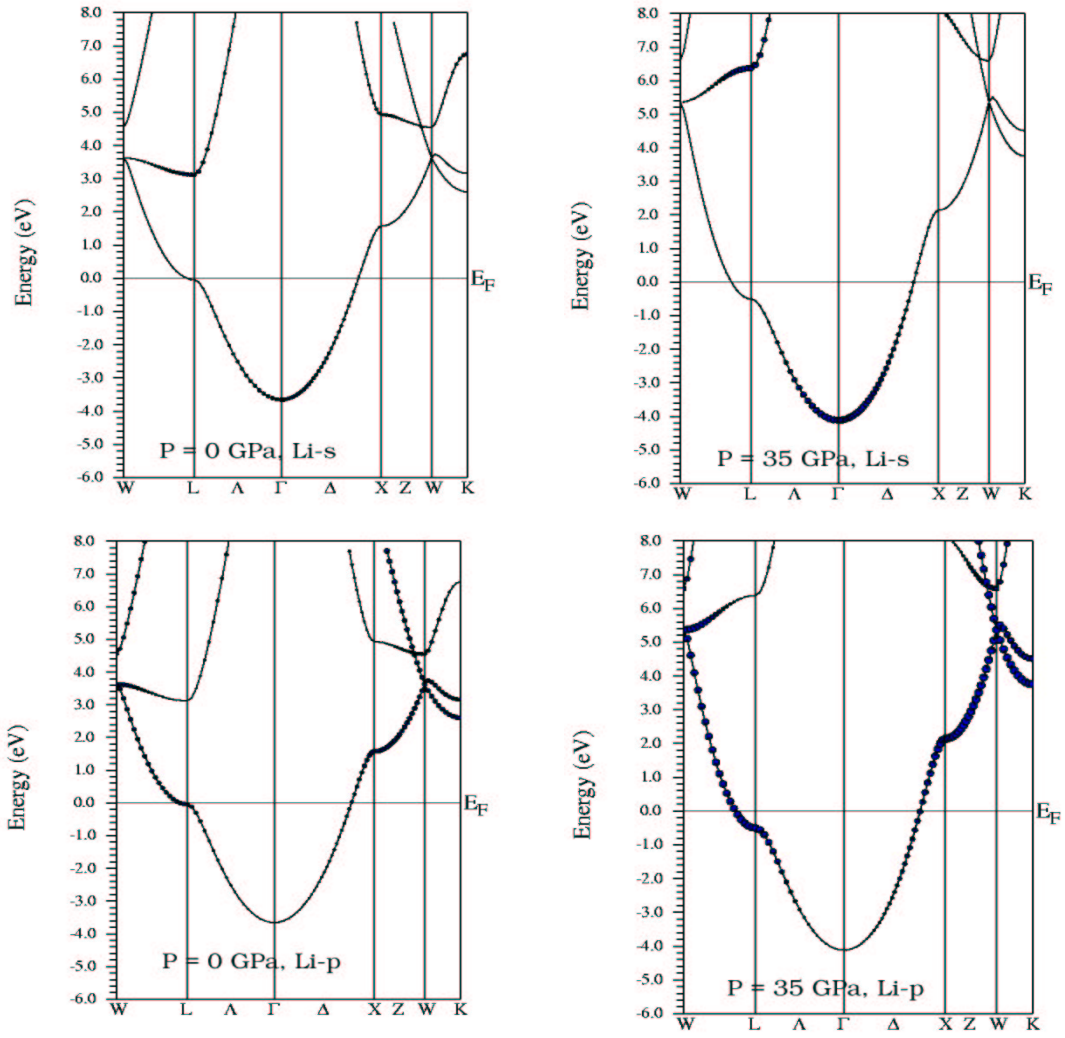

Figure 6.2. Lithium, s and p orbital projected band structure at 0 and 35 GPa. The size of the filled circles indicate the relative contribution of the orbital to the underlying bands. As noted in the text, we observe an increase in p character as a function of pressure, with necks appearing along $\langle 111 \rangle$ direction.

At P=0 in the fcc phase the FSs are significantly nonspherical and just touch at the L points of the BZ; necks (as in Cu), where the p character is strongest, grow with increasing pressure, and the FS at 35 GPa is shown in Fig. 6.3, colored by the Fermi velocity. The topology of the FS plays a crucial role in the superconductivity of Li, as we discuss below.

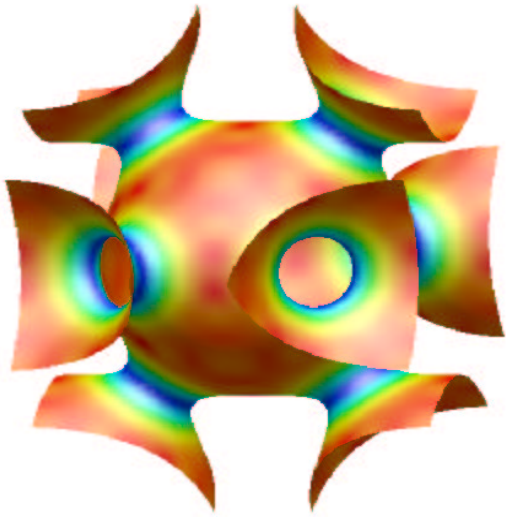

Figure 6.3. Fermi surface of Li at 35 GPa plotted in a cube region around k=0 and colored by the value of the Fermi velocity. Red (belly areas) denotes fast electrons (v_F^{max} = 9×10^7 cm/s), blue (on necks) denotes the slower electrons (v_F^{min} = 4×10^7 cm/s) that are concentrated around the FS necks. The free electron value is 1.7×10^8 cm/s.

6.3 Analytic Properties of the Nesting Function

The coupling strength λ is the average of mode coupling constants[95]

$$\lambda_{\vec{Q}\nu} = \frac{2N_\nu}{\omega_{\vec{Q}\nu} N(0)} \frac{1}{N} \sum_k |M^{[\nu]}_{k,k+Q}|^2 \delta(\varepsilon_k)\delta(\varepsilon_{k+Q}), \tag{6.1}$$

with magnitude determined by the EP matrix elements $M^{[\nu]}_{k,k+Q}$ and the nesting function $\xi(Q)$ describing the phase space for electron-hole scattering across the FS (E$_F$=0),

$$\xi(Q) = \frac{1}{N} \sum_k \delta(\varepsilon_k)\delta(\varepsilon_{k+Q}) \propto \oint \frac{dL_k}{|\vec{v}_k \times \vec{v}_{k+Q}|}. \tag{6.2}$$

Here the integral is over the line of intersection of the FS and its image displaced by Q, $\vec{v}_k \equiv \nabla_k \varepsilon_k$ is the velocity, and N(0) is the FS density of states. Evidently $\xi(Q)$ gets large if one of the velocities gets small, or if the two velocities become collinear.

Note that $\frac{1}{N}\sum_Q \xi(Q) = [\mathrm{N}(0)]^2$; the topology of the FS simply determines how the fixed number of scattering processes is distributed in Q. For a spherical FS $\xi(Q) \propto$

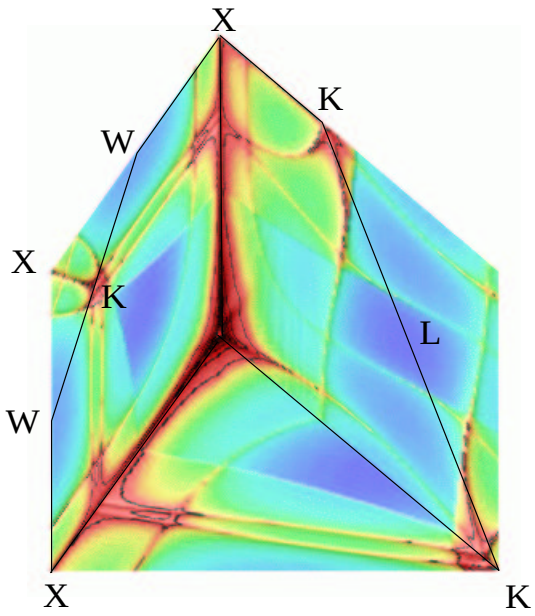

Figure 6.4. Surface plots of the nesting function $\xi(Q)$ at 35 GPa throughout three symmetry planes: (010) Γ-X-W-K-W-X-Γ; (001) Γ-K-X-Γ; (110) Γ-K-L-K-X-Γ. The Γ point lies in the back corner. The dark (red) regions denote high intensity, the light (blue) regions denote low intensity. The maxima in these planes occur near K and along Γ-X. To obtain the fine structure a cubic k mesh of $(2\pi/a)/160$ was used (2×10^6 points in the BZ).

$\frac{1}{|Q|}\theta(2k_F - Q)$; in a lattice it is simply a reciprocal lattice sum of such functions. This simple behavior (which would hold for bcc Li at P=0, for example) is altered dramatically in fcc Li, as shown in Fig. 6.4 for P=35 GPa (the nonphysical and meaningless $\frac{1}{|Q|}$ divergence around Γ should be ignored). There is very fine structure in $\xi(Q)$ that demands a fine k mesh in the BZ integration, evidence that there is strong focusing of scattering processes around the K point, along the Γ-X line peaking at $\frac{3}{4}$ Γ-X≡X_K, and also a pair of ridges (actually, cuts through surfaces) running in each (001) plane in K-X_K-K-X_K-K-X_K-K squares. Some additional structures are the simple discontinuities mentioned above, arising from the spherical regions of the FS.

Structure in $\xi(Q)$ arises where the integrand in Eq. 6.2 becomes singular, i.e.

when the velocities at k and $k+Q$ become collinear. The FS locally is either parabolic or hyperbolic, and the nature of the singularity is governed by the difference surface which also is either parabolic or hyperbolic. In the parabolic case (such as two spheres touching) $\xi(Q)$ has a discontinuity. In the hyperbolic case, however, $\xi(Q)$ *diverges* logarithmically. Such divergent points are not isolated, but locally define a surface of such singularities (or discontinuities, in the parabolic case). The ridges and steps visible in Fig. 6.4 are cuts through these singular surfaces; the intensity at K arises from transitions from one neck to (near) another neck and is enhanced by the low neck velocity (In Fig 6.5, two such scenario wherein the intensity arises from neck to neck transitions are shown). Roth *et al.* have pointed out related effects on the susceptibility[97] (which will analogously impact the real part of the phonon self-energy), and Rice and Halperin[98] have discussed related processes for the tungsten FS. In the susceptibility (and hence in the phonon renormalization) only FS nesting with antiparallel velocities gives rise to Q-dependent structure. This explains why the ridge in $\xi(Q)$ along the Γ-X line (due to transitions between necks and the region between necks) does not cause much softening (Fig. 6.6 portrays such a scenario); there will however be large values of $\lambda_{Q\nu}$ because its structure depends only on collinearity.

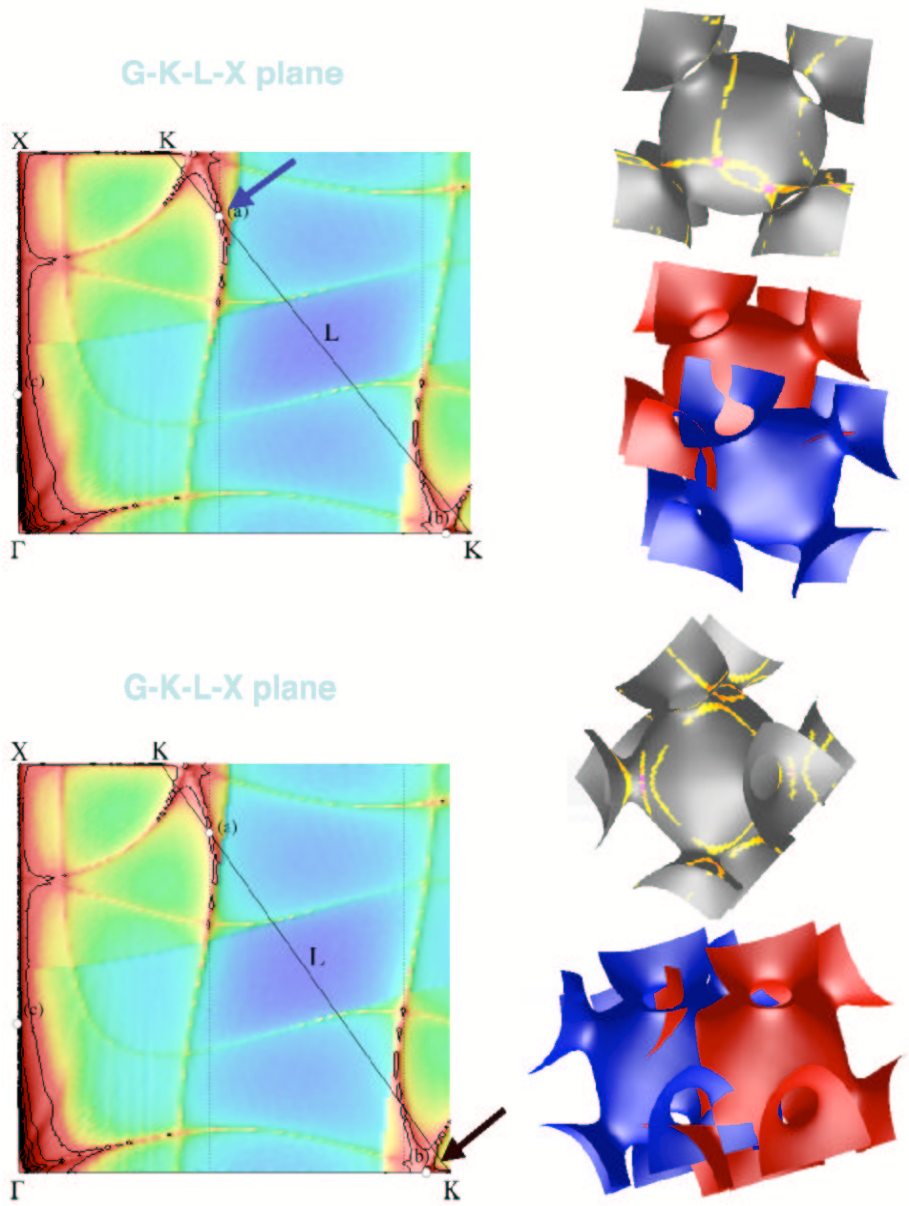

Figure 6.5. Two dimensional view of the nesting function $\xi(Q)$ along with the Fermi surfaces with relative shift, indicating lines of intersection. The light areas indicate the 'hot spots' (the intersection of the Kohn anomaly surfaces with the Fermi surface) that are involved in strong nesting and strong coupling. *Top and Bottom panel*: Nesting intensity near K, arising from one neck to another neck transition.

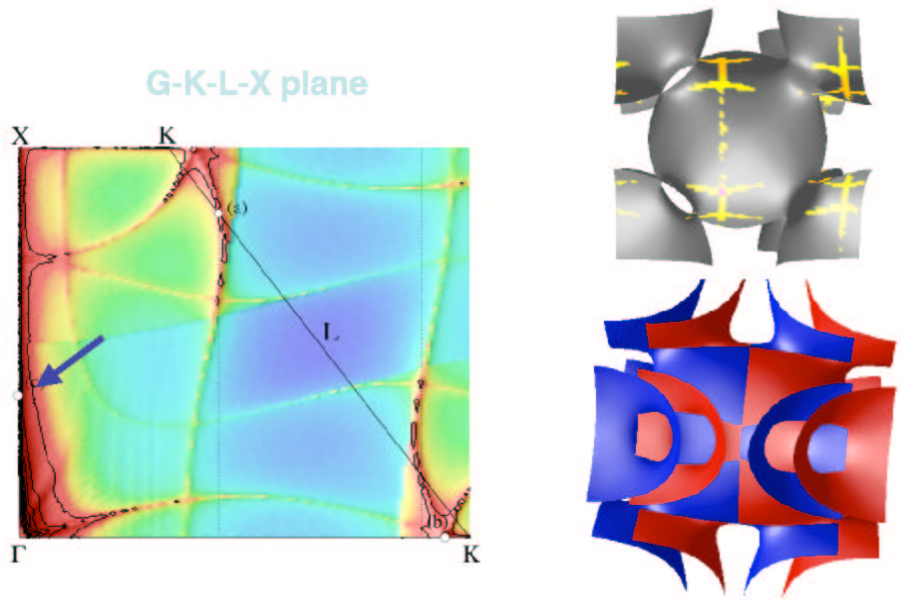

Figure 6.6. Same as Fig. 6.5, but shown here is the unphysical nesting arising along the $\Gamma \rightarrow X$ line from the transition between necks and regions between the necks.

Divergences of $\xi(Q)$, which we relate to specific regions of the FS shown in Fig. 6.4 (mostly distinct from the flattened regions between necks discussed elsewhere[91]), specify the Q regions of greatest instability. However, instabilities in harmonic approximation ($\omega_{Q\nu} \rightarrow 0$) may not correspond to physical instabilities: as the frequency softens, atomic displacements increase and the lattice can be stabilized to even stronger coupling (higher pressure) by anharmonic interactions.

6.4 Electron-Phonon interaction and evaluation of T_c

The phonon energies and EP matrix elements have been obtained from linear response theory as implemented in Savrasov's full-potential linear muffin-tin orbital code [74, 75]. We have used the Vosko-Wilk-Nusair local exchange-correlation [104]. To illustrate the evolution with pressure, we use the fcc lattice constants 8.00, 7.23, 6.80, 6.6, and 6.41 bohr, corresponding approximately to 3, 10, 20, 30, and 35 GPa respectively, accord-

ing to the experimental equation of state [102]. (and we use these pressures as labels). The 8.00 bohr value is the local density approximation equilibrium lattice constant. The 3 and 35 GPa phonon energies are calculated at 72 inequivalent Q points (a $12 \times 12 \times 12$ grid), with a $24 \times 24 \times 24$ grid for the zone integration when calculating the Eliashberg spectral function. The 10 GPa phonons are calculated at 29 inequvalent Q points (a $12 \times 12 \times 12$ grid), with a $24 \times 24 \times 24$ grid for the zone integration. The 20 and 30 GPa phonons are calculated using a fine mesh with 413 inequivalent Q points (a $24 \times 24 \times 24$ grid), with a $40 \times 40 \times 40$ grid for the zone integration. Though all the calculations were not done for the same sampling, the results presented here show the general trend in understanding the physics as a function of pressure, $i.e.$ what coupling is important for T_c, as opposed to what is important in increasing λ, which is a far simpler question.

6.4.1 Dispersion throughout the zone

The calculated phonon dispersion curves for the various pressures are displayed in Fig. 6.7. As a function of pressure, we notice softening midway along the Γ - L direction (transverse $\mathcal{T}$ branches), for the $\langle 1\bar{1}0 \rangle$ polarized $\mathcal{T}_1$ branch along the Γ - K direction which becomes unstable around 32 GPa, and possibly softening in the $\mathcal{T}$ branches around the X point. The noticeable dip near the midpoint of Γ - L is reflected in the ridge in $\xi(Q)$ running downward from the uppermost K point in Fig. 6.4. The $\mathcal{T}_1$ branch softens dramatically around the K point and at 35 GPa this mode is unstable in a substantial volume around the K point. This is also reflected in the $\xi(Q)$ in Fig. 6.4. Although, we obtain a 'harmonic' instability at $Q \approx K$ already at around 32 GPa, it is entirely feasible that this system is anharmonically stabilized beyond this pressure (experimentally, the fcc phase prevails to upto 40 GPa), an example of anharmonically stabilized 'high-T_c' superconductivity.

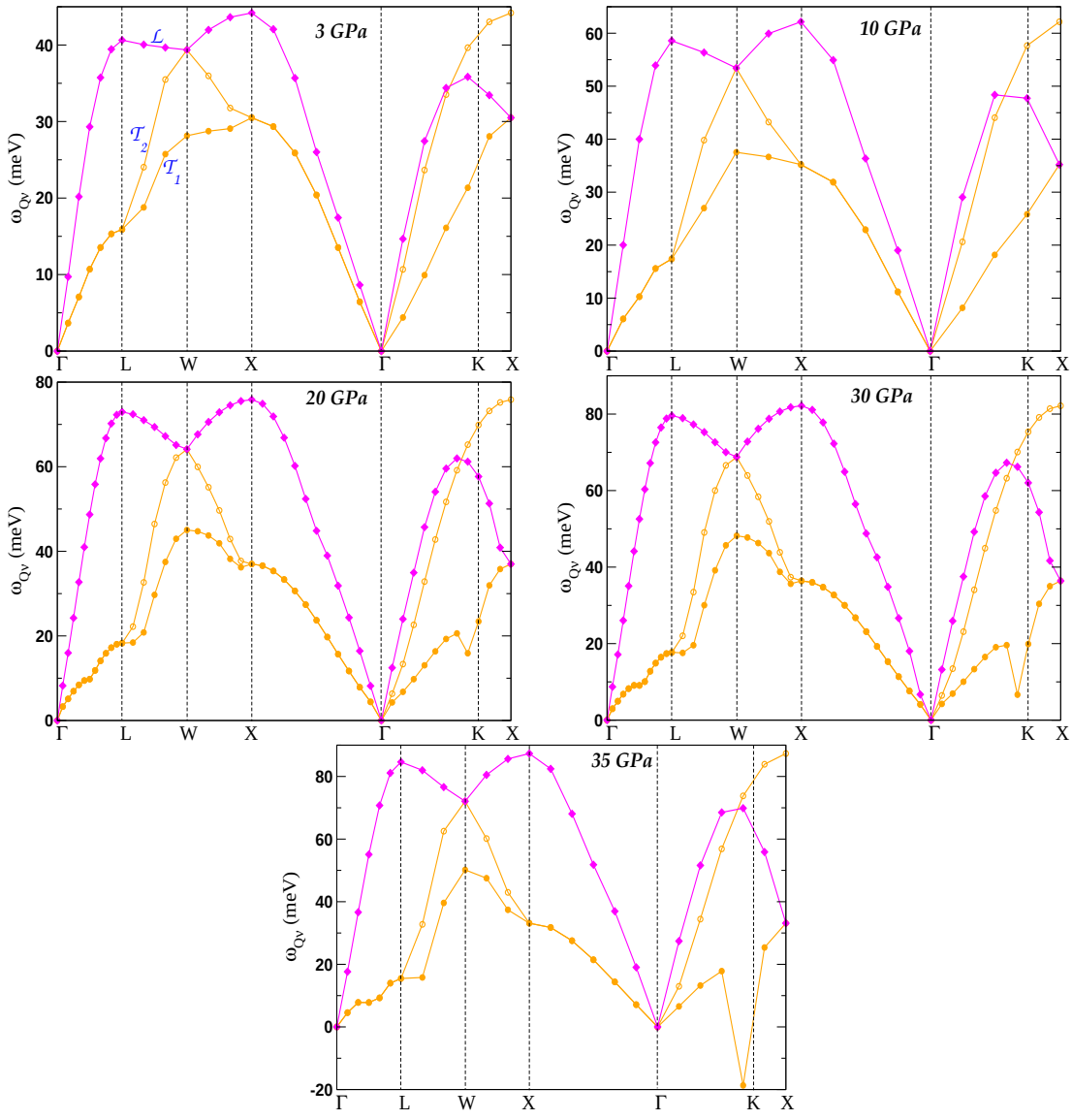

Figure 6.7. Calculated phonon spectrum for fcc Li along high symmetry directions for the various pressures as noted in the text. The solid diamonds denote the longitudinal mode $\mathcal{L}$, and where the transverse branches are non-degenerate, solid circles denote the transverse mode $\mathcal{T}_1$ and open circles denote the transverse mode $\mathcal{T}_2$. The mode symmetry has been used to connect braches across crossings ($\Gamma \rightarrow K$) although this is not possible off symmetry lines where branches do not cross. As a function of pressure, we notice softening midway along the Γ - L direction (transverse $\mathcal{T}$ branches), for the $\langle 1\bar{1}0 \rangle$ polarized $\mathcal{T}_1$ branch along the Γ - K direction, which becomes unstable around 32 GPa and possibly softening in the $\mathcal{T}$ branches around the X point.

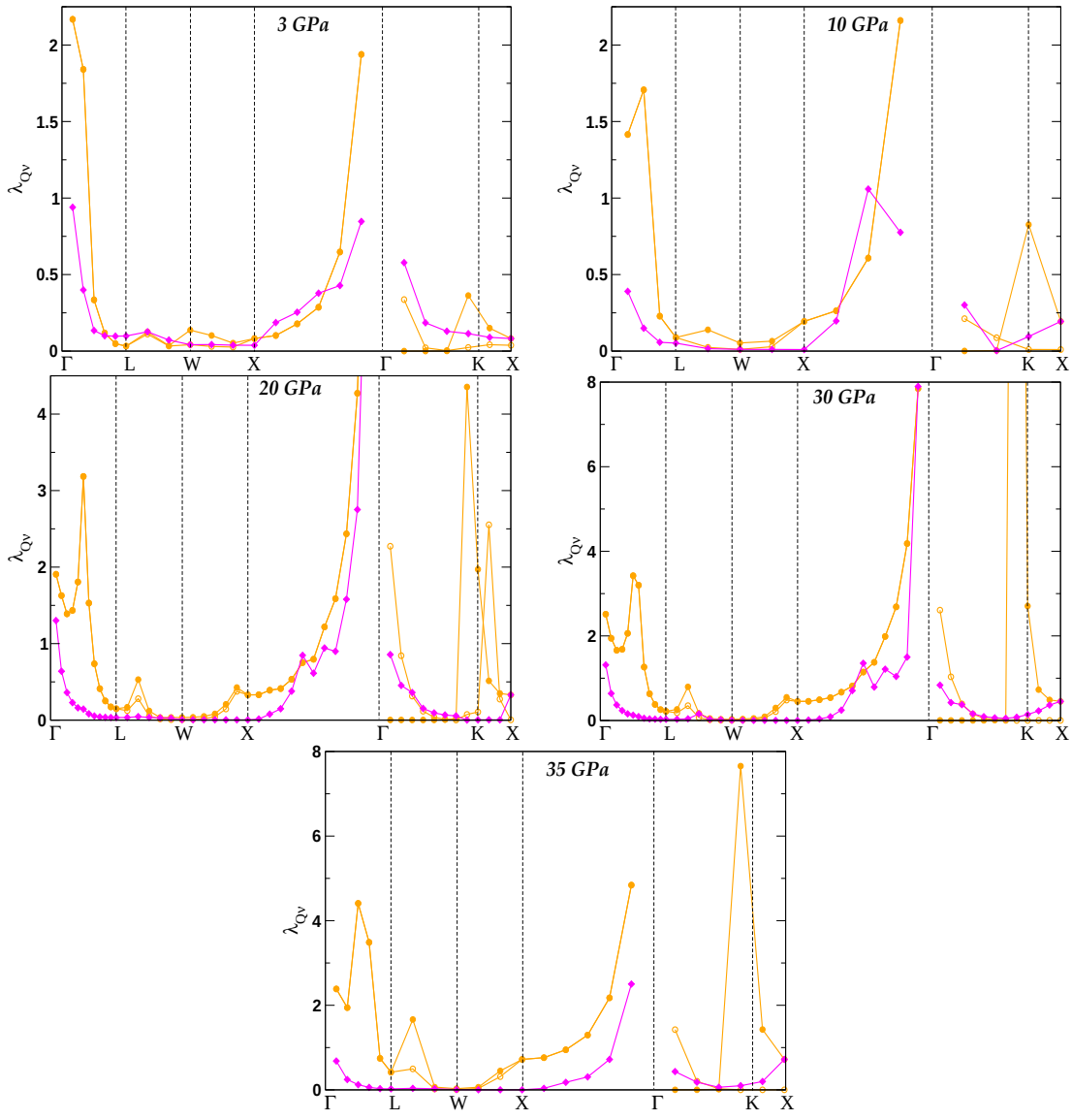

Figure 6.8. Calculated mode $\lambda_{Q\nu}$ values for the various pressures, following the notation in Fig. 6.7. The landscape is dominated by peaks in the transverse branches near K, a longitudinal peak along Γ - L, and an increase around $Q \approx$ zero where the phase space is limited. Here $\lambda_{Q\nu}$ is normalized such that the total λ requires a sum over the three branches (rather than an average).

The corresponding 'mode λ' values $\lambda_{Q,\nu}$ are presented in Fig. 6.8. With increase in pressure from 3 to 35 GPa, the electron-phonon coupling constant increases. The $\lambda_{Q,\nu}$ values for the $\mathcal{T}_1$ branch near K, and also near the midpoint of the Γ - L line are larger

compared to the other areas in the BZ, as expected from the phonon kinks. In addition, we notice that the $\lambda_{Q,\nu}$ values for all the three branches are large along the Γ - X; this coupling is not immediately obvious from the phonon dispersion in Fig. 6.7 because it depends only weakly on Q.

The calculation of $\xi(Q)$ and the phonon spectrum has shown that the Fermi surface topology concentrates scattering processes into well-defined surfaces in Q space and even in alkali metals, can lead to very strong coupling to specific phonons that can finally drive lattice instability. To enhance λ, it is necessary in addition that the large regions of $\xi(Q)$ are accompanied by large electron-phonon matrix elements. In order to verify that, we took the $Q = (\frac{2}{3}, \frac{2}{3}, 0)\frac{2\pi}{a}$ phonon (near K) and did frozenphonon calculations as a function of pressure for both $\mathcal{T}_1$ and $\mathcal{T}_2$ transverse modes. $\mathcal{T}_1$ mode is polarized along the $\langle 001 \rangle$ axis, while the $\mathcal{T}_2$ mode is polarized along the $\langle 1\bar{1}0 \rangle$ axis. From our total energy calculations, we find that the $\mathcal{T}_1$ (unstable) phonon causes large band shifts with atomic displacement ($\delta\varepsilon_K/\delta u \approx 5eV/\mathring{A}$) near the Fermi surface necks, while for the stable $\mathcal{T}_2$ mode band shifts are no more than 5% of this value (Fig. 6.9, 6.10). Thus, the focusing of the scattering processes is indeed coupled with large, polarization-dependent matrix elements.

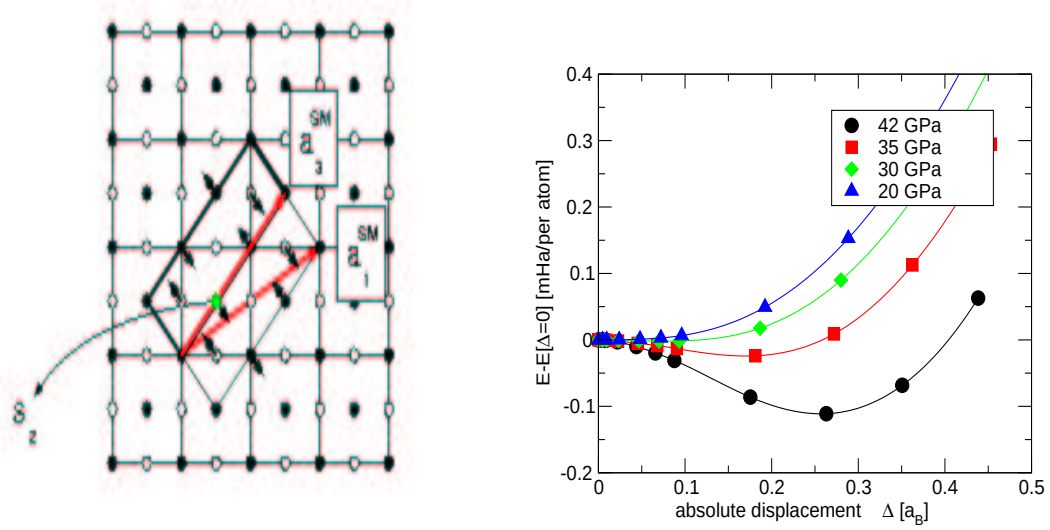

Figure 6.9. Frozen phonon results for the $\langle 1\bar{1}0\rangle$ polarized $\mathcal{T}_1$ branch. *Left panel*: Super cell, which contains two wave length of the $Q = (\frac{2}{3}, \frac{2}{3}, 0)\frac{2\pi}{a}$ phonon polarized in the $\langle 1\bar{1}0\rangle$ direction. *Right panel*: Total energy curves as a function of absolute displacement. As the pressure increases the minimum in the total energy happens when the atoms are displaced away from their fcc equilibrium positions. A plot of the band structure reveals large band shifts of 5 eV/$\mathring{A}$.

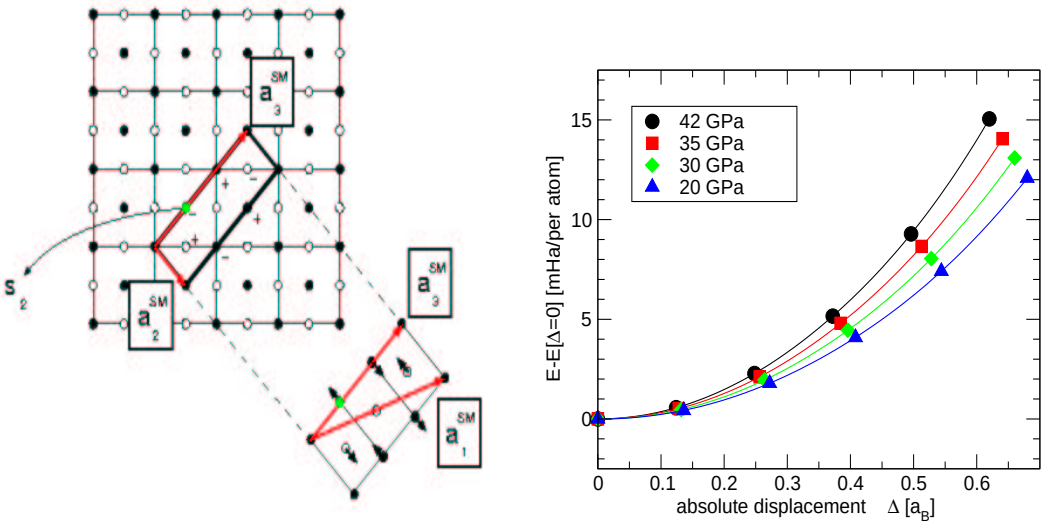

Figure 6.10. Frozen phonon results for the $\langle 001 \rangle$ polarized $\mathcal{T}_2$ branch. *Left panel*: Super cell, which contains two wave length of the $Q = (\frac{2}{3}, \frac{2}{3}, 0)\frac{2\pi}{a}$ phonon polarized in the $\langle 001 \rangle$ direction. *Right panel*: Total energy curves as a function of absolute displacement. As the pressure increases the minimum in the total energy always occurs when the atoms are in the fcc equilibrium positions. A plot of the band structure reveals no band shifts in particular.

In Fig. 6.11, we display the corresponding linewidths $\gamma_{Q\nu}$, which are given by[95]

$$\gamma_{Q\nu} = 2\pi\omega_{Q\nu} \sum_k |M^{[\nu]}_{k,k+Q}|^2 \delta(\varepsilon_k)\delta(\varepsilon_{k+Q}). \tag{6.3}$$

While $\gamma_{Q\nu}$ includes the same Q-specific Fermi surface average of the EP matrix elements with respect to the available phase space for scattering through wavevector Q as does $\lambda_{Q\nu}$, it is proportional to $\omega_{Q\nu}$ rather than inversely proportional. As a result, $\gamma_{Q\nu}$ is a much better indicator of the importance of the coupling for T_c. Coupling at high frequency is much more important than at low frequency for T_c, whereas the opposite is true for λ. Thus it is not surprising that the linewidth 'dispersion' in Fig. 6.11 provides a different viewpoint than does the $\lambda_{Q\nu}$ dispersion. There is still the large contribution from the region around K where there is an incipient instability, but it is very limited in Q and

very sharply structured, not being resolved even by the Q mesh we have used. The really impressive region however is the $\mathcal{L}$ branch along (100) directions, which dominates the landscape (at least along symmetry lines). There are also important contributions from the $\mathcal{L}$ branch along the Γ-K lines and from the $\mathcal{T}$ branches along (100). Even the small peak in the $\mathcal{T}$ branches midway between Γ and L (where the kink in the $\mathcal{T}$ branch occurs) is small compared to the contribution from the $\mathcal{L}$ branch along the same line. Tse *et al.* present γ_Q at $V/V_0 = 0.45$ GPa (≈ 50 GPa) which have some features [105] in common with Fig. 6.11, but cannot be compared in detail because of the different volumes.

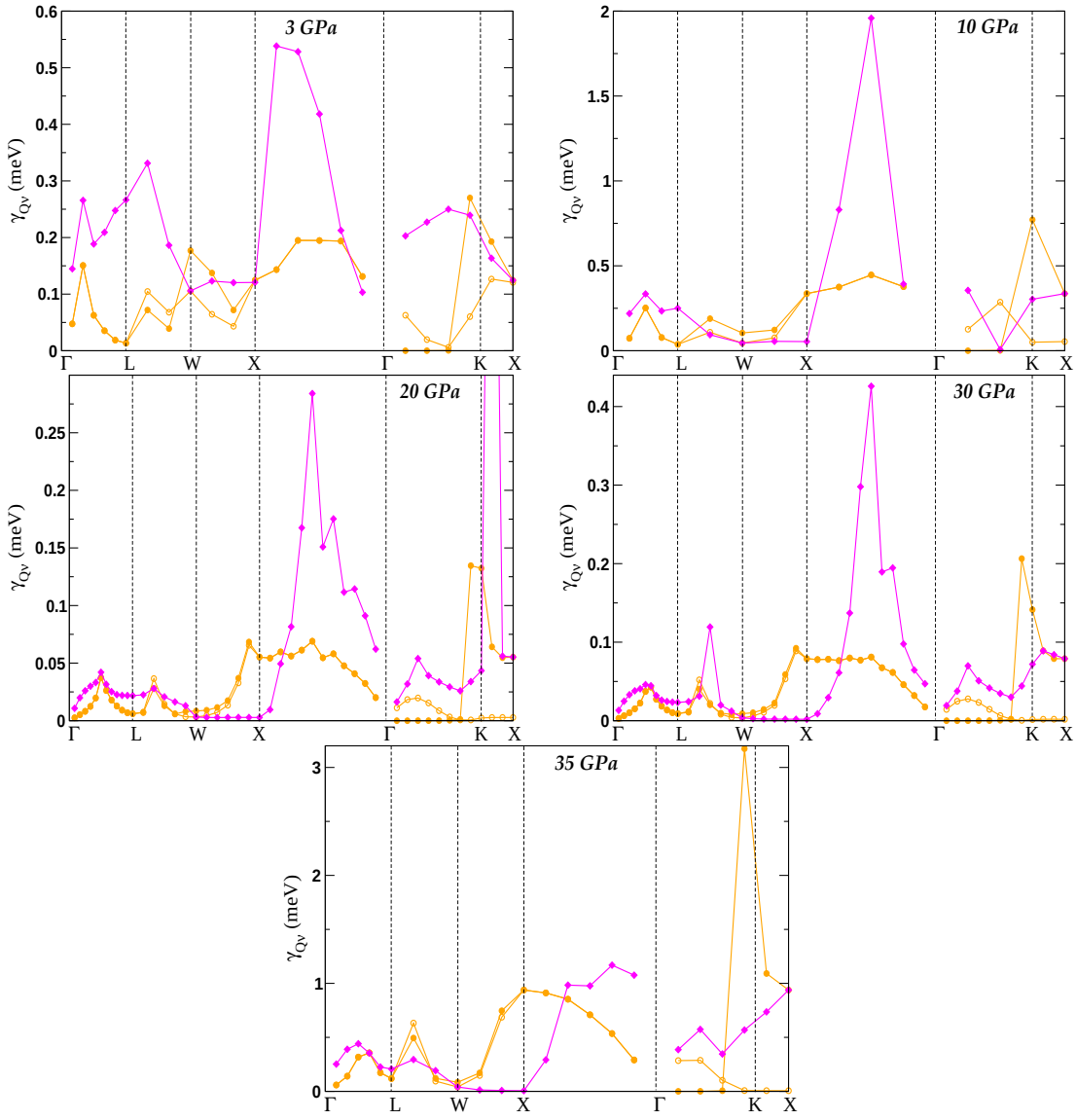

Figure 6.11. Calculated linewidths $\gamma_{Q\nu}$, following the notation of Fig. 6.7. The landscape here is dominated by all modes along Γ - X, and the region near K.

6.4.2 Spectral functions and T_c

The phonon frequency distribution $F(\omega)$ is shown in Fig. 6.12. The contribution to the phonon density of states comes from both the low and high frequency phonons as we increase the pressure from 3 to 35 GPa, indicative of the fact that the higher energy longitudinal phonons also play a role in determining the T_c.

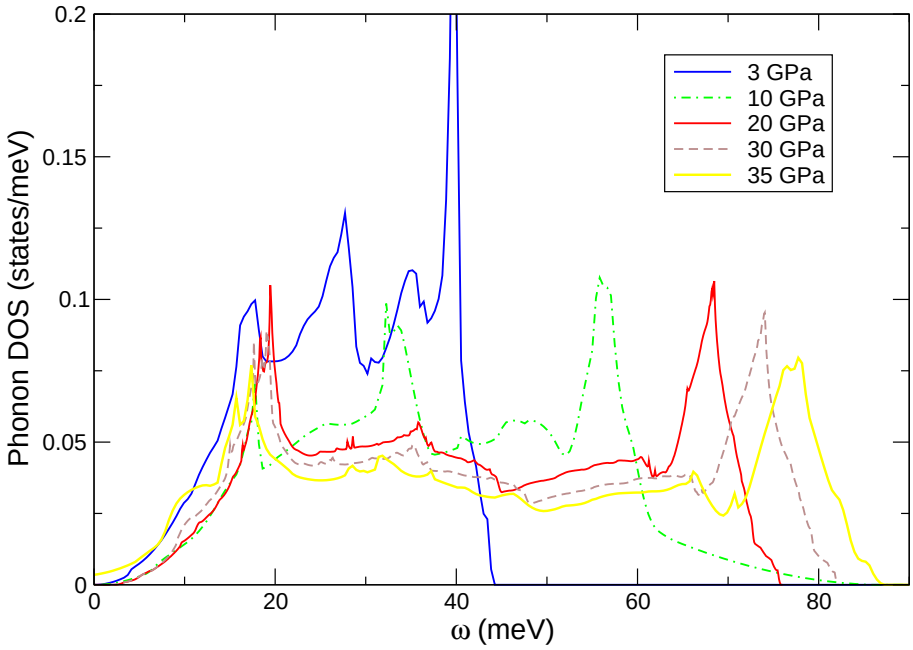

Figure 6.12. Phonon density of states as a function of pressure.

The electron-phonon spectral function $\alpha^2F(\omega)$ was evaluated using the tetrahedron method and is displayed in the inset of Fig. 6.13. Because of the fine structure in $\xi(Q)$ and hence, in $\lambda_{Q\nu}$, numerically precise results cannot be expected, but general trends should be evident. The resulting spectra shows the hardening of the highest frequency $\mathcal{L}$ mode with pressure (43 $\rightarrow$ 83 meV). The most important change is the growth in weight centered at 25 meV (10 GPa) and then decreasing to 15 meV (20 GPa), beyond which the instability renders any interpretation at 35 GPa questionable. The growing strength is at the low energy; note, however, that this region is approaching the energy $\omega_{opt} = 2\pi k_B T_c \approx$ 10 meV, which Bergmann and Rainer [99] found from calculation of $\delta T_c/\delta\alpha^2F(\omega)$ to be the optimal position to concentrate the spectral weight. The frequency resolved coupling strength $\alpha^2(\omega)$ is also shown in Fig. 6.13.

Table 6.1. From the calculated $\alpha^2F(\omega)$ at various pressures, this table provides: the logarithmic, first, and second moments of the frequency; the value of λ; T_c (K) calculated using μ^*=0.13 and μ^*=0.20; and two simple measures of α^2F (see text).

Pressure mesh	ω_{log} (K)	ω_1 (K)	ω_2 (K)	λ	T_c (μ^*=0.13)	T_c (μ^*=0.20)	$\lambda\omega_1$ (K)	$\sqrt{\lambda\omega_2^2}$ (K)
3 GPa	209	247	277	0.4	0.4	0.01	99	175
10 GPa	225	261	300	0.65	5	1.8	169	242
20 GPa	217	255	297	1.0	13	8.7	250	294
30 GPa	183	225	273	1.3	19	14	292	311

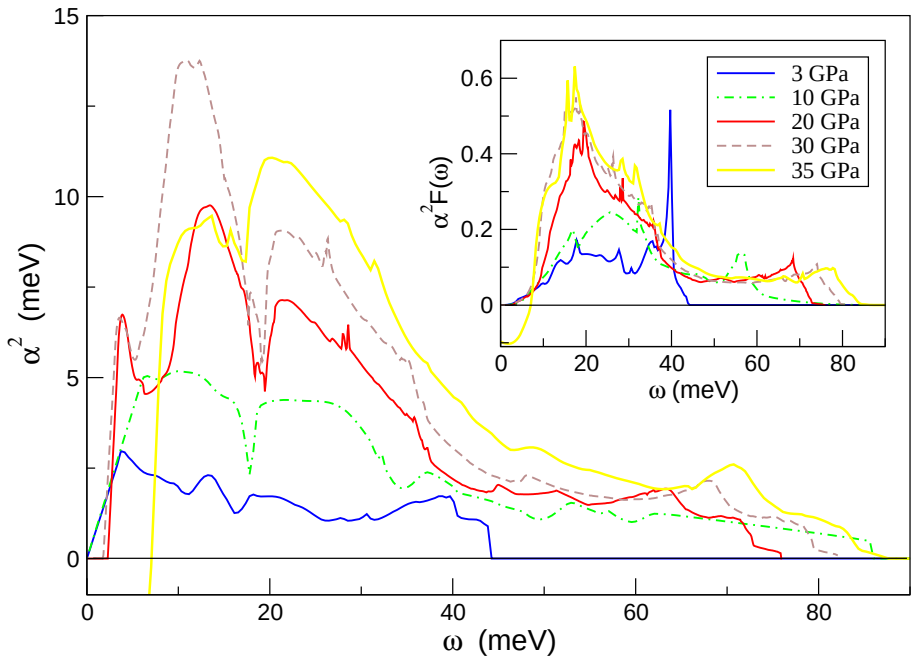

Figure 6.13. Comparison of the Eliashberg spectral function $\alpha^2F(\omega)$ (inset) and the frequency resolved coupling strength $\alpha^2(\omega)$ for fcc Li as a function of pressure.

We now concentrate on the evaluation of T_c and the interpretation of the distribution of coupling. Since the material constants listed in Table 6.1 for the various

pressures have been obtained from different set of sampling of the irreducible BZ, it would not be fair to compare the numbers, but as mentioned previously, the trends should be evident. We have obtained T_c using the Allen-Dynes equation[77]

$$T_c = \frac{\omega_{log}}{1.2}\Lambda_1\Lambda_2 exp\{-\frac{1.04(1+\lambda)}{\lambda-\mu^*(1+0.62\lambda)}\} \tag{6.4}$$

where Λ_1, Λ_2 are strong coupling corrections that depend on λ, μ^*, and the ratio ω_2/ω_{log}, which is a measure of the shape of α^2F. These values should be compared with the nearly hydrostatic value T_c = 6 K at 20 GPa found by Deemyad and Schilling.[79] One main thing to notice is the fact that the T_c values are not directly related to the change in λ as a function of pressure.

6.5 Analysis and Summary

This apparent weak dependence of T_c on λ reflects the observation, made several times in the past,[108] that, for providing an estimate of T_c with averages of α^2F, the combination of λ and some frequency moment separately is not the best choice. This observation is connected with the observation that coupling at low frequency, which strongly enhances λ, has only a weak effect on T_c. Carbotte and collaborators[108] argued that the product $\lambda\omega_1$ (with ω_1 being the first moment as defined by Allen and Dynes[77]) is nearly proportional to T_c for $1.2 \leq \lambda \leq 2.4$; this quantity is proportional to the area under α^2F and corresponds to a zone integral of $\gamma_{Q\nu}/\omega_{Q\nu}$. They were not including strong coupling corrections to T_c,[77] however, which were unknown at the time of the original work. The strong-coupling limit[77] gives $T_c \propto \sqrt{\lambda\omega_2^2}$; this product $\lambda\omega_2^2$ corresponds to a zone integral of $\gamma_{Q\nu}$. Even with the differences in the zone samplings, the Carbotte ratio follows the change in T_c best, of these choices.

The behavior of $\lambda_{Q\nu} \propto \gamma_{Q\nu}/\omega_{Q\nu}^2$ does not faithfully represent the relative importance of modes for T_c except in the weak-coupling limit. In the strong coupling limit

(which we do *not* claim is the case for Li) it is $\gamma_{Q\nu}$ that gives the better picture. For another perspective we display in Fig. 6.14 an isosurface of $\gamma_{Q\nu}$ for the $\mathcal{L}$ modes. As expected from Fig. 6.11, it is dominated by contributions near the center of the (100) line. The isocontours form a blunt jack-like shape although the true symmetry is only four-fold. Our corresponding plots for $\lambda_{Q\nu}$ are almost like those of Profeta *et al.*[103] except that we seem to find somewhat larger contributions near the zone center.

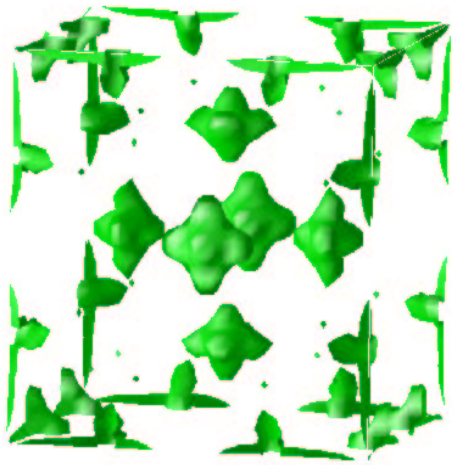

Figure 6.14. Isosurface plot of $\gamma_{Q\nu} = 0.054$ meV for the longitudinal branch at 20 GPa. The box contains the Γ point at the center and at each corner for this fcc structure. The amplitude is high inside the jack-shaped region midway between Γ and X, corresponding to the large linewidths evident in Fig. 6.11. [Unfaithful interpolation at the edges of the box account for the extra structure in those regions; the box edges are also Γ-X-Γ lines.]

This focusing of EP coupling strength makes accurate evaluation of the total coupling strength λ numerically taxing. The richness and strong $\vec{Q}$ dependence of the electron-phonon coupling and the drastic softening at large Q indicates that a denser zone sampling would be necessary to obtain accurate numerical results and also to obtain a correct understanding of the microscopic origin of the pressure-induced increase in T_c.

Compressed Li, thus has several similarities to MgB_2 - very strong coupling to

specific phonon modes, T_c determined by a small fraction of phonons - but the physics is entirely different, since there are no strong covalent bonds and it is low, not high, frequency modes that dominate the coupling. Compressed Li is yet another system that demonstrates that our understanding of superconductivity arising from 'conventional' EP coupling is far from complete.

Bibliography

[1] I. Loa, and K. Syassen, Solid State Connun. **118**, 279 (2001).

[2] H. Hohenberg, and W. Kohn, Phys. Rev. **136**, B864 (1964).

[3] W. Kohn, and L. J. Sham, Phys. Rev. **140**, A1133 (1965).

[4] J. C. Slater, *The Self-Consistent Field for Molecules and Solids* (McGraw-Hill, New York, 1974).

[5] K. Koepernik, and H. Eschrig, Phys. Rev. B **59**, 1743 (1999).

[6] I. Opahle, K. Koepernik, and H. Eschrig, Phys. Rev. B **60**, 14035 (1999).

[7] V. I. Anisimov, J. Zaanen, and O. K. Andersen, Phys. Rev. B **44**, 943 (1991).

[8] V. I. Anisimov, I. V. Solovyev, M. A. Korotin, M. T. Czyzyk, and G. A. Sawatzky, Phys. Rev. B **48**, 16929 (1993).

[9] I. V. Solovyev, P. H. Dederichs, V. I. Anisimov, Phys. Rev. B **50**, 16861 (1994).

[10] W. E. Pickett, S. C. Erwin, and E. C. Ethridge, Phys. Rev. B **58**, 1201 (1998).

[11] A. I. Liechtenstein, V. I. Anisimov, and J. Zaanen, Phys. Rev. B **52**, R5467 (1995).

[12] V. I. Anisimov, F. Aryasetiawan, A. I. Liechtenstein, J. Phys.: Condens. Matter **9**, 767 (1997).

[13] V. I. Anisimov, and O. Gunnarson, Phys. Rev. B **43**, 7570 (1991).

[14] M. T. Czyżyk, G. A. Sawatzky, Phys. Rev. B **49**, 14211 (1994).

[15] H. Akinaga, T. Manago, and M. Shirai, Jpn. J. Appl. Phys. Part 2, **39**, L1118 (2000).

[16] See J. E. Pask, L. H. Yang, C. Y. Fong, W. E. Pickett, and S. Dag, Phys. Rev. B **67**, 224420 (2003) and references therein.

[17] O. Schmidtz-Dumont and N. Kron, Angew. Chem. **67**, 231 (1995).

[18] B. Taylor, B. Joyner, and F. H. Verhoek, J. Am. Chem. Soc. **83**, 1069 (1961).

[19] K. Suzuki, T. Kaneko, H. Yoshida, H. Morita, and F. Fujimori, J. Alloys Compds. **224**, 232 (1995).

[20] K. Suzuki, T. Shinohara, F. Wagatsuma, T. Kaneko, H. Yoshida, Y. Obi, and S. Tomiyoshi, J. Phys. Soc. Japan **72**, 1175 (2003).

[21] K. Suzuki, H. Morita, T. Kaneko, H. Yoshida, and H. Fujimori, J. Alloys Compds. **201**, 11 (1993).

[22] K. Suzuki, Y. Yamaguchi, T. Kaneko, H. Yoshida, Y. Obi, H. Fujimori, and H. Morita, J. Phys. Soc. Japan **70**, 1084 (2001).

[23] M. Matsuoka, K. Ono, and T. Inukai, IEEE Trans. on Magnetics, Vol. MAG-23, 2788 (1987).

[24] H. Shimizu, M. Shirai, and N. Suzuki, J. Phys. Soc. Japan **66**, 3147 (1997).

[25] B. Eck, R. Dronskowski, M. Takahashi, and S. Kikkawa, J. Mater. Chem. **9**, 1527 (1999).

[26] P. Blaha, K. Schwarz, G. K. H. Madsen, D. Kvasnicka, and J. Luitz, J. Phys. Chem. Solids **63**, 2201 (2002).

[27] J. P. Perdew and Y. Wang, Phys. Rev. B **45**, 13244 (1992).

[28] J. P. Perdew, S. Burke, and M. Ernzerhof, Phys. Rev. Lett. **77**, 3865 (1996).

[29] P. Subramanya Herle, M. S. Hedge, N. Y. Vasathacharya, and S. Philip, J. Solid State Chem. **134**, 120 (1997) and references therein.

[30] A. Filippetti, W. E. Pickett, and B. M. Klein, Phys. Rev. B **59**, 7043 (1999).

[31] A. Filippetti and W. E. Pickett, Phys. Rev. B **59**, 8397 (1999).

[32] See the above paper for references to the literature on FeN.

[33] F. Birch, J. Geophys. Res. **83**, 1257 (1978).

[34] F. D. Murnaghan, Proc. Natl. Acad. Sci. U.S.A. **30**, 244 (1944).

[35] K. Schwarz and P. Mohn, J. Phys. F **14**, L129 (1984); G. L. Krasko, Phys. Rev. B **36**, 8565 (1987).

[36] A. Filippetti and W. E. Pickett, Phys. Rev. Lett. **83**, 4184 (1999).

[37] M. Imada, A. Fujimori, and Y. Tokura, Rev. Mod. Phys. **70**, 1039 (1998).

[38] T. Saitoh, A. E. Bouquet, T. Mizokawa, and A. Fujimori, Phys. Rev. B **52**, 7934 (1995).

[39] J. R. Patterson, C. M. Aracne, D. D. Jackson, V. Malba, S. T. Weir, P. A. Baker, and Y. K. Vohra, Phys. Rev. B **69**, 220101 (2004).

[40] C. S. Yoo, B. Maddox, J.-H. P. Klepeis, V. Iota, W. Evans, A. McMahan, M. Hu, P. Chow, M. Somayazulu, D. Häusermann, R. T. Scalettar and W. E. Pickett, Phys. Rev. Lett. **94**, 115502 (2005).

[41] A. Liebsch, Phys. Rev. Lett. **91**, 226401 (2003).

[42] A. Koga, N. Kawakami, T. M. Rice, and M. Sigrist, Phys. Rev. Lett. **92**, 216402 (2004).

[43] S. Massidda, M. Posternak, A. Baldereschi, and R. Resta, Phys. Rev. Lett. **82**, 430 (1999).

[44] The LDA bands of Fig. 4.3 were calculated with the scalar-relativistic version 5.20 of the full-potential local orbital band structure method (FPLO[**?**]). The basis set consisted of single numerical orbitals for the core states (Mn $1s2s2p$ and O $1s$) and two numerical orbitals for the valence-conduction sector including two $4s$ and $3d$ radial functions, and one $4p$ radial function, for Mn, and two $2s$ and $2p$ radial functions, and one $3d$ radial function, for O. The Mn $3s3p$ semicore states were included as valence states with a single numerical radial function per nl-shell.

[45] H. Eschrig, K. Koepernik, and I. Chaplygin, J. Solid State Chem. **176**, 482 (2003)

[46] J. C. Slater, Phys. Rev. **82**, 538 (1951).

[47] N. F. Mott, Proc. Phys. Soc. A **62**, 416 (1949); *Metal-Insulator Transitions* (Taylor and Francis, London, 1990).

[48] L. F. Mattheiss, Phys. Rev. B **5**, 290, 306 (1972).

[49] K. Terakura, T. Oguchi, A. R. Williams, and J. Kübler, Phys. Rev. B **30**, 4734 (1984).

[50] J. E. Pask, D. J. Singh, I. I. Mazin, C. S. Hellberg, and J. Kortus, Phys. Rev. B **64**, 024403 (2001).

[51] M. Posternak, A. Baldereschi, S. Massidda, and N. Marzari, Phys. Rev. B **65**, 184422 (2002).

[52] Z. Szotek, W. M. Temmerman, and H. Winter, Phys. Rev. B **47**, 4029 (1993).

[53] A. Svane and O. Gunnarsson, Phys. Rev. Lett. **65**, 1148 (1990).

[54] T. Kotani, Phys. Rev. Lett. **74**, 2989 (1995).

[55] T. Kotani and H. Akai, Physica B **237**, 332 (1997).

[56] T. Kotani, J. Phys.: Condens. Matt. **10**, 9241 (1998).

[57] J. D. Talman and W. F. Shadwick, Phys. Rev. A **14**, 36 (1976).

[58] M. Takahashi and J. Igarashi, Phys. Rev. B **54**, 13566 (1996).

[59] I. V. Solovyev and K. Terakura, Phys. Rev. B **58**, 15496 (1998).

[60] S. Y. Savrasov and G. Kotliar, Phys. Rev. Lett. **90**, 056401 (2003). The local impurity solver for DMFT was not specified.

[61] T. Bredow and A. R. Gerson, Phys. Rev. B **61**, 5194 (2000).

[62] C. Franchini, V. Bayer, R. Podloucky, J. Paier, and G. Kresse, Phys. Rev. B **72**, 045132 (2005).

[63] J. Zhang, Phys. Chem. Minerals **26**, 644 (1999).

[64] R. E. Cohen, I. I. Mazin, and D. G. Isaak, Science **275**, 654 (1997).

[65] Z. Fang, I. V. Solovyev, H. Sawada, and K. Terakura, Phys. Rev. B **59**, 762 (1999).

[66] L. Gerward, J. Staun Olsen, L. Petit, G. Vaitheeswaran, V. Kanchana, and A. Svane, J. Alloys & Compounds **400**, 56 (2005).

[67] G. D. Mahan, Phys. Rev. A **22**, 1780 (1980).

[68] N. E. Zein, Sov. Phys.: Solod State **26**, 1825 (1984).

[69] Stefano Baroni, Paolo Giannozzi, and Andrea Testa, Phys. Rev. Lett. **58**, 1861 (1987).

[70] R. M. Sternheimer, Phys. Rev. **96**, 951 (1954); Phys. Rev. **107**, 1565 (1957); Phys. Rev. **115**, 1198 (1959).

[71] S. Yu. Savrasov, Solid State Comm. **74**, 69 (1990).

[72] S. Yu. Savrasov, Phys. Rev. Lett. **69**, 2819 (1992).

[73] S. Y. Savrasov, D. Y. Savrasov, and O. K. Andersen, Phys. Rev. Lett. **72**, 372 (1994).

[74] S. Y. Savrasov, Phys. Rev. B **54**, 16470 (1996).

[75] S. Y. Savrasov, and D. Y. Savrasov, Phys. Rev. B **54**, 16487 (1996).

[76] O. K. Andersen, Phys. Rev. B **12**, 3060 (1975).

[77] P. B. Allen, and R. C. Dynes, Phys. Rev. B **12**, 905 (1975).

[78] H. Sakamoto, T. Oda, M. Shirai and N. Suzuki, J. Phys. Soc. Jpn. **65**, 489 (1996); C. F. Richardson and N. W. Ashcroft, Phys. Rev. Lett. **78**, 118 (1997); K.-H. Lee, K. J. Change and M. L. Cohen, Phys. Rev. B **52**, 1425 (1995).

[79] S. Deemyad and J. S. Schilling, Phys. Rev. Lett. **91**, 167001 (2003).

[80] K. Shimizu *et al.*, Nature **419**, 597 (2002).

[81] V. V. Struzhkin *et al.*, Science **298**, 1213 (2002).

[82] J. Nagamatsu *et al.* Nature **410**, 63 (2001).

[83] K. I. Juntunen and J. T. Tuoriniemi, Phys. Rev. Lett. **93**, 157201 (2004).

[84] P. B. Allen and M. L. Cohen, Phys. Rev. **187**, 525 (1969).

[85] T. Jarlborg, Phys. Scr. **37**, 795 (1988).

[86] N. E. Christensen and D. L. Novikov, Phys. Rev. Lett. **86**, 1861 (2001).

[87] A. Y. Liu *et al.*, Phys. Rev. B **59**, 4028 (1999).

[88] J. B. Neaton and N. W. Ashcroft, Nature **400**, 141 (1999).

[89] K. Iyakutti and C. Nirmala Louis, Phys. Rev. B **70**, 132504 (2004).

[90] M. Hanfland, K. Syassen, N. E. Christensen, and D. L. Novikov, Nature **408**, 174 (2000).

[91] A. Rodriguez-Prieto and A. Bergara, Proc. of the Joint 20th AIRAPT-43rd EHPRG 2005 Conference (unpublished); cond-mat/0505619.

[92] J. An and W. E. Pickett, Phys. Rev. Lett. **86**, 4366 (2001).

[93] J. Kortus *et al*, Phys. Rev. Lett. **86**, 4656 (2001).

[94] Y. Kong *et al.*, Phys. Rev. B **64**, 020501 (2001).

[95] P. B. Allen, Phys. Rev. B **6**, 2577 (1972); P. B. Allen and M. L. Cohen, Phys. Rev. Lett. **29**, 1593 (1972).

[96] A. K. McMahan, Phys. Rev. B **29**, 5982 (1984).

[97] L. M. Roth, J. J. Zieger, and T. A. Kaplan, Phys. Rev. **149**, 519 (1965).

[98] T. M. Rice and B. I. Halperin, Phys. Rev. B **1**, 509 (1970).

[99] G. Bergmann and D. Rainer, Z. Physik A **252**, 174 (1972).

[100] S. K. Bose, T. Kato, and O. Jepsen, cond-mat/0507283.

[101] L. Jansen, Physica A **332**, 249 (2004).

[102] M. Hanfland *et al.*, Solid State Commun. **112**, 123 (1999).

[103] G. Profeta *et al.*, Phys. Rev. Lett. **96**, 047000 (2006).

[104] S. H. Vosko, K. Wilk and N. Nusair, Can. J. Phys. **58**, 1200 (1980).

[105] J. S. Tse, Y. Ma, and H. M. Tutuncu, J. Phys.: Condens. Matt. **17**, S911 (2005).

[106] L. Shi and D. A. Papaconstantopoulos, Phys. Rev. B **73**, 184516 (2006).

[107] Z. P. Yin, S. Y. Savrasov, and W. E. Pickett, private communication.

[108] See J. P. Carbotte, Rev. Mod. Phys. **62**, 1027 (1990) and references therein.